The Generation and Control of Ultrasonic Waves in Nonlinear Media

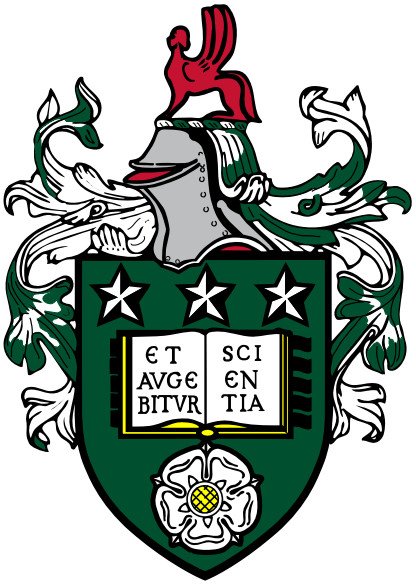

Christopher Adams

School of Electronic and Electrical Engineering

University of Leeds

Submitted in accordance with the requirements for the degree of

Doctor of Philosophy

November 2018

The candidate confirms that the work submitted is their own, except where work which has formed part of jointly authored publications has been included. The contribution of the candidate and the other authors to this work has been explicitly indicated below. The candidate confirms that appropriate credit has been given within the thesis where reference has been made to the work of others.

The work in chapter 2 of the thesis has appeared in publication as follows:

- C. Adams, D. M. Cowell, L. Nie *et al.*, 'A miniature HIFU excitation scheme to eliminate switching-induced grating lobes and nullify hard tissue attenuation', in *Ultrasonics Symposium (IUS), 2017 IEEE International*, IEEE, 2017, pp. 1–4
- D. Cowell, T. Carpenter, P. Smith *et al.*, 'Modified harmonic reduction pulse width modulation (mHRPWM) for switched excitation of resonant HIFU transducers', in *Ultrasonics Symposium (IUS), 2018 IEEE International*, IEEE, 2018, pp. 1–4

I was responsible for the concept, simulation programs, experiments and preparation of the figures and publication. Luzhen Nie and David Cowell were responsible for designing the array excitations. David Cowell was responsible for writing the second manuscript.

The work in chapter 3 of the thesis has appeared in publication as follows:

- C. Adams, S. Harput, D. Cowell *et al.*, 'An adaptive array excitation scheme for the unidirectional enhancement of guided waves', *IEEE transactions on ultrasonics, ferroelectrics, and frequency control*, vol. 64, no. 2, pp. 441–451, 2017
- C. Adams, S. Harput, D. Cowell *et al.*, 'Specimen-agnostic guided wave inspection using recursive feedback', in *IEEE International Ultrasonics Symposium (IUS)*, IEEE, 2016

I was responsible for the entirety of these publications, except the initial concept which David M. Charutz was responsible for.

The work in chapter 4 of the thesis has appeared in publication as follows:

- C. Adams, S. Harput, D. Cowell *et al.*, 'A phase velocity filter for the measurement of Lamb wave dispersion', in *IEEE International Ultrasonics Symposium (IUS)*, IEEE, 2016
- C. Adams, J. McLaughlan, L. Nie *et al.*, 'Excitation and acquisition of cranial guided waves using a concave array transducer', in *Proceedings of Meetings on Acoustics 173EAA*, ASA, vol. 30, 2017, p. 055 003

I was responsible for the entirety of these publications, except the transducer delay profiles which were designed by Luzhen Nie.

The work in chapter 5 of the thesis has appeared in publication as follows:

- C. Adams, T. M. Carpenter, D. Cowell *et al.*, 'HIFU drive system miniaturisation using harmonic reduced pulse width modulation', *IEEE transactions on ultrasonics, ferroelectrics, and frequency control*, 2018
- T. M. Carpenter, C. Adams, S. Freear *et al.*, *Five Level Switched High Intensity Focused Ultrasound Driver Design*, Jul. 2018

I was responsible for the concept, simulation, experiments and composition of the publications. Thomas Carpenter was responsible for the full design and manufacture of the HIFUARP hardware. David Cowell was responsible for designing the HRPWM excitations.

In loving memory of Grandad Ray (1937-2015). Any scholar would be content with half your wisdom.

Acknowledgements

This thesis, like others, owes its existence to many people.

Firstly, I must thank my supervisors: Prof. Steven Freear, Dr. James McLaughlan, and Dr. David Cowell.

To Prof. Freear: I am grateful for your wisdom, a wisdom that at times I questioned, but always proved fruitful and in my best interests. I'm thankful that you undertook all the background work necessary to support my research.

Dr. McLaughlan: I thank you for voluntarily supervising me in the last year of my PhD, and more significantly, for planting the initial seeds in my growing interest in HIFU. Your daily guidance on all aspects of my PhD study and research has been invaluable. Without your mentorship, chapters 2, 4 and 5 would not have been possible.

To Dr. Cowell and particularly Mr Carpenter: I am extremely grateful for the UARP II and the HIFUARP that you designed and built. The development of an ultrasound array platform is no trivial task, and these two excellent machines exist only because of many years of fastidious development. Without either, there would have been no experimental capacity for the work presented here.

I am grateful for Dr. Sevan Harput's candor and supervision during my first year. Your guidance provided me with the skills required to publish my first paper and produce chapter 3 of this thesis.

I must thank the tax-payer and all the funding bodies who have supported me financially: EPSRC, the Royal Society, the Wellcome Institute, the NHLBI, and the University of Leeds.

For Chapter 4, I owe thanks to Alex Starling for cleaning advice and Katherine Fodor of Max-Planck-Institut für Meteorologie for her help with the mathematics. The largest contribution however was from Joahnnes Schneider and Professor Kay Raum of Berlin-Brandenburger Centrum für Regenerative Therapien. Without their generous gift of clinical data, this chapter would not have been possible.

To Ms Anna de Jong, Ms Louisse Coffey, Ms Jenny Blackburn and all the other staff members at the University of Leeds, who are too numerous to name, I am very grateful for your hard work that maintains the institution that has made this thesis feasible.

I must thank all of my office mates; Chunqi (aka Li), Safeer, Abdulrahman, Chau, and Chris. Special thanks however must be given to my friends Oscar, Luzhen and Asraf whom I've spent nearly every working day of the last $3\frac{1}{2}$ years with. They have been excellent confidants, and best of all, they made my PhD study fun. They will all be sorely missed, and I wish them the best of luck with the remainder of their PhD studies.

To my friend Iain, thank you for nudging me to do a PhD in the first place. Likewise, I must thank Mum and Ray for supporting me throughout my study. To all three of them, I'm grateful for the perspective they have provided during the more challenging spans of my PhD study.

Finally, I must thank my partner Michelle for her unwavering patience, understanding, support, and her exhilarating personality.

Abstract

The objective of this thesis is to utilise modern open-design ultrasound research platforms to develop new and advance several existing techniques that incorporate nonlinear phenomena.

Acoustically, nonlinearity refers to changes in speed of sound, attenuation or elasticity that vary with frequency, temperature or pressure. These effects cannot be linearised by the wave equation and require fluid dynamics and elasticity equations to be fully understood. While this is a hindrance and source of error in many areas of ultrasound such as high-intensity focused ultrasound (HIFU) and medical imaging, nonlinearities do have uses in non-destructive guided wave (GW) testing. These effects are influenced greatly by the transducer surface pressure, and so precise control of the excitation is necessary to achieve the desired nonlinear effect, if any, in the medium. In this thesis, aided by the use of two new research platforms, several new ultrasound techniques were developed.

It was shown the frequency content in the electrical waveform is pertinent and so distortion must be minimised. This requirement conflicts with several hardware limitations, however. Accordingly, a genetic algorithm was applied to find novel switched waveform designs. It was found to achieve a 2% granularity in amplitude control with harmonic reduction, where existing waveform designs could not produce any. This fine amplitude control is a requirement for array applications.

Following this, a technique to control the direction of GWs without knowledge of the waveguide was devised. Recordings of a propagating GW, induced by the first element of an array transducer, were re-transmitted in a recursive fashion. The effect was that the transducer's transmissions constructively interfered with the transverse wave, causing most of the guided wave energy to travel in the direction of the transducer's spatial influence. Experimental results show a 34 dB enhancement in one direction compared with the other.

GWs were then applied to bone for two purposes: for assessment of osteoporosis and for measurement of skull properties to assist transcranial therapy. It was shown that existing methods for obtaining dispersion curves are ineffectual due to limitations in the available sampling area. A signal processing scheme was devised to temporally align transverse dispersive waves so that beamforming style techniques could be applied to prove or disprove the existence of certain modes. The technique in combination with multiplication was applied to numerical, ex vivo and in vivo experiments. It was found to improve the contrast of the higher order modes. The technique could improve the reliability of osteoporosis diagnosis with ultrasound, but may also prove useful for acquiring dispersion images in NDT. Numerically the technique was shown to improve the S_3 and A_3 mode intensity by 6 dB and 13 dB respectively compared with an existing Fourier method.

In skull, a relationship was found between the curved therapeutic array geometry and the delay profile necessary to form GWs in skull. Several numerical models were tested and it was shown that the thickness could be obtained from the group velocity. The estimated maximum error using this technique was 0.2 mm. Since the data is co-registered with the therapeutic elements, this method could be used to improve the accuracy

of thermal treatments in the brain.

Finally, the application of switched excitation for HIFU was considered. To improve on cost, efficiency and size, alternative excitation methods have the potential to replace the linear amplifier circuitry currently used in HIFU. In this final study, harmonic reduction pulse width modulation (HRPWM) was proposed as an algorithmic solution to the design of switched waveforms. Its appropriateness for HIFU was assessed by design of a high power 5 level unfiltered amplifier and subsequent thermal-only lesioning of ex vivo chicken breast. HRPWM produced symmetric, thermal-only lesions that were the same size as their linear amplifier equivalents ($p > 0.05$). These results demonstrate that HRPWM can minimise HIFU drive circuity size without the need for filters to remove harmonics or adjustable power supplies to achieve array apodisation.

Overall it has been shown in this thesis that precise control of the nonlinear wave phenomena can be afforded when using open-platform ultrasound research hardware. The methods described within may reduce the cost and increase the efficacy of future commercial systems.

Contents

List of Figures

List of Tables

Abbreviations

AZA	Prototype system for bone quantitative ultrasound
BMD	Bone mass density
CEM43	Cumulative equivalent minutes at 43 °C
CNC	Computer numerically controlled
CT	Computer tomography
CW	Continuous wave
DAC	Digital analogue converter
DAS	Delay and sum
DFT	Discrete Fourier transform
DMAS	Delay multiply and sum
DMUA	Dual mode use array
DSP	Digital signal processing
DXA	Dual X-ray absorptiometry
EMATs	Electromagnetic acoustic transducer
EVA	Prototype system for bone quantitative ultrasound
FEA	Finite element analysis
FEM	Finite element modelling
FFT	Fast Fourier transform
FOV	Field of view
FPGA	Field programmable gate array
GA	Genetic algorithm
GaN	Galium nitride
GAPWM	Genetic algorithm pulse width modulation
GND	Ground
GUIGUW	Graphical User Interface for Guided Ultrasonic Waves
GW	Guided wave
HIFU	High-intensity focused ultrasound
HIFUARP	High-intensity focused ultrasound array research platform
HRPWM	Harmonic reduced pulse width modulation
IC	Integrated circuit

MOSFET	Metal-oxide-semiconductor field-effect transistor
NaOH	Sodium hydroxide
NDE	Non-destructive evaluation
NDT	Non-destructive testing
NMOS,NMOSFET	N-channel MOSFET
NPN	N channel transistor
PCB	Printed circuit board
PCD	Passive cavitation detector
PCI	Peripheral component interconnect
PMOS, PMOSFET	P channel MOSFET
PNP	Peak negative pressure, p channel transistor
PPP	Positive peak pressure
PSAM	Phase shift and multiply
PVDF	Polyvinylidene fluoride
PWM	Pulse width modulation
PZT	Lead zirconate titanate (piezoelectric material)
QUS	Quantitative ultrasound
RAM	Random access memory
RMS	Root mean square
SHM	Structural health monitoring
SNR	Signal to noise ratio
SOS	Speed of sound
SVD	Singular value decomposition
THD	Total harmonic distortion
TX	Transmit
UARP	Ultrasound array research platform
XDR	Transducer

List of Symbols

Symbol	Definition (section)
α_0	Coefficient of sound attenuation at 1 MHz
α	Attenuation coefficient
α_a	Absorption coefficient
α_h	Absorption of harmonic h
α_s	Scatting coefficient
β	Coefficient of nonlinearity
β	Arbitrary integer (4)
β_m	Wavenumber of mode m
γ	Plane wave angle
δ_n	Switching angle n
θ	Incidence angle
θ	Circumferential vector (4.6.2)
λ	Wavelength
Λ	Thermal conductivity
ρ	Density
ρ_0	Initial density
τ	Correlation lag
ϕ	Angle from normal of selected transmit elements
ϕ	Frequency (4.3)
ω	Angular frequency
$a(t)$	Excitation signal
$\mathrm{A}_0, \mathrm{S}_0, \mathrm{A}_1, \mathrm{S}_1, ..\mathrm{S}_m$	Asymmetric and symmetric mode order m (4, 3)
$\overline{A_{1+}}, \overline{A_{2+}}..\overline{A_{N+}}$	Active-low enable signals for positive level N (5)
$A_m(z)$	Mode amplitude
$A_{1-}, A_{2-}..A_{N-}$	Enable signal for negative level N (5)
B/A	Parameter of non linearity

c	Speed of sound
c_0	Initial speed of sound
C_S	Shear speed of sound
C_L	Longitudinal speed of sound
$C_m(z)$	Coupling coefficient of mode m
C_{ph}	Phase velocity
d	Thickness
$D(\phi, m, C_{\text{ph}})$	Delay equation
f	Frequency
f_0	Start frequency (5)
f_0	Fundamental frequency (2)
f_1	Stop frequency (5)
f_2, f_3, f_n	Harmonic 2,3,n (2,5)
f_c	Centre frequency
f_{min}	Minimum filter frequency
f^n	Frequency in n MHz
f_s	Sampling frequency
f_t	Target frequency
F(1,1), F(a,b)	Flexural mode (4)
$F(\omega)$	Frequency response of element
$\mathscr{F}$	Fourier transform
G	Generation number
$g(x)$	Fitness function
h	Harmonic (2)
h	Thickness (3)
H	Heating (2,5)
$H(\omega)$	Transducer response (3)
I	Intensity
k	Wavenumber
l	Number of samples (4.3)
l	Number of levels (2)
L	Pitch

m	Element number (3)
m	Mode number (3)
m	Permutation number (2)
N	DFT size
O	Computational complexity
p	Statistical significance 5.5
p_h	Pressure of harmonic h (5)
P, p	Pressure (2,5)
$P, P_T, P(f)$	Power (5)
P_0	Initial pressure
P_{mm}	Power density (3)
Q	Nyborg's heating
Q	Total transmitting elements (4)
r	Radial vector
R	Number of receiving elements (4)
R_1	Internal radius
R_2	External radius
R_t	Radius of transducer geometry
S	Area

t	Time
t_0	Signal lag
t_{d0}	Element delay
t_k	Propagation delay in pzt
T	Surface traction (3)
T	Time
T_0	Ambient temperature
T_t	Total transmission time
TB	Time-bandwidth product
u_r, u_θ, u_z	Displacement (4.6.2)
V	Particle displacement (3)
V_n	Voltage of rail n
V_{pp}	Peak to peak voltage
x	Propagation distance (2)
$x, x(t)$	Excitation signal (3)
$y, y(t)$	Recorded signal
z	Position along waveguide
z	Cylindrical plane (4.6.2)
$+Z, -Z$	In-plane motion vectors (3)

Chapter 1

Introduction

1.1 History

Sound plays a part in our lives that is scarcely less important than light or motion. It may be surprising to the reader then that our now vast knowledge of the mechanics of sound is relatively new. Despite huge advances in the understanding of optics, astronomy and classical mechanics during the Islamic golden age (769-1258), little attention was given to the physics of sound except for the first estimations on the speed of sound by Abū Rayhān al-Bīrūnī [9].

In fact, beyond simple observations by Pythagoras (600 BC) [10] about the relation of pitch to the length of a vibrating string, the vibratory nature of sound wasn't discovered, albeit accidentally, until 1638 by Galileo. In "Discourses Concerning Two New Sciences", published in the same year, he describes how a pure tone can be produced by dragging an iron chisel across a brass plate [11]. Notably, he found that the indentations left by the chisel were closer together when the pitch was high. He expressed that a relation is to be found in the number of vibrations per unit time, which we now call frequency.

The next 250 years brought with it volumes of publications that describe the linear behaviour of sound in gas, including reflection, diffraction and attenuation. The most significant of these works perhaps being Lord Rayleigh's, "Theory of Sound" [12]. His work introduced a number of complex surface waves including Rayleigh and whispering gallery waves. Lamb, who was greatly admired by Rayleigh, would later theorise the existence of a more complex

multi-modal highly dispersive wave [13]. Sadly, he died before the identification of the Kramers–Kronig relation and the invention of the modern computer which have both made Lamb waves so prolific in everyday non-destructive testing (NDT).

Lamb waves are just one example of small signal acoustics that are highly dispersive, and so unlike regular wave propagation their speed of sound varies greatly with frequency. At large finite amplitudes, sound exhibits additional nonlinearities as the localised acoustic pressure changes the material's density. Unlike the regular wave equation, its one-dimensional analysis includes a position term. This 3rd order differential equation has its own dedicated body of literature called *nonlinear acoustics*. This thesis, also considers this nonlinear phenomenon. To better distinguish the two, nonlinear will always appear italicised with a footnote explanation when referring to *nonlinear acoustics*[1].

1.2 Scope

This thesis concerns itself mostly with two particular areas of ultrasound: guided wave testing and high intensity focused ultrasound (HIFU). In both of these areas, observation of nonlinear phenomena is both critical and commonplace, so they serve as excellent examples for this thesis. Whilst the reader may be familiar with more common modes of ultrasound, such as ultrasonography, there are important differences with these modalities that must be described first.

Guided waves are used in non-destructive testing to inspect *thin* structures, which usually means that the material (waveguide) thickness is close to, or less than, one wavelength. Unlike regular ultrasonic NDT, where bulk waves are used to find features in the elevation direction of the transducer, guided waves travel perpendicular to the thin dimension. Because the waveguide boundaries are so close, and the attenuation is low, these waves are useful for inspecting long structures such as pipes or heat exchangers [14]. As with many oscillating systems, the guided waves have multiple anti-symmetric and symmetric modes. Their relationship between the speed of sound and frequency is extremely

[1]Nonlinear propagation induced by sufficiently large amplitudes

nonlinear.

HIFU is a form of therapeutic ultrasound wherein a focused transducer is used to non-invasively heat tissue inside the body. With low intensities, perfusion can be increased, but it is more common to use higher intensities, where cavitation and thermal ablation can be caused which is useful to treat a variety of diseases [15]. The temperature rise is related to the tissue attenuation which has a nonlinear relationship with frequency. *Nonlinear propagation*[1] also adversely occurs, due to the high pressures involved.

1.3 Motivation

With the exception of the development of guided wave testing in the 90s, these nonlinearities have had little consequence for imaging and were neglected until recently. Conversely, for high intensity focused ultrasound (HIFU), where the pressures used are commonly two orders of magnitude higher, nonlinear propagation has been greatly studied [16]. However, with the ever-increasing frequencies used in imaging, nonlinear phenomena should now be taken into consideration, for example, when designing matched filters [17]. Similarly in the HIFU field, while there is a great ambition to miniaturise and reduce the cost of the excitation hardware, the effects this has on any nonlinear phenomena should be considered.

Various successes in transducer, hardware and software design have lead to the miniaturisation of NDT and medical ultrasound scanners. Unfortunately, this has needlessly impaired ultrasound research because these systems do not allow reconfiguration of the transmit, receive or processing sequences. In response, academics and engineers have triumphantly developed their own open platforms [18] such as University of Bristol's *Ultraino* [19], University of Florence's *ULA-OP* [20] and University of Leeds' *UARP* systems [8], [21].

These highly flexible architectures continue to produce novel imaging techniques [22], but the focus has mainly been on two and three dimensional cardiac and vascular imaging, where the propagation of sound is mostly linear.

[1] Nonlinear propagation induced by sufficiently large amplitudes

1.4 Objectives and Organisation

Advances in signal processing and electronic design make it possible to use new post-processing algorithms and more complex transmit sequences to control, monitor, and observe the nonlinear propagation of waves. However, the task remains non-trivial, and careful consideration should be given to the transmission frequency, bandwidth and pressures to achieve the desired experimental behaviour. In this thesis, signal processing algorithms and custom transmit/receive sequencing are combined to control and/or observe the propagation of complex nonlinear ultrasonic waves.

Chapter 2 first introduces the hardware used in this thesis. Switched excitation is used exclusively and the implications for nonlinear wave propagation is considered. With this in mind, the transmit capabilities are extended to facilitate ultra high-frequency imaging (60 MHz) and high-intensity focused ultrasound (3.3 MHz). The results of this study were published in:

- C. Adams, D. M. Cowell, L. Nie *et al.*, 'A miniature HIFU excitation scheme to eliminate switching-induced grating lobes and nullify hard tissue attenuation', in *Ultrasonics Symposium (IUS), 2017 IEEE International*, IEEE, 2017, pp. 1–4.

- D. Cowell, T. Carpenter, P. Smith *et al.*, 'Modified harmonic reduction pulse width modulation (mHRPWM) for switched excitation of resonant HIFU transducers', in *Ultrasonics Symposium (IUS), 2018 IEEE International*, IEEE, 2018, pp. 1–4.

In the next chapter, the flexibility of the UARP transmit is leveraged to automate guided wave inspection in plates. A methodology is developed that allows the enhancement of the direction of guided waves without the need for parameters to be known. The results of this study were published in:

- C. Adams, S. Harput, D. Cowell *et al.*, 'An adaptive array excitation scheme for the unidirectional enhancement of guided waves', *IEEE transactions on ultrasonics, ferroelectrics, and frequency control*, vol. 64, no. 2, pp. 441–451, 2017.

- C. Adams, S. Harput, D. Cowell *et al.*, 'Specimen-agnostic guided wave inspection using recursive feedback', in *IEEE International Ultrasonics Symposium (IUS)*, IEEE, 2016.

Chapter 4 continues on the theme of guided waves by describing a new beamforming technique for measuring phase velocity dispersion. The technique is applied to the assessment of cortical bone ex vivo and in vivo. Another technique for measuring skull's acoustics properties using a transcranial array was also devised. As a result, the following was published:

- C. Adams, S. Harput, D. Cowell *et al.*, 'A phase velocity filter for the measurement of Lamb wave dispersion', in *IEEE International Ultrasonics Symposium (IUS)*, IEEE, 2016.

- C. Adams, J. R. McLaughlan, L. Nie *et al.*, 'Excitation of leaky Lamb waves in cranial bone using a phased array transducer in a concave therapeutic configuration', *The Journal of the Acoustical Society of America*, 2017.[1]

- C. Adams, J. McLaughlan, L. Nie *et al.*, 'Excitation and acquisition of cranial guided waves using a concave array transducer', in *Proceedings of Meetings on Acoustics 173EAA*, ASA, vol. 30, 2017, p. 055 003.[2]

Finally, in an extension to chapter 2, methods for lesioning using switched excitation are explored in chapter 5. An electronics design and associated switching algorithm are presented to miniaturise and reduce the cost of HIFU array systems. This body of work resulted in the following publications:

- C. Adams, T. M. Carpenter, D. Cowell *et al.*, 'HIFU drive system miniaturisation using harmonic reduced pulse width modulation', *IEEE transactions on ultrasonics, ferroelectrics, and frequency control*, 2018.[3]

- T. M. Carpenter, C. Adams, S. Freear *et al.*, *Five Level Switched High Intensity Focused Ultrasound Driver Design*, Jul. 2018.[4]

[1] Conference presentation
[2] Editor-reviewed publication
[3] Accepted for publication, available pre-print on IEEEXplore `https://doi.org/10.1109/TUFFC.2018.2878464`
[4] Online document repository

Chapter 2

Evolutionary Approach to Switched Waveform Design for Frequency-Dependent Propagation

This thesis uses two bespoke ultrasound systems built at the University of Leeds. Both use 5-level switched excitation circuits, which improves the efficiency and reduces the size of the systems. However, if consideration is not given to the switched waveform design, harmonics will be introduced within the bandwidth of the transducer. There are implications of this for frequency-dependent waveform propagation, which will be discussed in this chapter. Following this, the two ultrasound systems are introduced and waveform design methodologies for controlling acoustic pressure, including harmonically reduced pulse width modulation (HRPWM), are discussed. Although HRPWM has superior spectral performance, it is found that hard limitations on the switch timing make a number of its waveforms unusable. To find possible solutions with the required amplitude control and harmonic reduction, a genetic algorithm (GA) was employed to search the large space. The number of possible amplitudes, or *granularity*, that could be generated using the GA was measured experimentally. A low percentage granularity indicates a fine control of the amplitude. When HRPWM was supplemented with waveforms

from the GA, at 1.1 MHz the granularity was reduced from 2.7 % to 1.3 %. At 3.3 MHz HRPWM could not achieve any control of amplitude, but the GA was able to achieve a granularity of 2.1%. This improvement allows finer control of acoustic intensity in HIFU array applications, which could reduce treatment time.

2.1 Introduction

The dimensions of piezoelectric (PZT) elements in ultrasonic array transducers are constrained by requirements for lateral resolution and frequency response, which in turn influences axial resolution in imaging. This means that array element dimensions are typically on the order of 10 µm. Because the array elements are this small, the excitation circuitry needs to deliver large voltages to the PZT to achieve the desired pressures necessary for imaging [24]. In therapeutic devices, the array elements are larger so require smaller excitation voltages but are excited continuously at much higher total powers. Therefore, the design of electronics for imaging and therapeutic systems pose challenges.

A number of electronic designs are available for ultrasound systems that vary in complexity and features. The simplest are pulser circuits, where a high voltage, usually negative, pulse with a very short duration and rise time is applied to the transducer. This causes the PZT to resonate naturally and produce acoustic energy according to its bandwidth. For simple biomedical and NDT imaging applications, this may suffice. However, the improvements in SNR that can be obtained by using sinusoidal or chirped excitation makes alternative designs highly desirable [25]. Pulsed excitation is also not suitable for therapeutic applications where continuous wave (CW) operation is required to achieve the necessary increase in temperature. Traditionally, these requirements have been met with linear amplifiers. In this configuration, the amplifier's switches, (MOSFET, GAN etc) are operated in their unsaturated, linear region so that a fixed gain is applied to the input. Transformers may also be included at the output stage to convert the power to a higher voltage [26]. Naturally, the circuit also requires some waveform generator such as a DAC to generate the desired input.

With switched excitation, the transistors are instead operated in their fully saturated region. Here, the input of each transducer is connected to transistors that rapidly switch between a discrete number of voltage levels to approximate the desired waveform. This may be referred to as any combination of class d, e or f amplifiers[1]. The distinction between the classes is often subtle, although Class-D generally uses two transistors and the output is nonlinear[2]. Class-E if more efficient and uses only one transistor with a filter, with class-F being similar but with filters designed to reflect some harmonics, making transistor parasitics permissible [28]. Designs with any combination of these classes also exist. These types of amplifiers may feature an input stage, as is often the case with consumer audio amplifiers. However, in ultrasound systems, the source is usually virtual and the excitations are generated by a digital device such as a micro-controller or an FPGA.

The advantages of these circuit topologies are numerous [29], [30]. Improvements in efficiency can be yielded, which in turn reduces thermal management requirements and thus system size. Switched excitation circuits also tend to be less expensive to manufacture, which is perhaps responsible for the ubiquity of class-D and class-DE audio amplifiers [31]. An example of a multi-level switched circuit is shown in figure 2.1. It features two positive levels (V_2, V_1), two negative ($-V_1$, $-V_2$) and a clamp circuit (blue) that is designed to return the output to 0 Volts. Each switch output is connected to a common input on the transducer element (red).

Although switched excitation offers many of the aforementioned improvements, the rapid switching inevitably spectrally distorts the signal. So as to minimise this, the switching frequency is typically set to be much higher than the frequency response of the connected load. Additional power filters may also be employed to further improve signal purity. But these are large and limit the bandwidth of the waveform and transducers that can be used. Also, because of the current speed capabilities of transistor technologies, relative to the frequencies used in ultrasound (20 kHz - 100 MHz), there is a limit on the number of switching events that can occur per excitation cycle. This means

[1] M. M. El-Desouki and K. Hynynen, 'Driving circuitry for focused ultrasound noninvasive surgery and drug delivery applications', *Sensors*, vol. 11, no. 1, pp. 539–556, 2011.

[2] The output voltage does not follow the input voltage in a linear fashion

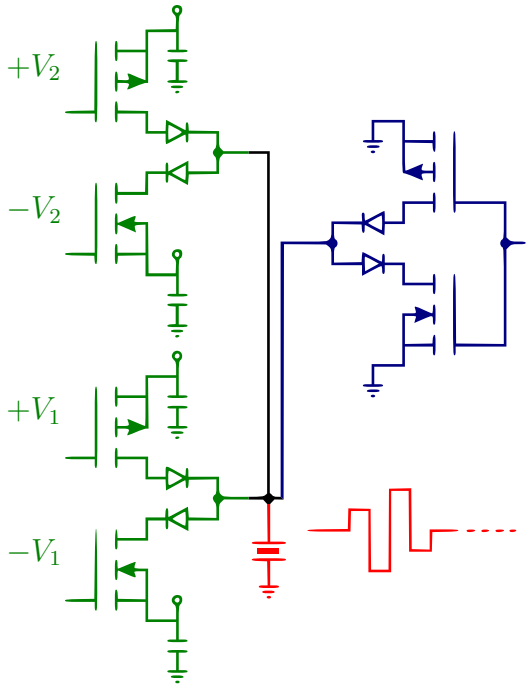

Figure 2.1: A simplified example of a multi-level switched circuit. The green circuity is used to switch the circuit between the discrete voltage levels $-V_1$, $+V_1$, $-V_2$ and $+V_2$. The blue circuity is used to clamp the transducer to ground. In red, the circuit output is connected to the transducer element without the use of a filter.

any generated harmonics may be within, or close to the effective bandwidth of the transducer. For this reason, a number of authors have proposed solutions to the problem of harmonic generation for ultrasound applications [32]. A range of these schemes are discussed and tested for therapeutic applications in chapter 5. The rest of this chapter serves three purposes:

1. To introduce the hardware used and the harmonic reduction technique that is used throughout the thesis.

2. To consider the effect harmonic distortion from switched circuits has on phased arrays and problems of frequency dependent propagation phenomena.

3. To propose a new approach to switched waveform design using genetic algorithms.

2.2 UARP Technology and HRPWM

This thesis owes its experimental results to two bespoke ultrasound systems developed at the University of Leeds which are shown in figure 2.2. The Ultrasound Array Research Platform II (UARPII) [21] is shown on the left and the High Intensity Focused Ultrasound Array Research Platform (HIFUARP) [8] is shown on the right. They are both the result of development over several years. Table 2.1 shows a performance summary of the two systems.

The UARPII is a 128 channel imaging system and can be used for both NDT and biomedical applications. The HIFUARP is a 16 channel array system with each driving circuit capable of 41 W continuous use. Both systems are extremely flexible and allow truly arbitrary sequencing of transmit and receive. These systems use switched excitation and were designed to use a Harmonic Reduced Pulse Width Modulation (HRPWM) algorithm to excite the transducers, although this is not imperative and other methodologies may be used.

Left: Ultrasound Array Research Platform II (UARP II).

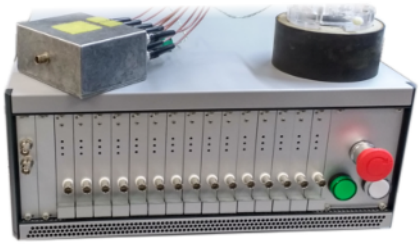

Right: High-Intensity Focused Ultrasound Array Research Platform (HIFUARP).

Figure 2.2: Ultrasonic array systems used throughout this thesis.

Table 2.1: System specifications

	UARP II	HIFUARP
Max. continuous transmit time	100 ms	40 s
Maximum voltage	200 V	48 V
Receive sampling frequency	80 MHz	TX only
Max. transmit frequency	160 MSps, 15 MHz TX	160 MSps, 4 MHz TX
Transmit technology	5 level with IC pulsers	5 level with discrete MOSFETs
Channels	128	16
Maximum power per channel	< 1 W	41 W

Figure 2.3 shows examples of several existing switching schemes. Each is compared with an ideal 70% amplitude sine wave. The maxima of this sine wave is used as a reference for the corresponding periodograms. $+V_2$, $+V_1$, GND, $-V_1$ and $-V_2$ represent the voltage rails used and are set to 1, 0.5, 0, -0.5 and -1 respectively. The most harmonically distorted scheme, bi-level, is shown in 2.3a. Here, the harmonics are large compared to the fundamental component, with f_3, the third harmonic being only 10 dB less than the fundamental. Since this is the most intense and likely has the largest ramifications of all the harmonics, reducing its magnitude is the focus of the switching schemes presented here.

The rest of the graphs in 2.3 show other schemes. Continuing down the page, the first is third harmonic reduction (3HR) (figure 2.3b)[1]. Here the angles are fixed to remove the third harmonic symmetry. Following this is staircase excitation which works by approximating the sine wave in a quantised manner. The addition of extra levels naturally disrupts the generation of harmonics. Finally, HRPWM[2] is shown, which extends the harmonic reduction used in 3HR with the addition of amplitude control. Because of this amplitude control, f_1 has a power of 0 dB unlike others in the figure. This makes it highly useful in array applications where apodisation is required, as all the elements can be connected to a single power supply. Like 3HR, the angles are still set to reduce the third harmonic, but critically it is able to modulate its amplitude of the fundamental component. Reduction of the third harmonic is often more effective than with staircase excitation as the latter relies on incidental rather than systematic disruption of symmetry. Crucially, HRPWM can perform this harmonic reduction at peak amplitudes below V_1, where staircase cannot.

[1] S. C. Tang and G. T. Clement, 'A harmonic cancellation technique for an ultrasound transducer excited by a switched-mode power converter', in *Ultrasonics Symposium, 2008. IUS 2008. IEEE*, IEEE, 2008, pp. 2076–2079.

[2] D. Cowell, P. Smith, S. Harput *et al.*, 'Non-linear harmonic reduction pulse width modulation (HRPWM) for the arbitrary control of transducer-integrated switched excitation electronics', *2014 IEEE International Ultrasonics Symposium*, 2014. DOI: 10.1109/ultsym.2014.0198.

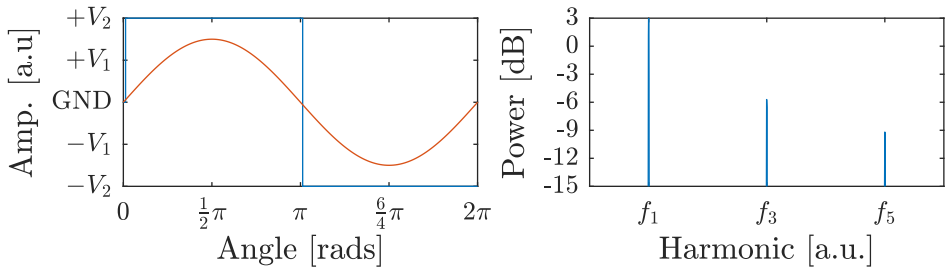

(a) Bi-level excitation

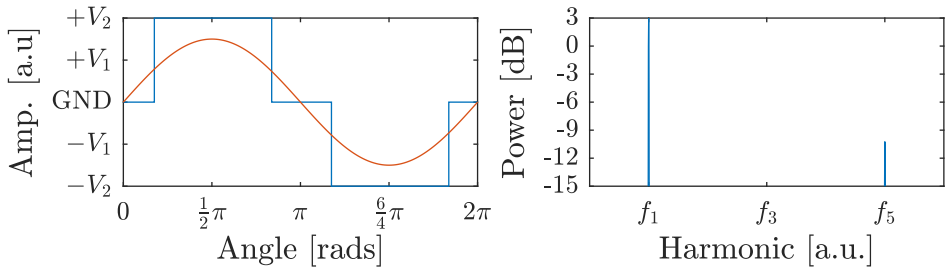

(b) Third harmonic reduced bi-level excitation

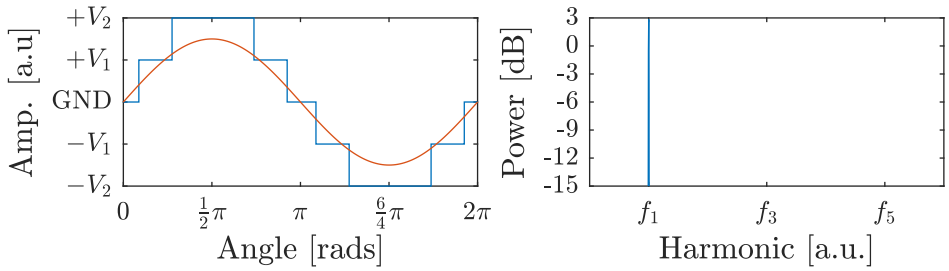

(c) Staircase excitation

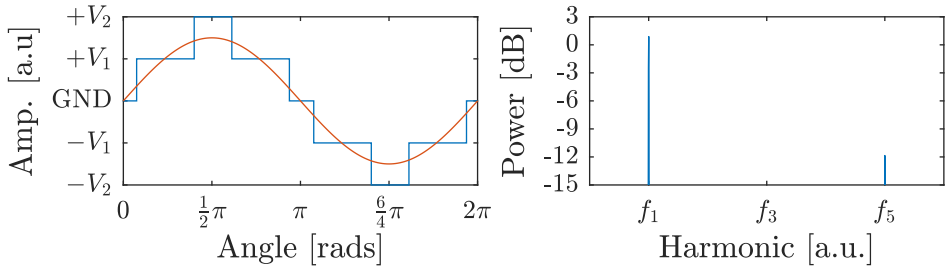

(d) HRPWM excitation

Figure 2.3: Time and frequency domain data for each of the excitation schemes. Each has differing levels of complexity and harmonic distortion. Each switching scheme is shown in blue and compared to ideal excitation made with a linear amplifier. The periodograms are calculated using the peak amplitude of the ideal waveform (shown in red).

2.3 Acoustic Consequences of Harmonic Distortion

Some harmonic reduction schemes allow for miniaturisation and integration of excitation circuitry into the transducer without the need for filters [33]. Without these schemes, the harmonic distortion may be converted to acoustic energy. The consequences of this are discussed in this section.

2.3.1 With Phased Arrays

Phased arrays refer to array transducers where the pitch, k, is approximately half the wavelength, λ, or less ($k < \lambda/2$). This spacing allows the transducer to build effective interference patterns in the near field for steering beams. Just as with moving or wobbling a single element transducer, this allows a particular area of interest to be sonicated [34], which has applications in NDT[1][36], therapeutic ultrasound[2] and biomedical imaging [34].

Unlike single element transducers, phased array transducers produce undesired field patterns that include grating lobes [38]. This has ramifications for all types of ultrasound including undesired heating during HIFU [39] and artefacts in imaging. These lobes have known relationship with frequency and speed of sound (SOS). It is known that at a given frequency and fixed pitch, that the grating lobe is always some fixed angle from the main lobe irrespective of the steering angle. To reduce these lobes, transducer pitch is usually minimised so that the grating lobe is not within the field of view and so is negligible.

The harmonics generated by switched excitation effectively have a smaller wavelength acoustically, because the frequency is higher, and so the pitch-wavelength ratio effectively becomes much larger for these generated harmon-

[1] B. W. Drinkwater and P. D. Wilcox, 'Ultrasonic arrays for non-destructive evaluation: A review', *NDT & E International*, vol. 39, no. 7, pp. 525–541, 2006, ISSN: 0963-8695. DOI: 10.1016/j.ndteint.2006.03.006.

[2] F. Xiaobing and H. Kullervo, 'Control of the necrosed tissue volume during noninvasive ultrasound surgery using a 16-element phased array', *Medical Physics*, vol. 22, no. 3, pp. 297–306, DOI: 10.1118/1.597603. eprint: https://aapm.onlinelibrary.wiley.com/doi/pdf/10.1118/1.597603.

ics:

$$\frac{k}{\lambda_h} = h \times \frac{k}{\lambda_1}$$

where h is the harmonic component number. These components then are more likely to produce lobes. They will be of most consequence when curved arrays, which are commonplace in HIFU, are used because the lobes will be within the field of view (FOV). To test this, a typical prostate HIFU array [40] was simulated in Field II [41]. The concave array consisted of 64 elements, where each was 50 mm in height, 1.5 mm in width and 167 µm of kerf separated them. The array elements were distributed on an arc with a radius of 100 mm. The geometric focus of the transducer was at 0 mm laterally and -100 mm axially. The excitation for the array was a 1 MHz continuous wave, and phase shifts were applied to focus the beam at -30 mm laterally and -70 mm axially. To reduce simulation time, only part of the field of view was simulated. Figure 2.4 depicts the transducer, its focal points and the simulation area.

The impulse response of a 10 element HIFU transducer (Imasonic, France) [42] was obtained using a 1 mm needle hydrophone (Precision Acoustics Ltd, UK). The hydrophone was placed at the transducer natural focal point and the peak excitation voltage was kept under 20 V to reduce the effects of any *nonlinear propagation*[1] (PPP $<$ 1.5 MPa). This impulse response was input into field II to improve modelling accuracy.

Four different excitation schemes were considered; analogue, bi-level, 3HR and HRPWM. Linear amplifier excitation (pure sine) was defined as,

$$a(t) = \sin(2\pi f t) \tag{2.1}$$

where f is 1 MHz. The bi-level excitation was formed by finding the sign of the analog excitation:

$$a(t) = \text{sgn}\{\sin(2\pi f t)\} \tag{2.2}$$

[1]Nonlinear behaviour introduced by large signal amplitudes

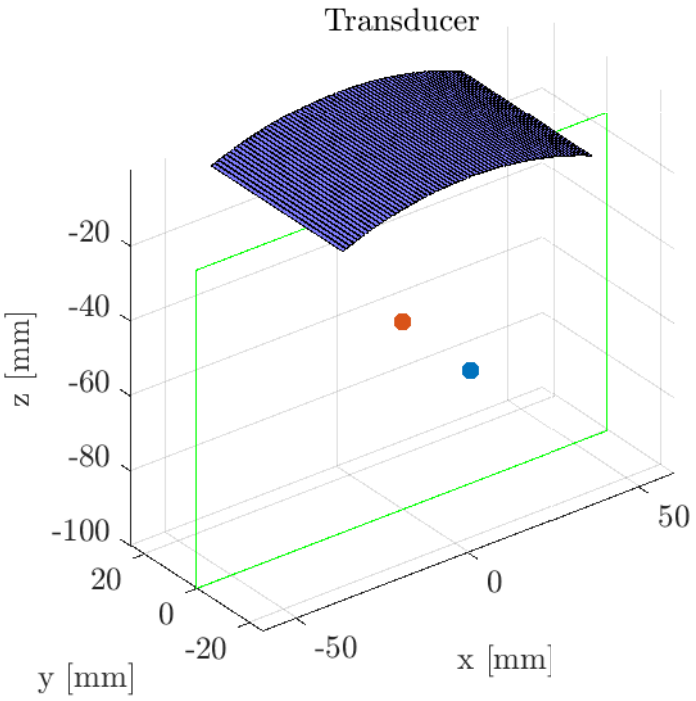

Figure 2.4: The geometry of a curved array HIFU transducer used in the simulation. The natural focus of the transducer is shown by the red dot (0,0,-100 mm). Phase delays were applied to each element so that the energy was focused on the blue dot (-70,0,-30 mm). The green square shows the actual area that was simulated.

Third harmonic reduction is defined as

$$a(t) = \left\{ \begin{array}{rl} 1, & \text{for } \sin(7\pi/6) < \sin(2\pi ft) \geq \sin(\pi/6) \\ 0, & \text{for } \sin(7\pi/6) \leq \sin(2\pi ft) \geq \sin(\pi/6) \\ -1, & \text{for } \sin(7\pi/6) \geq \sin(2\pi ft) < \sin(\pi/6) \end{array} \right\} \tag{2.3}$$

3HR and bi-level have a fixed amplitude, so any changes to amplitude must be achieved by changing the electrical configuration. HRPWM comprises multiple DSP stages and is difficult to represent analytically. Fundamentally, it involves modulating PWM switching angles in a manner that modulates the desired amplitude of the fundamental component of the signal without forming undesired 2nd or 3rd harmonics. The waveforms may be truly arbitrary in frequency and amplitude.

Figure 2.5 shows the beam profiles for all the excitations. To create a beam profile, the PPP was obtained at each point then the absolute maximum for all tested points was used as a reference to convert the image into relative intensity. The sampling frequency used in the simulation was 100 MHz. Each excitation and image used its own unique reference. The highest, 12 dB, is shown in the images. All excitation schemes correctly focus the beam to a small point (dictated by the diffraction limit). For the analogue excitation, there is little energy outside of the focal spot. For the bi-level excitation, harmonics form a grating lobe of approximately -12 dB relative intensity. Both 3HR excitations and HRPWM reduce the magnitude of this energy, with HRPWM performing best at removing energy outside the focal region.

Table 2.2 summarises the suitability of each of the considered excitation schemes for use with phased arrays. Linear amplifier is the gold standard as it can achieve amplitude control, and it has no harmonic distortion, and thus no grating lobes. However it does not have the aforementioned benefits of switched excitation. When simple bi-level switched excitation is used efficiency can be improved, but it produces grating lobes and cannot achieve amplitude control with a fixed power supply. 3HR can remove these grating lobes and is still efficient but still cannot achieve amplitude control. Of the switched schemes considered, HRPWM is best because it can achieve harmonic reduction, amplitude control and uses an efficient switched-based architecture.

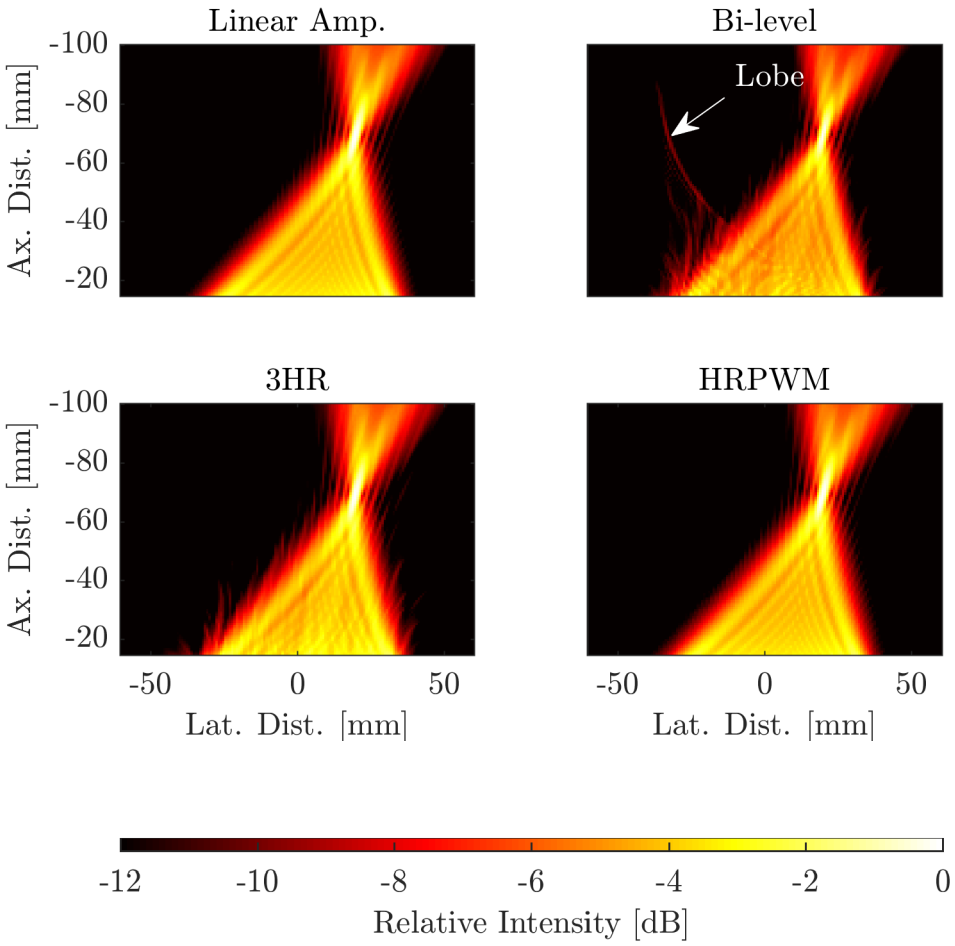

Figure 2.5: Beam profiles of a concave focused HIFU transducer when different excitation schemes were used. Bi-level has lots of acoustic energy in harmonics which form grating lobes that deposit energy outside the focal region. 3HR and HRPWM schemes were able to reduce the amplitude of the grating lobes.

Table 2.2: Performance of each scheme when used to excite a phased array.

	Amplitude control	Grating lobe removal	Switch-based
Linear amplifier	✓	✓	
HRPWM	✓	✓	✓
3HR		✓	✓
Bi-level			✓

2.3.2 For Nonlinearities

All waves are subject to nonlinear, frequency dependent effects. However, the severity depends on the medium, and the conditions of propagation (eg, Lamb, bulk etc). The harmonic distortion prevalent in switched excitation may have a profound effect on wave propagation. Relevant phenomena and the associated implications of a distorted signal are discussed below.

Frequency-Dependent Attenuation Scattering and absorption are the two mechanisms that constitute the attenuation of sound. Absorption is the process that converts sound into heat. Scattering is when sound deviates from its path because of localised non-uniformities in the medium. Both are complex frequency related phenomena that reduce the intensity of a propagating wave. The intensity of a propagating plane wave can be described by

$$\bar{I}(x) = \bar{I}(0)e^{-1(\alpha_s+\alpha_a)} \tag{2.4}$$

where $\bar{I}(0)$ is the initial intensity at the start of the medium and x is the distance travelled in the medium. α_s and α_a describe the scattering and absorption coefficients respectively. Mediums such as pure liquids may be dominated entirely by attenuation, but biological tissues and solid materials are rarely comprised of just one mechanism [38]. A good approximation for the frequency dependence of combined attenuation, $\alpha = (\alpha_s+\alpha_a)$ can be described by the equation:

$$\alpha = \alpha_0 \times f^n \tag{2.5}$$

Where f is frequency in MHz, n is between 1 and 2, and α_0 is the attenuation coefficient at 1 MHz. This strong frequency dependence means propagating acoustic waves that contain harmonic distortion will exhibit pressure loss at a faster rate (with distance) than non-distorted waves. At therapeutic intensities, this could result in undesired pre-focal heating and will be explored further in chapter 5. For imaging, this reduces the strength of an echo at a given fixed PPP.

Dispersion Dispersion refers to the propensity for different wavelengths to have differing phase velocities. For plane waves travelling in tissue, this means that temporal spreading of the wave occurs when either a broadband pulse or frequency modulated signal is used. The Kramers-Kronig relation has been used to build accurate models that relate attenuation and dispersion in solids and fluids[43]. Therefore, because the attenuation in water is quite low compared with other fields of study, dispersion is of little consequence in tissue at low frequencies [44], [45]. However, the same cannot be said of guided waves where the relations are considerably more complex. These waves travel at the surface of structures and consist of multiple oscillatory modes which in turn, have their own relationship between frequency and velocity. An infinite number of modes with different speeds exist. At high frequency-thickness products it is possible for several modes to exist at a given frequency. However, practically, because of attenuation and spatial sampling limitations, it is difficult to observe more than a few at one time. In NDT, these waves can be leveraged for inspection [46] because of the unique way they interact with defects in thin structures and biomedically, they are being used to assess bone [47]. Harmonic distortion in the acoustic waveform could extenuate certain modes of oscillation.

Shockwave Formation At sufficiently high pressures, the normal wave equations that govern wave propagation become unsuitable as the propagating wave begins to influence the local density of the medium in which it is propagating. Instead, *nonlinear* equations must be used[1]. In *nonlinear* acoustics, the pressure maxima are sufficiently large that they increase the density of the medium they are travelling in, and thus travel faster than the rest of the wave. Conversely, the minima travel slower. This effect distorts the waveform and simultaneously generates harmonics at the same time. This effect continues as the wave travels through the medium until shock waves are formed. Shockwaves have extremely short rise times, which enhances heat deposition. The heating from a non-shocked wave can be described as

$$H_{\text{lin}} = 2\alpha I \tag{2.6}$$

[1]Nonlinear propagation induced by large amplitudes.

Whereas the heating from a shocked wave is described by,

$$H_{\text{shock}} = \beta f_0 A_s^3 / 6 c_0^4 \rho_0^2 \tag{2.7}$$

where f_0 is the initial frequency, β is the coefficient of nonlinearity, A is the amplitude of the shock wave, c_0 is the normal SOS in the medium and ρ_0 is the nominal density. Shock waves are usually short-lived because they are rapidly attenuated. This causes pre-focal deposition of energy [16] and as such are usually avoided, although they have uses in histotripsy [48].

The blue line in figure 2.6 shows some of the stages of shock-wave formation:

- Close to the source, the waveform propagates in a linear fashion. (top in the figure)
- Some distance away from the source the wave begins to exhibit nonlinear behaviour as the wave becomes more sawtooth-shaped. (middle)
- The rise time of the waveform continues to decrease until the waveform is "shocked". (not shown)
- Further on, the high harmonic content of this waveform is rapidly attenuated and the amplitude is reduced.

This figure was made using 1D analysis in k-wave, a nonlinear pseudo-spectral simulation package [49]. The source pressure and frequency were 30 MPa and 1 MHz respectively, which are typical values used in lithotripsy [50]. The medium properties were set to be representative of generic tissue [51].

The significance of this phenomena to switched excitation is that the shock wave formation distance, $\bar{x}$, is frequency dependent:

$$\bar{x} = \frac{\rho_0 c_0^3}{\beta P_0 2\pi f} \tag{2.8}$$

Or approximately in tissue, 100 mm / (MHz MPa). This means that the distorted components of the acoustic waveform (as a result of distortion of the electrical waveform) will shock before the fundamental component. The red coloured waveform in figure 2.6 shows what happens to shock wave formation when harmonic distortion (30% when $f = 3 \times f_0$) is introduced. At 50 mm,

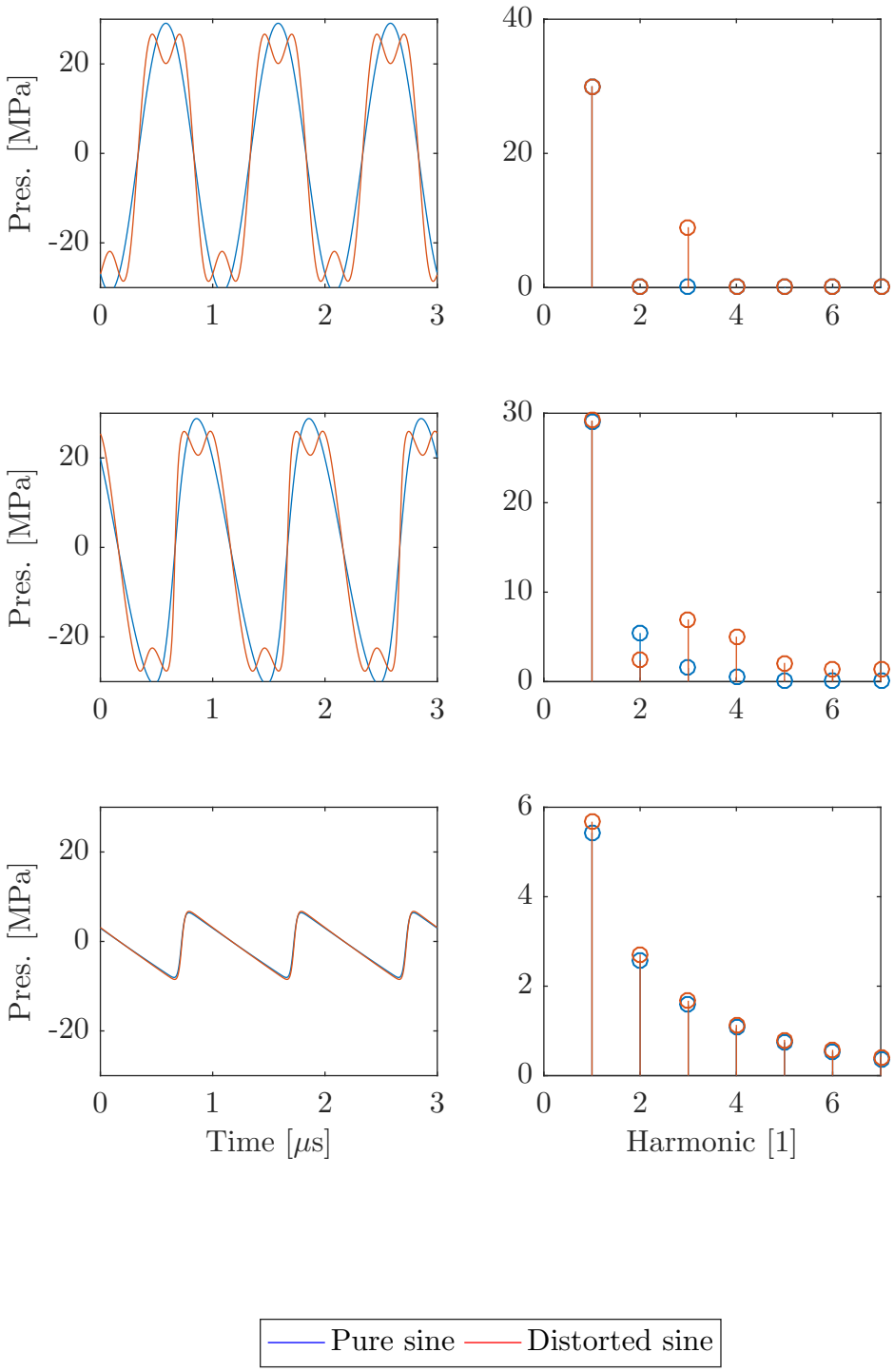

Figure 2.6: Shockwave formation of acoustic waves with and without distortion caused by switched excitation, at the source (top), 2 mm from the source (middle), and 50 mm from the source (bottom).

there is more harmonic content at the third and fourth harmonics compared to when an ideal sine wave was used, but after the shock wave begins to be absorbed, the magnitudes of these harmonics are equal. This means that they were absorbed and converted to heat, which may or may not be desired.

2.4 Evolutionary Design of Switched Waveforms

The previous section described a number of scenarios where distortion in the acoustic wave, brought about by switched excitation, may influence wave propagation. In addition to the desire for selective harmonic reduction, there may be additional constraints on the timing of switched waveforms. For example, consider figure 2.8 which shows one cycle of a switched waveform (red) sampled at 160 MHz. The green markers represent the time that the gates of all transistors must be switched off, *dead time*. The length of time depends on the MOSFETs used and is often anti-symmetric if P and N-type switches are used. It is necessary because there is a delay between the gate of a MOSFETs being turned off and the output actually turning off. If dead time is not used after a transistor turns off and another turns on, the two transistors will short two of the supply rails.

This requirement then limits the validity of some waveforms because they may require transitions during the dead time or any added dead time may overlap. Consider also that due to the varying specification of transducers, the harmonic reduction is not always necessary, and in fact, some harmonic reduction could be sacrificed in order to achieve finer control over the amplitude which is necessary for array applications. This is demonstrated in figure 2.7 which shows the centre-normalised frequency response for a number of common transducers. The selected harmonic to be eliminated may also change, for example with dual mode use arrays (DMUA) [52] where the bandwidth is highly unconventional. Indeed it may even be desirable to accentuate certain harmonics in order to excite the transducer at a higher centre frequency than could be achieved otherwise. The number of requirements for switched excitation waveforms are therefore broad, numerous, and cannot be addressed by one universal design algorithm. However, the problem remains complex with

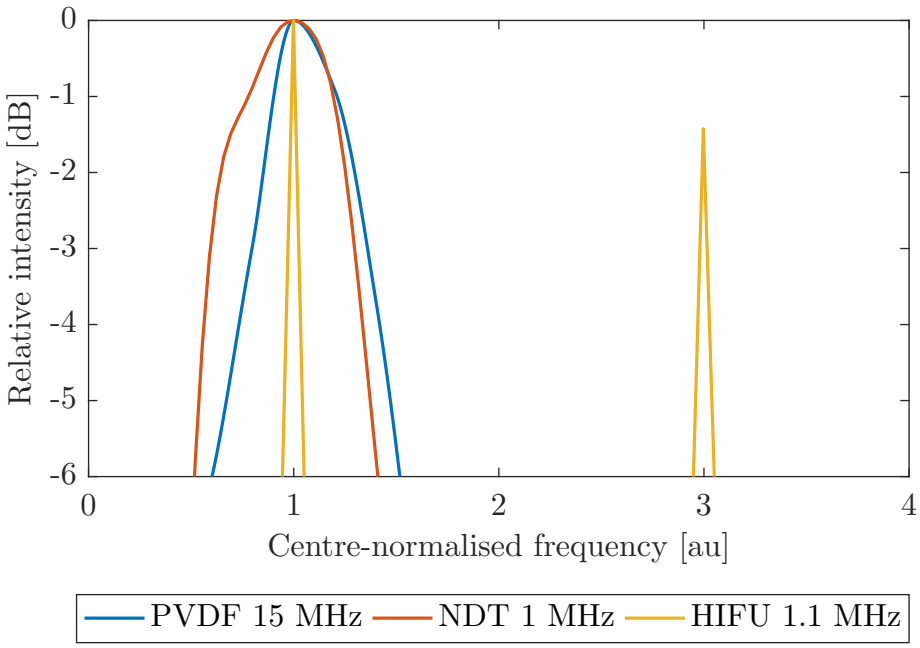

Figure 2.7: The frequency response of three different transducers. The PVDF and HIFU originate from their datasheets but the NDT response was obtained experimentally. The frequency axis is normalised for their centre frequencies.

objectives that are seemingly conflicting. It is prohibitively time consuming to derive a switched excitation from first principles every time there are new requirements.

In this work, it is proposed that a genetic algorithm (GA) may be used to generated switched waveforms. The GA will be applied to HIFU. Testing will be performed numerically and experimentally. Waveforms produced by the GA will hereafter be referred to as GAPWM.

2.4.1 Genetic Algorithm Operation

Consider figure 2.8 again which shows a generalised depiction of a 5 level waveform with 8 transitions. The variable δ represents the incremental angle between each transition. In other words, the first transition occurs at $0+\delta_1$, the second at $\delta_1 + \delta_2$ and so on. The role of the waveform designer, algorithmic or

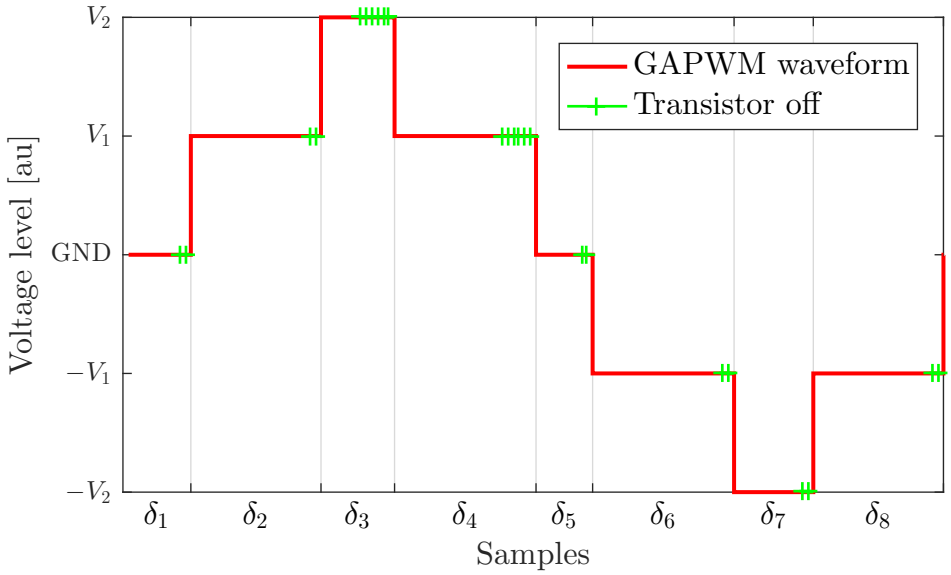

Figure 2.8: An example of a switched waveform. This one was produced by GAPWM. The green dots show the *dead time* period where the transistor must be switched off.

otherwise is to adjust these switching angles to achieve the desired magnitude of certain frequencies and minimise others. The problem, therefore, has a large number of dimensions (8 in this case).

Positive changes are represented by $\delta_{1,2,7,8}$ and negative ones by $\delta_{3..6}$. The systems described previously all use 5 level excitation circuitry and therefore only 5 levels are considered, but since the algorithm is highly parametrised there is no reason it cannot be adapted for any number of levels. The number of transitions is $(l-1)\times 2$ where l is the number of levels.

In total, 9 angles are optimised, 8 of which are shown in figure 2.8, with the ninth inferring the total length of the waveform. The unit for the angles is samples and $\delta \in \mathbb{Z}^{+}[0..f_s/f_c]$. A zero value is permissible because it allows the algorithm to consider missing levels as the waveform jumps to a level and then immediately to the next. For example, consider if δ_3 were 0, the waveform would transition to V_2 and then to V_1 0 samples later, with the latter taking precedence.

For a five-level waveform, the design search space is extremely large. For a 1 MHz single cycle waveform sampled at 160 MHz there are approximately

4.3×10^{17} possible waveforms. Genetic algorithms (GA) are extremely well suited to this type of problem. They are effective at traversing large, multi-dimensional search spaces to find optima using a limited number of tests. Although the only way to guarantee finding a global optima is by using an exhaustive search, the mutation operator in the algorithm has been shown to be often effective at avoiding local optima [53]. The proximity of solutions to the global optima depends on several algorithm parameters which are discussed later. A full explanation of the workings of genetic algorithms is beyond the scope of this thesis, and excellent literature already exists to explain them[1]. However, in brief, GAs mimic the process of biological evolution to find mathematical solutions. Abstractly, their operation is as follows:

1. Set the generation counter, $G = 0$
2. Create a population of random *genes* where each gene represents a possible solution to a mathematical problem.
3. Test each member of the population using a fitness function, $g(x)$ and assign a value that quantifies how well it solves the problem.
4. Produce offspring from the *fittest* members of the population. This produces genes with even more optimal solutions.
   (a) Some members may have random mutations to increase the diversity of the population. This helps to avoid local optima.
   (b) If elitism is enabled, extremely fit members will produce offspring asexually.
5. Increment the generation counter, G.
6. GOTO 3, or stop when some condition is satisfied.

A number of stopping conditions may be used, such as a maximum number of generations being reached. The trade off in this instant is increasing the likelihood of the algorithm finding an optima average change in the fitness of

[1] D. A. Coley, *An introduction to genetic algorithms for scientists and engineers*. World Scientific Publishing Company, 1999.

the fittest member, at a cost of increased execution time. For this reason, it may be desirable to monitor the average change in fitness [54].

There are also a number of critical parameters that need describing and defining. The crossover fraction defines what percentage of the next generation should consist of normal, sexually produced members. When the crossover fraction is 0, the next generation is made entirely of mutated members. Conversely, when it is set to 1, there is no mutation.

Elitism, which allows the fittest members to reproduce asexually guarantees that the fitness of the best member will not decrease between generations, at the cost of genetic diversity. Authors have shown that when applied to standard test problems, using elitism is more effective than optimising the crossover function [55].

In this implementation, the algorithm stops when either the average fitness is less than 1×10^{-3} over the previous 100 generations, or $G > 500$. This was chosen so solution-dependent stopping criterion weren't needed and there was high confidence that enough solutions were tested [54].

There is currently no consensus on the optimum population size for a problem, except that high dimensionality problems require a larger population [56]. Therefore to ensure that there was enough genetic diversity, the population size was set to be 500. Elitism was enabled for the top 20 fittest members, and the crossover fraction was set to 0.9, which is typical for the given population size [56].

Each parameter is described and defined in table 2.3.

The fitness function $g(x)$ used was as follows,

$$g(x) = \begin{cases} 450 \times 10^6 \times \Sigma_{i=1}^{8} \delta_i & \text{if } \Sigma_{i=1}^{8} \delta_i > f_s/f_t \\ 400 \times 10^6 & \text{if dead time overlaps} \\ 300 \times 10^6 & \text{if no transitions} \\ 250 \times 10^6 & \text{if } |\mathbf{A}_i - \mathbf{A}_{i-1}| > (V_2 - V_1) \cup \mathbf{A}_{i-1} = 0 \\ 200 \times 10^6 & \text{if } |\mathbf{A}_i - \mathbf{A}_{i-1}| > (V_2 - -V_1) \\ \Sigma \mathbf{E}_i^2 & \text{otherwise} \end{cases}$$

$\mathbf{A}$ refers to the generated time domain waveform consisting of I samples. $\mathbf{E}$

Table 2.3: Description of each GA parameter

Parameter	Description	Value
Population size	Number of solutions considered in each generation	500
Elitism	Fittest members reproduce asexually	True
Crossover fraction	Fraction of children that are created from parents and not from mutations	0.9
Stopping condition	Condition that must be met to stop the algorithm	$G < 500$ or $\|g(x_{n-100}) - g(x_n)\| < 1 \times 10^{-3}$

is the error in frequency magnitude between the switched waveform and the equivalent analogue excitation. **E** is calculated from the squared difference between the frequency responses of **A** and the an equivalent sinusoidal signal. $g(x)$ would then be exactly 0 when the frequency responses are the same. f_t is the target frequency. The algorithm attempts to minimise the fitness function.

The function can be used to sanitise the population of genes that produce untenable waveforms. Here δ_n is in samples and the first line (450×10^6) ensures that the waveform is not longer than one cycle. The next line ensures that the dead time does not overlap so the waveform is safe. Following this 300×10^6 is used if the waveform is completely empty, i.e. all levels have been skipped. 250×10^6 is assigned if there are any large transitions away from GND. This has been included to reduce overshoot although may not be strictly necessary. Similarly, waveforms with very large changes from V_2 to $-V_2$ or likewise are assigned a high fitness of 200×10^6. If all these conditions are met the assigned fitness is based on the previously described error, **E**. The decrementing nature of these values encourages the algorithm to improve the quality of its solutions and differentiate between the different failure conditions.

The frequency points of interest are application dependent and are calculated using the Goertzel transform. Since only the magnitude of a few frequencies is required, this z transform-based method was chosen over Fourier methods to improve the algorithm performance. Weighting may also be applied to indicate the preference for control of certain frequencies over others.

2.4.2 Experimental Method

The necessity of dead time limits the number of usable waveforms that the HRPWM algorithm produces for the HIFUARP. For a 1.1 MHz transducer, for example, HRPWM can only produce one valid waveform in the range 40-60%. For a 3.3 MHz transducer it cannot produce any.

To extend the transmit capabilities of the HIFUARP, to better support array applications, the algorithm was used in two ways, firstly to increase the amplitude granularity at 1.1 MHz and secondly to produce waveforms at 3.3 MHz. Waveform solutions were found in 1% increments at both frequencies. For the 1.1 MHz waveforms, the algorithm was set to eliminate the second and third harmonic. Whereas the $\frac{1}{3}$ subharmonic was minimised for the 3.3 MHz waveforms because this is where the transducer is sensitive (figure 2.7).

Using the solutions, 20 cycle waveforms were generated and then uploaded to the HIFUARP which was connected to a HIFU transducer (H-102, Sonic Concepts, USA) along with its matching network. With a membrane hydrophone (Precision Acoustics, UK), the acoustic waveform at the transducer focus was recorded for each GA excitation along with all usable HRPWM excitations. The transducer and hydrophone were placed in a tank of degassed and deionised water. To reduce the effects of *nonlinear propagation*[1], the rail voltages, V_2, V_1, GND, $-V_1$ and $-V_2$ were reduced to 12 V, 6 V, 0 V, -6 V and -12 V respectively. Although this was lower than what would be required to generate lesioning pressures, it reduced the effects of harmonic generation as a result of nonlinear propagation. This allowed the harmonic distortion of the signal as a result of the electrical waveform to be isolated and measured.

From the recorded waveforms, the magnitude of the selected frequencies was found using an FFT. The globally maximum observed peak pressure was used as a reference to represent each waveform by a dB value, and from this, the effective amplitude as a percentage of maximum was found by linear curve fitting. The process was as follows:

1. For each considered design waveform, the resulting acoustic waveform was recorded 16 times and then averaged.

[1]Nonlinear propagation caused by large signal amplitudes

2. Averaged data was then Fourier transformed to find the magnitude of the target frequency for each tested switched waveform.

3. Data were converted to relative intensity by using the global maximum magnitude as a 0 dB reference (at the target frequency).

4. Experimental results were then compared against constructed sinusoids to find the closest equivalent amplitude.

The constructed sinusoids were created in increments of 0.1%. The FFT length and sampling frequency were conserved. Waveforms that produce the same effective amplitude after this procedure fitting are considered superfluous and the duplicate is disregarded. For 1.1 MHz, the GAPWM is only being used to supplement HRPWM, so if one of the waveforms is produced by GAPWM and the other by HRPWM, the former was disregarded.

Figure 2.9 demonstrates the GAs operation. It shows the fittest solutions over several generations. Here, the GA is attempting to produce a 3.3MHz waveform with a 25% amplitude. The left-hand graph shows the frequency response for the waveform being tested on the right. Comparisons in both the frequency and time domain are made with the equivalent sinusoidal in grey. Generation 1 shows that at least one member produced a valid waveform ($\Sigma\delta < 2\pi$), but there is a lot of harmonic content which appears as side lobes in the frequency spectrum. Additionally, the amplitude is incorrect as the peak in the frequency domain is ≈ 10 dB, although it is a good first approximation. Five generations later, the peak amplitude begins to approach the correct value and the side lobes are significantly reduced. By removing the top level, the algorithm has found that it can meet the dead time requirements and the desired amplitude control. At the 100th generation, the algorithm has nearly found its optimal solution as it is no longer possible to visually discriminate the difference in amplitude in the frequency domain between the sinusoid and switched waveform.

2.4.3 Results

Figure 2.10 shows three further solutions produced by GAPWM at different amplitudes when $f = 3.3\,\text{MHz}$. Once again, the first three cycles are shown

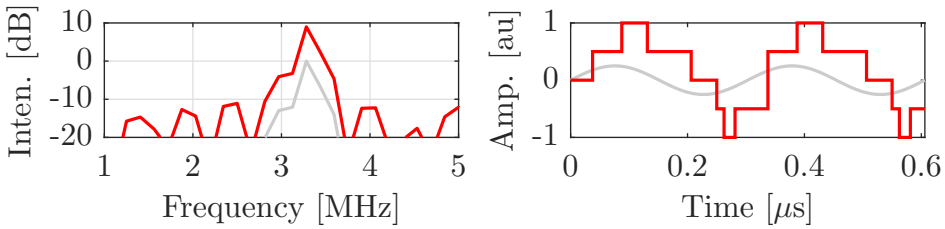

(a) Generation = 1

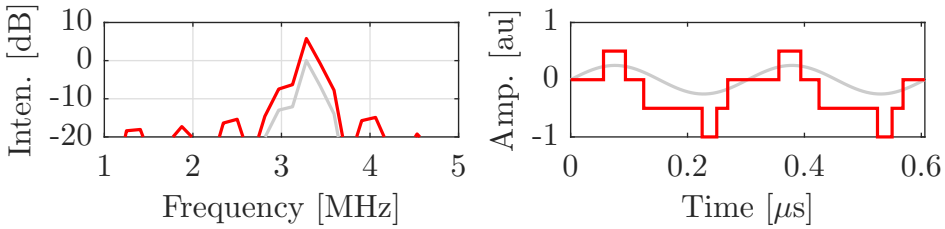

(b) Generation = 5

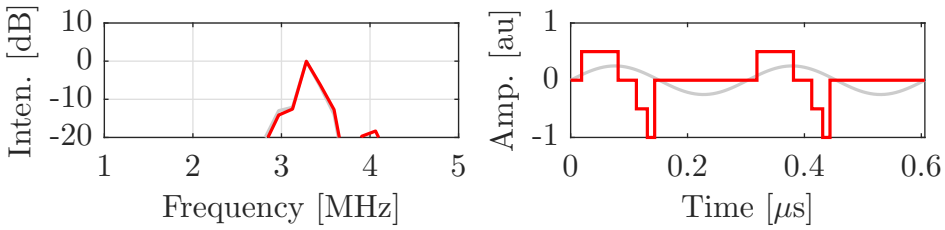

(c) Generation = 100

Figure 2.9: The GA improving the quality of its solution over several generations for 3.3 MHz waveform generation. The resulting waveform from the fittest member of generation 1, 5 and 100 is shown. The periodogram on the left shows the frequency content of the waveform. The corresponding waveform in the time domain is shown on the right. Results are compared with a perfect analogue excitation with an amplitude of 25% which is shown in grey.

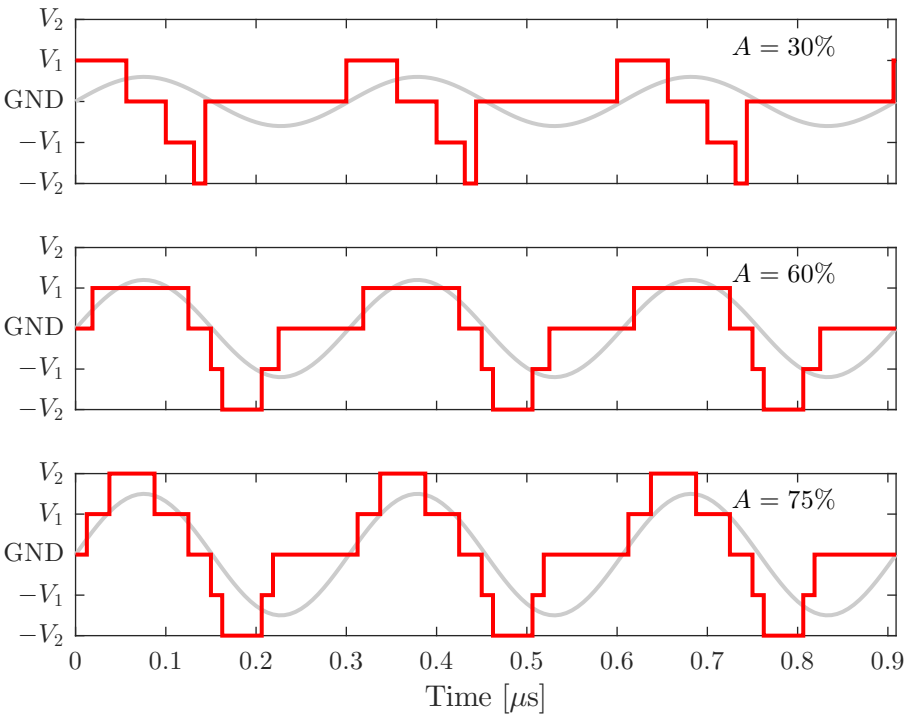

Figure 2.10: Example waveforms produced by GAPWM at different amplitudes when $f = 3.3$ MHz. The grey sinusoid shown in the background is of equivalent amplitude

along with a sinusoidal excitation at the equivalent amplitude (grey). The waveforms do not appear to have obvious form, progression or symmetry and would be difficult to obtain analytically.

Figure 2.11 shows the linearised acoustic amplitudes of combined GA and HRPWM waveforms. The 3rd harmonic amplitude is also shown, although, for greater clarity, values more than 15 dB below the fundamental are excluded. Similarly, figure 2.12 shows the same for $f = 3.3$ MHz, but subharmonics at 1.1 and 2.2 MHz are instead considered, because this is where the transducer can produce acoustic energy. The grey lines in both figures show the curve used for the fitting procedure described in the method.

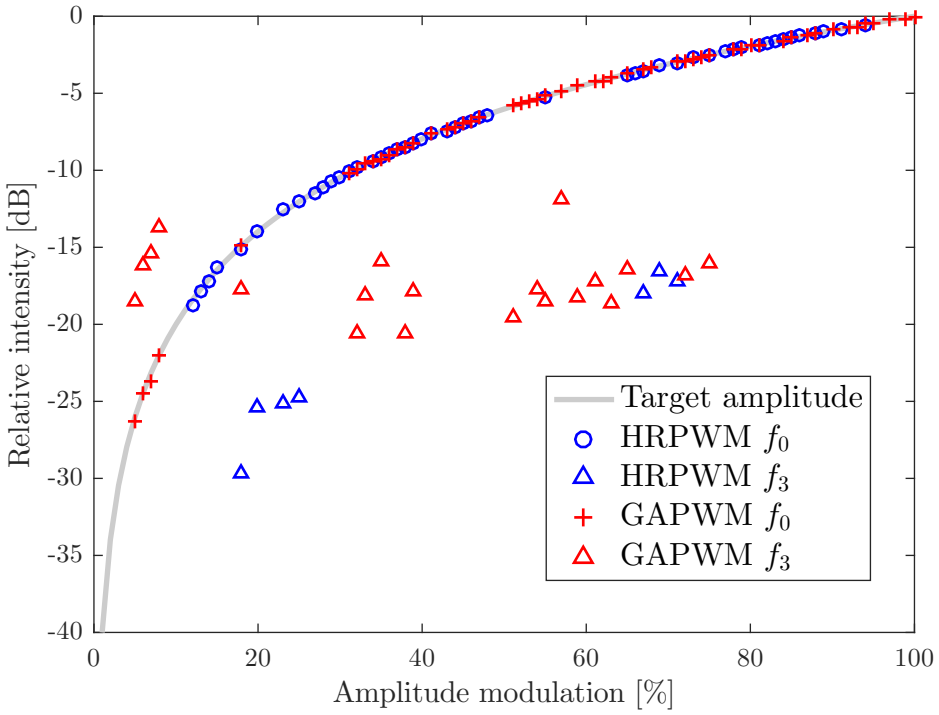

Figure 2.11: Experimentally obtained acoustic intensity for each design method across valid excitation amplitudes. Significant harmonic content is also shown. $f = 1.1$ MHz

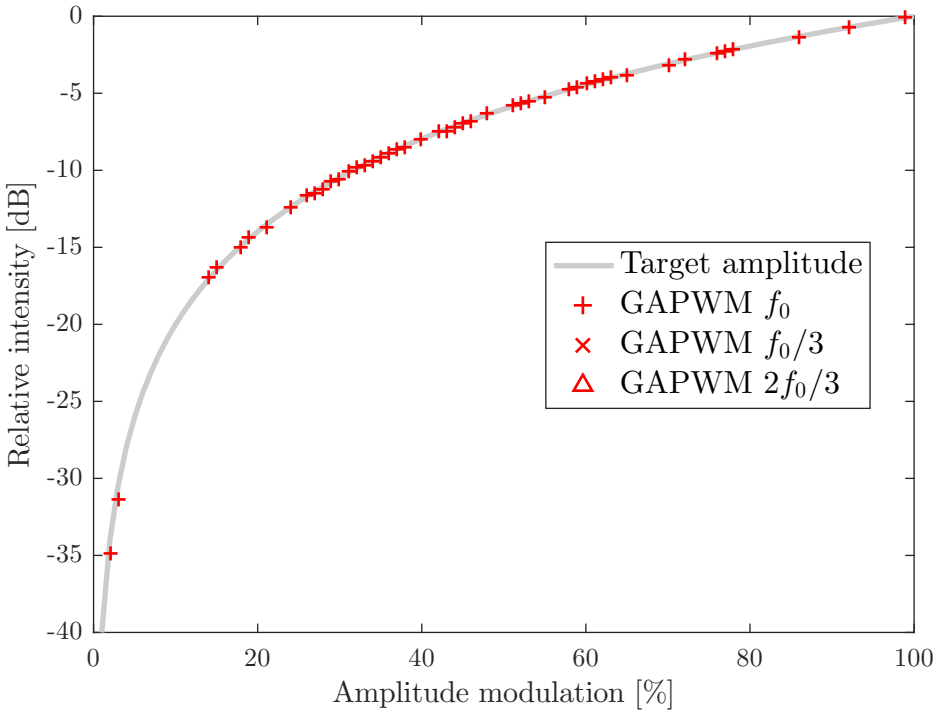

Figure 2.12: Experimentally obtained acoustic intensity across valid excitation amplitudes using GAPWM. There was no significant harmonic distortion in the acoustic output. $f = 3.3$ MHz

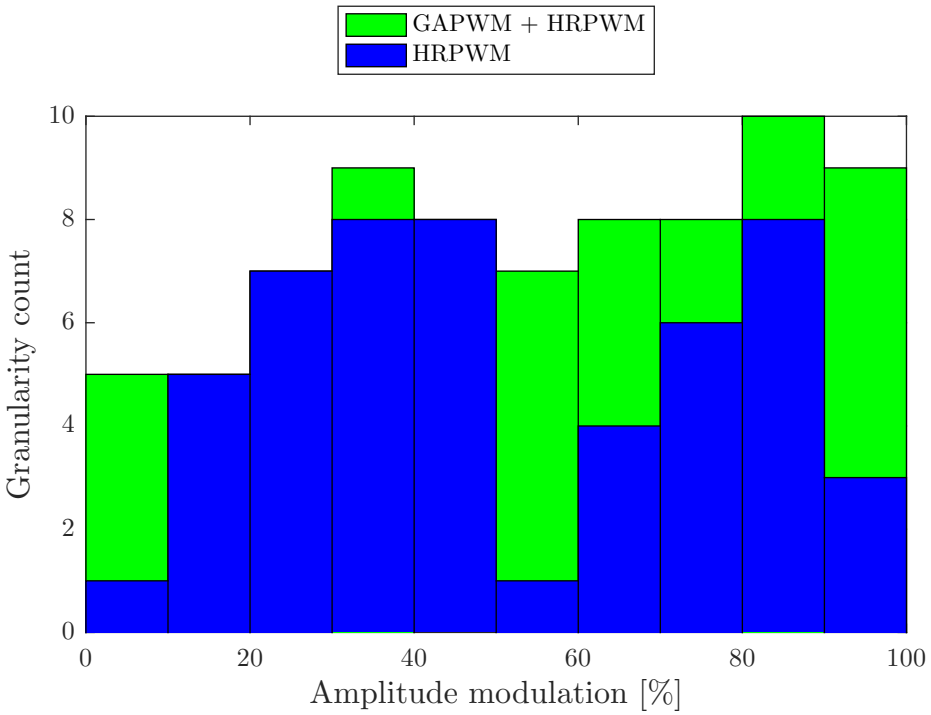

Figure 2.13: The number of valid excitations across the amplitude range. Green shows the granularity when HRPWM (blue) is supplemented with waveforms from GAPWM (green).

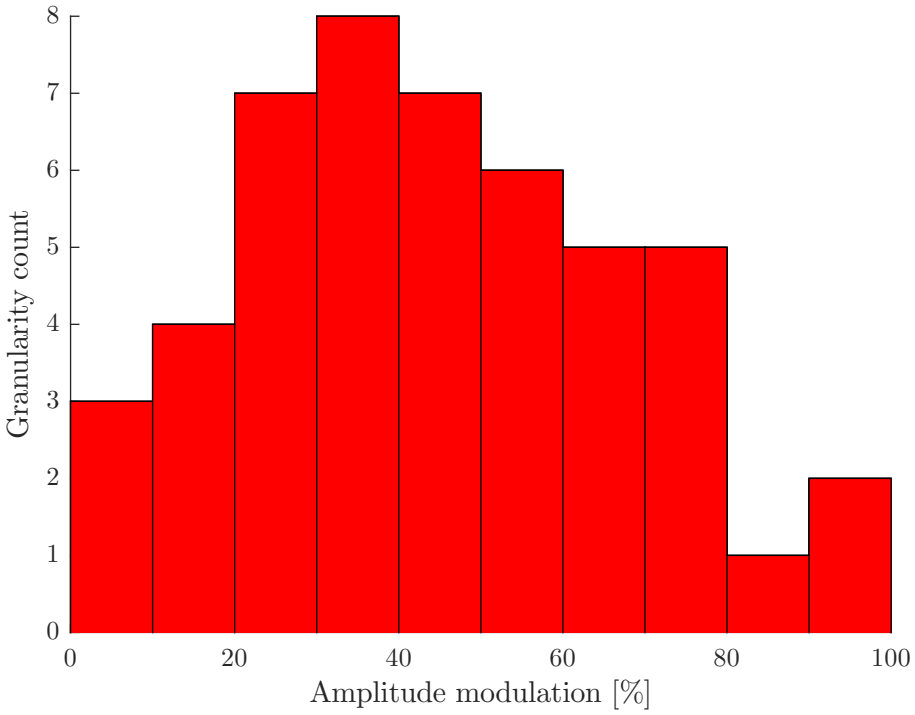

Figure 2.14: The number of valid excitations across the amplitude range. Red shows results from GAPWM when $f = 3.3$ MHz. HRPWM produced no valid excitations at this frequency.

To assess the effectiveness of the amplitude control with each scheme, the granularity of both was measured. The linear fit procedure already given in section 2.4.2 described how the effective acoustic amplitude was used to convert each excitation into a percentage. Following this procedure, the number of waveforms inside 10% intervals were measured. The granularity number indicates how many waveforms that differ by more than 0.1% (due to the threshold used in the fit procedure) in the given range there were. A high granularity number indicates that the scheme was able to achieve fine amplitude control in that range which is desirable. Granularity may also be given in percentage for the whole range. This indicates how many different amplitudes can be generated across the whole range. For example a 2% granularity indicated that totally there were 50 waveforms of different acoustic amplitudes.

The granularity of these results are shown in figures 2.13 and 2.14 for 1.1 and 3.3 MHz respectively. Due to the interval chosen in the linearisation procedure, 10 is the maximum possible value. The granularity when HRPWM and GAPWM results are combined is shown by the green bar of figure 2.13. The granularity achieved by GAPWM at 3.3 MHz is shown by the red bars in figure 2.14.

Figure 2.15 shows waveform solutions at 65% amplitude using HRPWM and GA. The green markers show where dead time is applied. The required dead time invalidates the waveform produced by HRPWM because of the collisions shown by the red patches. To avoid this, GAPWM produced a solution with a longer mid-level but no upper level.

Figure 2.16 shows a pressure wave measured at the transducer focus using GAPWM excitation. The amplitude was 65% and the frequency was 3.3 MHz.

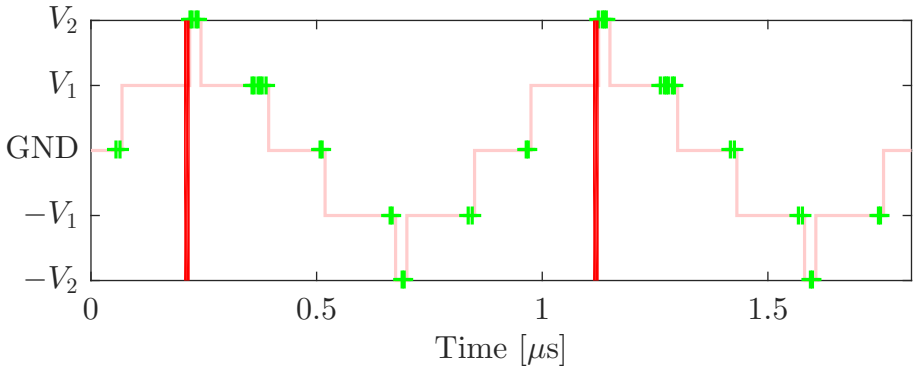

(a) HRPWM

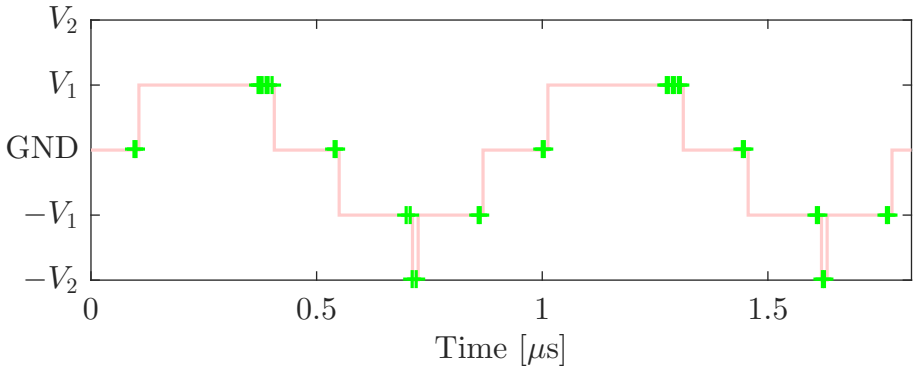

(b) GAPWM

Figure 2.15: Two switched waveforms generated using HRPWM (top) and GAPWM (bottom). The amplitude was 63%. The HRPWM waveform was unusable because of dead time collisions which are shown in red. The green crosses show the dead time.

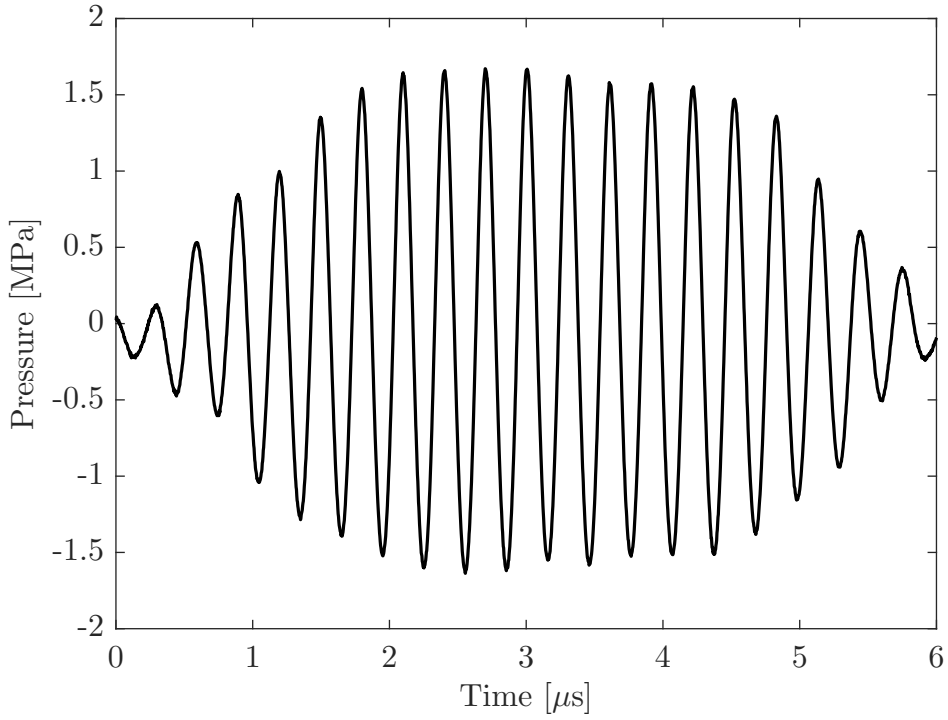

Figure 2.16: Recorded pressure wave when using a 3.3 MHz GAPWM excitation at 65%

2.5 Discussion

The results show that GAPWM is able to produce switched waveforms that can meet varying specifications for frequency response and strict timing. At 1.1 MHz, the GA was used to supplement HRPWM, improving on the granularity whilst maintaining 3rd harmonic reduction. At this frequency, between 60% and 80%, the granularity was reduced from 2.73% to 1.3%. However, at modulations below 20%, the harmonic reduction was ineffective and the waveforms would be unusable because the harmonics were so large. This is because of a limitation on the search space. In this modulation range, HRPWM achieves harmonic reduction through double pulses per half cycle which were not considered. The algorithm could be modified to consider such solutions.

At 3.3 MHz, the timing constraints imposed by dead time meant that HRPWM could not produce any usable waveforms. The GAPWM was re-run with the 3rd harmonic reduction requirement relaxed, but suppression of subharmonics (1.1 MHz) was enabled. The GA produced a set of waveforms with an average amplitude granularity of 2.1%. The pressure wave was clean of transients and any obvious distortion, although a slight reduction in peak pressure was observed with each cycle. This is perhaps due to the slight asymmetry of the voltage rails caused by differing P and N-type switch resistances. The algorithm could be modified to remove very low-frequency components if required. The improvements in granularity will allow the system to better apodise an array.

The produced waveforms may be difficult to derive analytically. However, the very nature of genetic algorithms means that the waveform solutions are likely to be close to but not equal to the global optima. This is evidenced for example by the increased harmonic content compared to the mathematically perfect solutions offered by HRPWM at equivalent amplitudes. The algorithm could be improved by performing a linear search once the space has been narrowed by the GA.

However, the GA's strengths lay in its flexibility, because the fitness function can be easily adapted to consider other requirements and solutions can be found relatively quickly. For 3.3 MHz, 100 waveforms were generated in 15 minutes with a regular desktop computer (Intel i5, 8GB Memory). By compar-

ison it would take approximately 1675 years to perform an exhaustive search of all possible amplitudes. This estimation allows 90 ms per test and 48^7 possible tests. There are some limitations, as the waveforms generated have fixed transmission frequency and amplitude. In therapeutic environments, this is ideal. However, for imaging applications, frequency modulated and windowed waveform are beneficial [17]. The unusual nature of the solutions pose some small problems, whilst they are successful novel solutions to the problem, there is currently no analytical understanding of the solutions, which may make frequency and amplitude modulated waveforms difficult to construct from the existing data.

If the algorithm could be adapted to consider solutions in terms of phase relationships, more complex waveforms could be constructed by comparing against the real phase of a chirp or other signal.

2.5.1 Adaptations for Ultra High Frequency Waveform Design

The trend in both biomedical imaging and NDT is to use continually higher frequencies [57]. The reduction in wavelength improves the spatial resolution which can reveal great detail even though in tissue, penetration depths are very low. At these frequencies, detailed imaging of the eye has been demonstrated [58].

The dead time requirement for the HIFUARP was just one example of a constraint that may be placed on waveform design, but high-frequency ultrasound ($>$ 20 MHz) and pre-clinical imaging (40-80 MHz) also present challenges for switched, discrete-sampled transmit systems. Adaptations to the algorithm for designing high-frequency waveforms are described in this section. Improving the granularity of HRPWM was again the aim. Apodisation is commonly used in imaging systems to reduce the magnitude of side lobes which cause imaging artefacts. To achieve this, the search space was increased so that more unusual waveform patterns could be generated with intentionally high harmonic distortion within the transducer bandwidth.

Whilst genetic algorithms are efficient at solving large search spaces, increasing the number of dimensions usually warrants an increase in the popu-

lation size to maintain diversity. A good rule of thumb is that the population size should be 10 times larger than the number of dimensions. Since the computational complexity is $O(n)$, the search space should be increased whilst minimising the number of additional dimensions, n. Fortunately, the problem can be constrained. Since it is still only possible to perform a few transitions per cycle, the entropy can be increased by instead changing the levels to which each transition goes.

Given the number of transitions is still fixed, the number of level permutations is also fixed. This allows a plethora of different waveforms to be produced with fixed angles by just changing one variable. Figure 2.17 demonstrates this for a 30 MHz waveform. Here the angle variables remain the same, but the permutation number (m) differs. Each waveform, in turn, has a unique representation in the frequency domain.

Improvements to the testing of fitness were also made. For the CW excitations, a number of repeat cycles were considered to ensure the average energy was the same or very similar as a sinusoid. For imaging applications, much shorter excitations are typically used, so in order to achieve reliability and good frequency resolution for fitness testing, the following changes were made. Firstly, each waveform was up-sampled to 300 MHz whilst maintaining the exact switching position. The fitness function was then applied on only one cycle, but over 50 repeats, with each repeat having a 2π offset. The error was summed over each repeat. This process allows high accuracy in the frequency domain over a short period of time with good reliability to extend the waveform into multiple cycles. This step stops the algorithm taking advantage of any harmonic properties afforded by sampling frequency rounding errors.

Figure 2.18 shows three example 30 MHz waveforms solved using the GA. Figure 2.19 shows 256 element apodisation profiles generated using ideal results, GA and HRPWM. The profiles were generated from 5 cycle excitations using each method, applying a representative bandpass filter, normalising and compensating for phase. The peak magnitude for all excitations was then found and fit, using the smallest error, to an ideal hamming window. Figure 2.19 below shows the error between the ideal and each of the switched methods. The HRPWM has a peak error of 100% at the edges of the window whilst GAPWM only has a peak error of approximately 55% at the same location.

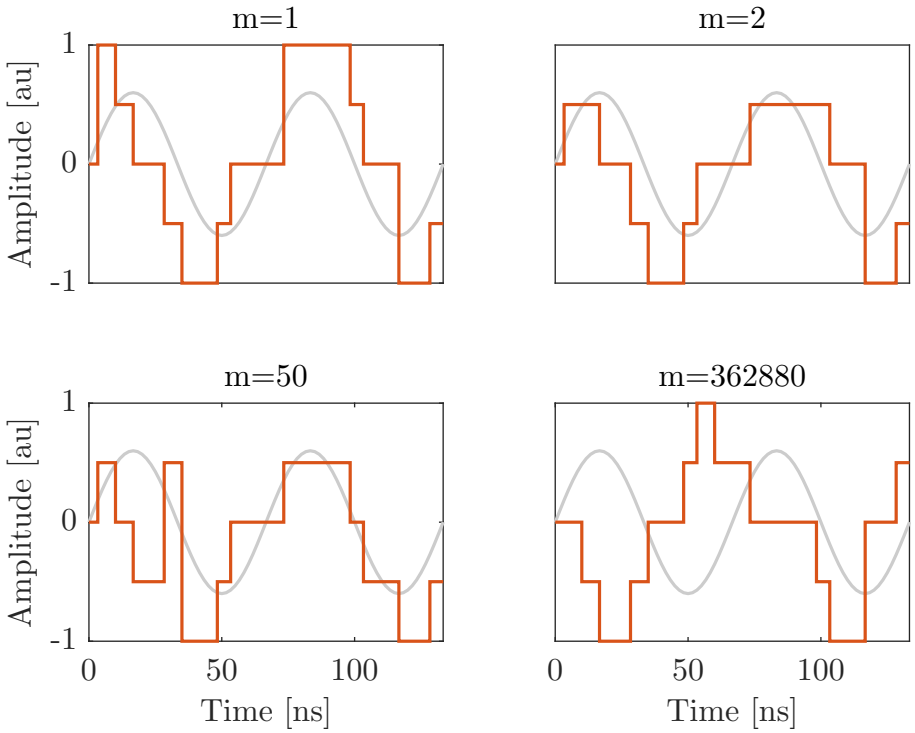

Figure 2.17: Several different waveforms produced using fixed angle parameters but with a different permutation number m. The addition of the m variable allows the entropy of the algorithm to be increased by including only one additional dimension to the search space.

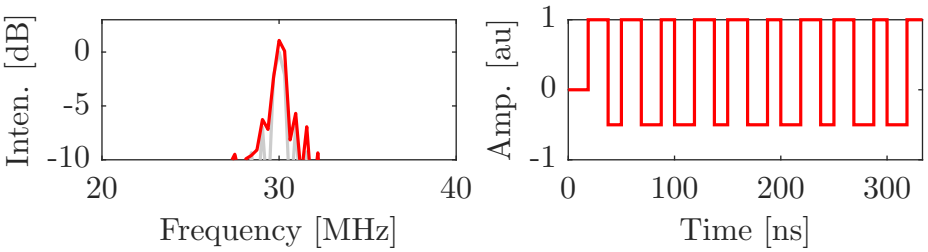

(a) 72 %

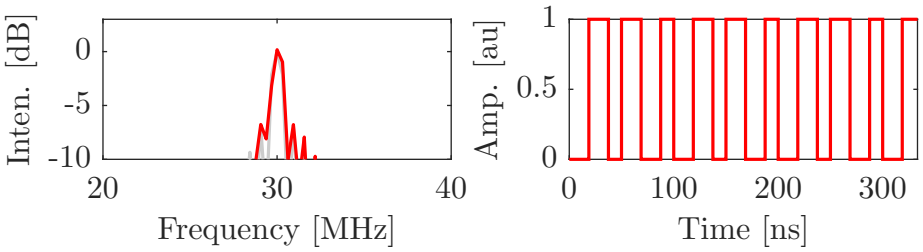

(b) 60 %

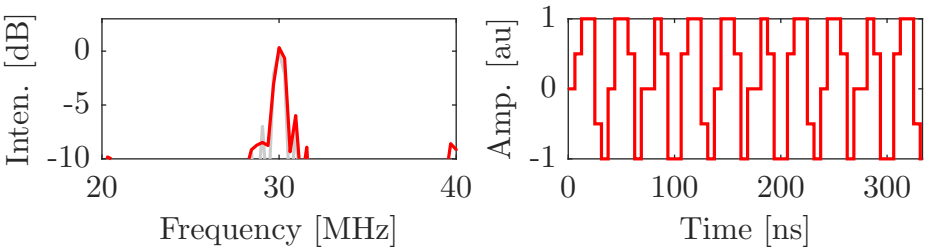

(c) 91 %

Figure 2.18: Three high frequency waveforms generated using the GA with amplitudes of 72 % (top), 60 % (middle), 91 % (bottom).

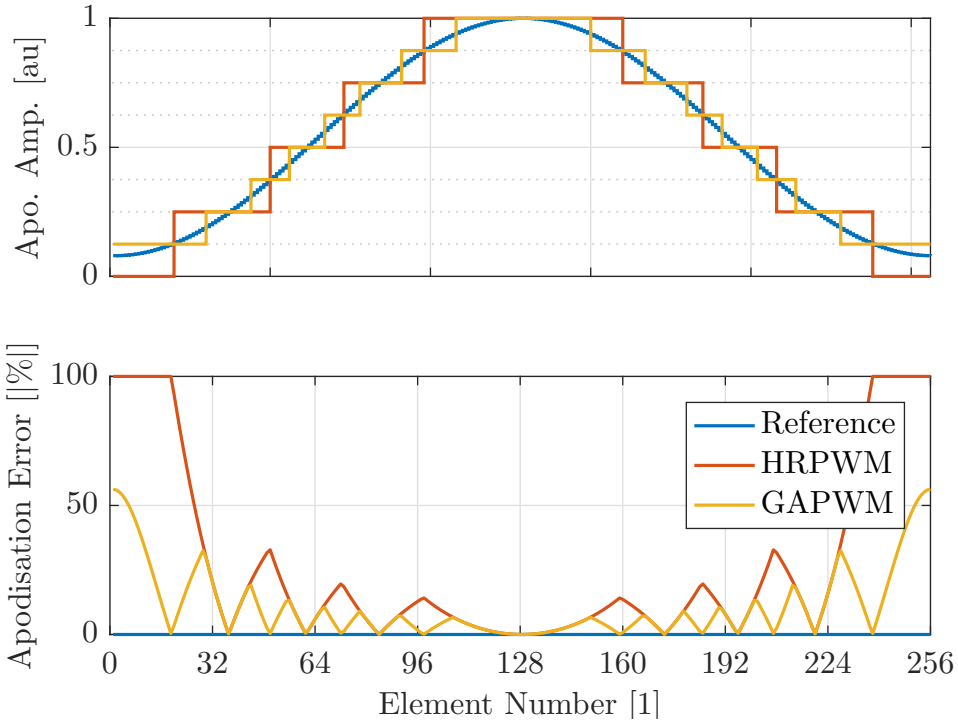

Figure 2.19: Top: Actual apodisation profiles achieved. Bottom: Absolute percentage error between target and achieved curve as a result of improved granularity.

This further highlights the rigidity of traditional switched waveform design methodologies. Although some improvements in efficiency may be provided, at high frequencies HRPWM's harmonic reduction is superfluous to requirements. For example, with a centre frequency of 20 MHz, the 3rd harmonic is 60 MHz; so in order for this to be observed acoustically, the transducer would need a 200% bandwidth. This is well beyond the capabilities of any current transducer technology.

2.6 Conclusions

Switched excitation offers many improvements in terms of efficiency and physical size. Without filtering, it can produce harmonics that may be observed acoustically if the transducer bandwidth allows. For ultrasonic waves that propagate with a strong dependence on frequency this switching distortion may have a profound influence on the expected behaviour.

To compensate, several authors have demonstrated switching schemes that minimise the production of the third harmonic. In practice, at low frequencies and with HIFU transducers it is more important to perform this reduction but is not necessary at high frequencies as the bandwidth of these transducers seldom allows production of the third harmonic. Timing constraints are also placed on the waveform, which makes some of these reduction techniques untenable. Accordingly, genetic algorithms were used to explore the large space and generate waveforms that improved on the granularity offered by existing schemes.

GAPWM can facilitate the use of switched excitation in ultrasonic systems where fine amplitude control is required, leading to lower cost per acoustic channel.

Chapter 3

An Adaptive Array Excitation Scheme for the Unidirectional Enhancement of Guided Waves

Control over the direction of wave propagation allows an engineer to spatially locate defects. When imaging with longitudinal waves, time delays can be applied to each element of a phased array transducer to steer a beam. Because of the highly dispersive nature of guided waves, this beamsteering approach is sub-optimal. More appropriate time delays can be chosen to direct a guided wave if the dispersion relation of the material is known. Existing techniques, however, need a priori knowledge of material thickness and acoustic velocity. The scheme presented here does not require prior knowledge of the dispersion relation or properties of the specimen to direct a guided wave. Initially, a guided wave is generated using a single element of an array transducer. The acquired waveforms from the remaining elements are then processed and retransmitted, constructively interfering with the wave as it travels across the spatial influence of the transducer. The scheme intrinsically compensates for the dispersion of the waves and thus can adapt to changes in material thickness and acoustic velocity. The proposed technique is demonstrated in simulation and experimentally. Dispersion curves from either side of the array were acquired to demonstrate the scheme's ability to direct a guided wave in an aluminium plate. Results show that uni-directional enhancement is possible

without a priori knowledge of the specimen using an arbitrary pitch array transducer. Experimental results show a 34 dB enhancement in one direction compared with the other.

3.1 Introduction

Guided waves (GW) have been applied to a plethora of inspection problems [14], [59]. The applications are abundant and diverse. Historically GW have been used for the inspection of pipe work [60], [61], heat exchangers and aging aircraft [14]. Newer aircraft are manufactured from composites, which require sophisticated techniques for inspection [62], [63]. Guided waves however are still applicable here [64], [65]. They are widely regarded as the most promising tool for non destructive evaluation (NDE) [66], [67] and structural health monitoring (SHM) [68]–[74]. GW also have biomedical applications [75]–[80]. Their excellent range [66]–[68], good sensitivity [74] and flexibility of application [60], [68], [69] make them desirable in NDE and SHM.

In pipes and plates, guided waves are used for detection of cracks [61], [72], delaminations [65] and corrosion. Welds [67] and joints [14], [72], [81] can be evaluated and thickness can be measured [82]. With the correct choice of mode, which will be discussed later, guided waves can propagate in pipes that are immersed or coated [14].

Lamb waves, a useful variety of guided waves, are complex [14], but they are now well understood [83]–[85]. They are composed of multiple modes of oscillation [86] which is advantageous for the detection of many types of defects [60]. Low order modes can be used for the detection of large cracks, and higher order modes can be used for the measurement of corrosion [60], [87], [88], texture and small defects [87].

Two dimensional Fourier analysis [71], [89] and delay-sum methods [83] can quantify the presence of modes [67]. This technique is commonly used to quantify the interaction of Lamb waves with defects [90]. Phase velocity dispersion relations are often more useful but are harder to obtain experimentally, although authors have obtained them using optoacoustics [91]. For low frequency-thickness products this is not problematic, as only two modes exist

[66], [67], A_0 and S_0. Lamb waves are dispersive, however, so their velocity changes with frequency. At higher frequency-thickness products, low order modes will approach Rayleigh waves, whilst higher order modes can have the same velocity. In SHM situations, where a broadband stimulus is commonplace, sophisticated methods for the separation of these higher order modes exist [65]. Thus for high order mode inspection, it can be desirable to only generate a single mode at a time [67], [87]. Monitoring the backscatter [61] for reflections can indicate poor bonding, whilst mode conversions [65] can be observed when a mode interacts with the edges of a defect [71], [92]. Control over mode generation can also be useful for traversing complex materials or waveguides [93]. Mode selection, however, is not required for more common low order mode inspection, as these modes can be easily identified.

Control over the direction of propagation is advantageous to the engineer for greater range and location of defects [68], [74], [94]. With finite acoustic power, a greater range can be realised by applying the wave in only one direction. Without any steering, Lamb waves will propagate in all directions equally in the waveguide. When the Lamb wave interacts with a defect it can be difficult to locate since the reflection or mode conversion could have come from any direction. Scatter and the inherent dispersion of Lamb waves can hamper exact location of defects, but methods exist to compensate for this [59], [73], [95]–[97]. The application of signal processing in NDE is commonplace [98].

While sophisticated techniques for guided-wave inspection exist, they are not always adopted. Often not all the necessary parameters are known at the time of inspection. This is especially an issue when the specimen is placed in a harsh environment. Pipes can be under strain or be heated by their contents. In SHM, components may be exposed to extreme seasonal temperatures [99]. All these will effect the acoustic properties and dispersion relation of the material. Existing techniques are not robust to these harsh environments which may contribute to their lack of adoption. Progress is being made in the development of software to automate processes and analysis [100]. A parameter-agnostic technique for the generation of directed guided waves might allow guided waves to see more use in the field.

In thin plates, transmission at an oblique incidence has historically been used for control over direction, mode generation and mode reception. Many

researchers point out its limited use [68]. The engineer is limited by the angular resolution of the probe, and changing the angle can be tedious or impossible if the transducer is buried or inaccessible.

Arrays are increasingly used in NDE [35] in place of single element transducers. Arrays can be used to excite a single mode if the pitch matches the wavelength of the desired mode. Generally, arrays are favoured in ultrasound because of their flexible beamforming capabilities. Whilst beamforming of transducer arrays is often associated with medical imaging [101], these techniques are applicable to NDE also [102]. New NDE specific imaging techniques are being published too [103]. A commonly used industrial technique for creating a unidirectional array is to apply a 90° phase shift to quarter wavelength separated elements[1]. With respect to GW specific techniques, unidirectional single-mode waves can be generated through the application of delays to each element's excitation in a phased array transducer[2]. The delays approximate the transport time of the phase for the desired mode between adjacent elements. In both cases, this is only possible with a priori knowledge of the specimen thickness and its dispersion curves. When the modes of the specimen are unknown it may be possible to first obtain a dispersion curve from an edge reflector and use these results as inputs into the technique just described. However, the availability of an appropriate reflector cannot be guaranteed and it complicates an already complex inspection technique with an additional step. In SHM, authors have manufactured bonded transducers that are able to direct guided waves based on the wavenumber [74].

This chapter describes a scheme for the uni-directional enhancement of guided Lamb waves. The direction of propagation can be controlled without a priori knowledge of the material's parameters. This chapter builds on existing work[3] with the addition of an improved signal processing chain that has

[1] C. F. Vasile, 'Periodic magnet unidirectional transducer', 4 232 557, Nov. 1980.

[2] J. Li and J. L. Rose, 'Implementing guided wave mode control by use of a phased transducer array', *IEEE transactions on ultrasonics, ferroelectrics, and frequency control*, vol. 48, no. 3, pp. 761–768, 2001.

[3] C. Adams, S. Harput, D. Cowell *et al.*, 'Specimen-agnostic guided wave inspection using recursive feedback', in *IEEE International Ultrasonics Symposium (IUS)*, IEEE, 2016, D. M. Charutz, E. Mor, S. Harput *et al.*, 'Guided wave enhancement phased array beamforming scheme using recursive feedback', in *2013 IEEE International Ultrasonics Symposium (IUS)*, Jul. 2013, pp. 166–169. DOI: 10.1109/ULTSYM.2013.0043.

facilitated experimental validation.

3.2 Method

In this section, a scheme for the uni-directional enhancement of guided waves is described. A short process called recursive feedback allows the scheme to resolve unknown parameters. Consisting of several short iterations, once complete, allows uni-directional guided wave inspection to be undertaken. Simulation results are presented for the purpose of graphical demonstration. Following this, mathematical analysis is undertaken by comparing the scheme with an existing one. Before experimental validation can be completed a noise filtering and truncation signal processing chain is presented. Finally, experimental process and parameters are justified.

3.2.1 Recursive Feedback

Consider a phased array transducer of N elements mounted normally on a thin plate as shown in figure 3.1.

The recursive feedback scheme is as follows:

1. $i = 1$ Initially, the first element of the transducer is excited with a linear chirp. As the first element loads the material, longitudinal and shear waves combine and create multimodal Lamb waves that travel in both directions. Simultaneously element two records the surface pressure of the material.

2. $i = 2$ Now the first element transmits the same stimulus as it did before. This time, however, the second element transmits back its recording from the previous iteration. The third element records.

3. $i = 3$ In the third step of the scheme, the first element transmits its stimulus, the second its recording from step one and the third its recording from step two. The fourth element records.

4. $i = N$ This process is continued until all N elements are transmitting.

The effect is that Lamb waves tend to travel in the direction of the array's spatial influence ($+Z$). Each element reinforces the travelling wave using its recording. Lamb waves will still propagate in the opposite direction but with less energy. The scheme will amplify forward ($+Z$) any modes generated by the first element.

It is often highly desirable to enhance only one mode at a time which facilitates thorough inspection, where each mode is sensitive to different defects. However, the multimodal nature of the scheme is advantageous in two circumstances. The first is at low frequency-thickness products where the modes are easily separated by their disparate phase velocities. At this operating point, mode selection is less advantageous as modes can be very easily separated temporally. The second circumstance is the inspection of joints because the lowest order modes are most indicative of joint health. For example, complete attenuation of all modes crossing the boundary indicates a break whilst a loss of the A_0 mode indicates contamination in a kissing bond joint.

The process is shown diagrammatically along side finite element modelling (FEM) results in figures 3.1a through 3.1f. In FEM a 2.5 mm thick aluminium sheet was used. The excitation was a 10 cycle 700-800 kHz linear chirp. Idealised pressure loads were used instead of a transducer to improve simulation efficiency and they were separated (pitch) by 400 μm. The linear chirp was windowed with the Blakman-Harris function. The colour represents pressure. In figure 3.1a element 1 is transmitting (green) whilst element 2 is recording (red). The wave packets are equal in pressure and equidistant from the first element. In figure 3.1b elements 1 and 2 are transmitting, element 3 is recording. In $+Z$, the wave packets appear less defined than those in $-Z$. In figure 3.1c, elements 1, 2 and 3 are transmitting. Element four is recording. This process is continued until the ninth and final iteration, shown in figure 3.1f. Here the wave packets are most intense and well defined in $+Z$.

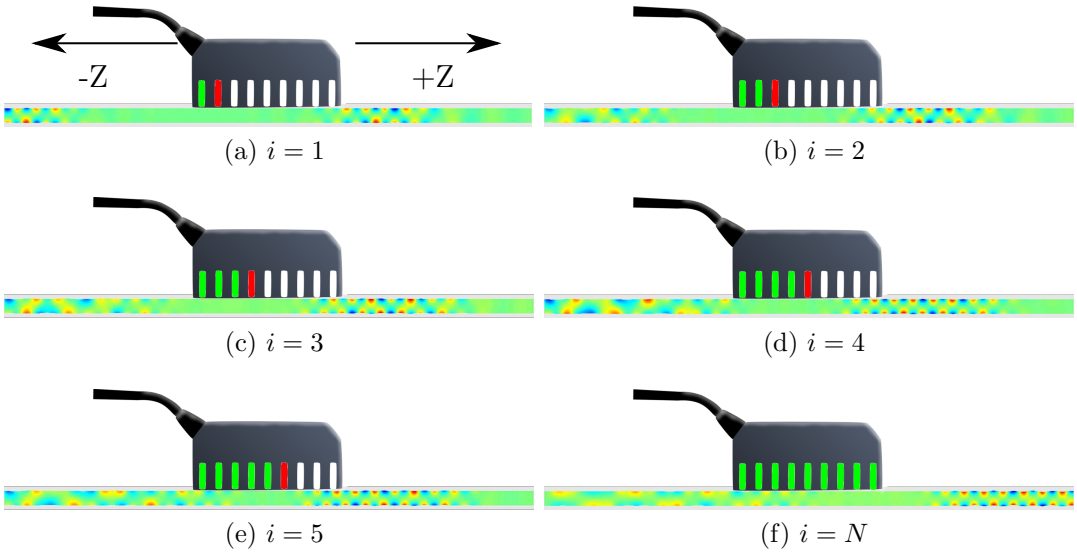

(a) $i = 1$ (b) $i = 2$

(c) $i = 3$ (d) $i = 4$

(e) $i = 5$ (f) $i = N$

Figure 3.1: Diagrammatic representation of each iteration of the scheme. A nine element array transducer is superimposed on simulation results to show where pressure loads were applied. The colour of the waveguide represents the normalised intensity of the pressure. Elements which are highlighted green are transmitting, whilst those highlighted red are receiving. Simulation images for iterations 1 though 5 are captured at 17 μs. For the Nth iteration the image was captured at 23 μs, enough time for the wave packets to exit the influence of the array. The scheme enhances guided waves in one direction.

3.2.2 Background

The wave-length of a Lamb wave is described by equation 3.1. The phase velocity, C_{ph}, can be found from well documented dispersion curves. An array transducer of pitch L can be used to amplify a particular mode. If $\lambda = L$, an excitation with a centre frequency of f can be used to satisfy equation 3.1, the corresponding mode will be amplified in both directions. This is limited of course by the pitch and bandwidth of the transducer.

$$\lambda = \frac{C_{\text{ph}}}{f} \tag{3.1}$$

The rest of this section references work already published on the use of time delays for mode selectivity in both directions[1].

[1]W. Zhu and J. L. Rose, 'Lamb wave generation and reception with time-delay periodic

For an array probe mounted to a thin waveguide, the amplitude of a generated mode is described by equation 3.2.

$$A_{\mathrm{m}}(z) = V \cdot F(\omega) \cdot C_{\mathrm{m}}(z) \cdot H(\omega) \tag{3.2}$$

Where $\mathrm{A_m}(z)$ is the amplitude of mode m. V is particle displacement. $F(\omega)$ is the frequency response of each element and $C_{\mathrm{m}}(z)$ is the coupling coefficient between the waveguide surface traction and the guided wave mode. z is the position along the waveguide. Since the designer has no control over the coupling coefficient or the frequency response of each element, $H(\omega)$ must be changed to affect the amplitude of a mode. Equation 3.3 describes the transducer response in relation to frequency and separation when using a single frequency.

$$H(\omega) = \sum_{i=1}^{N} e^{j[\omega t \mp \beta_{\mathrm{m}}(z-z_i)]} = \frac{\sin(N\frac{L}{\lambda}\pi)}{\sin(\frac{L}{\lambda}\pi)} e^{j[\omega t \mp \beta_{\mathrm{m}}(z-z_{\mathrm{centre}})]} \tag{3.3}$$

$\mp$ means $-$ for $+Z$ and $+$ for $-Z$. λ is the wavelength of harmonic mode m. z_{centre} is the centre location of the transducer array. β_m is the wavenumber. To influence $H(\omega)$ either the frequency must be changed or the separation must be changed. For the designer, this is either tedious or impossible. With the introduction of an additional delay of t_{d0} to each element i, $H(\omega)$ can be influenced without changing these parameters. Consider equation 3.4.

$$H(\omega) = \sum_{i=1}^{N} e^{j[\omega(t-t_i) \mp \beta_{\mathrm{m}}(z-z_i)]} = \frac{\sin[N\pi(\frac{L}{\lambda} \mp \frac{t_{d0}}{T})]}{\sin[\pi(\frac{L}{\lambda} \mp \frac{t_{d0}}{T})]} e^{j[\omega(t-\frac{N-1}{2}t_{d0}) \mp \beta_{\mathrm{m}}(z-z_{\mathrm{centre}})]} \tag{3.4}$$

In order to maximise the amplitude of a harmonic mode in the $+Z$ direction, t_{d0} should be chosen to satisfy

$$\lambda = \frac{L}{(n - t_{d0}/T)} \tag{3.5}$$

linear arrays: A bem simulation and experimental study', *Ultrasonics, Ferroelectrics, and Frequency Control, IEEE Transactions on*, vol. 46, no. 3, pp. 654–664, 1999, J. Li and J. L. Rose, 'Implementing guided wave mode control by use of a phased transducer array', *IEEE transactions on ultrasonics, ferroelectrics, and frequency control*, vol. 48, no. 3, pp. 761–768, 2001.

T is simply $1/f$. n here is an arbitrary integer, of a value that must satisfy $n > (t_{d0}/T)$. Here, t_{d0} is used to approximate the propagation time between adjacent elements, such that the peaks of the travelling mode are reinforced. It does not however take into consideration the dispersive nature of Lamb waves; the travelling wave will tend to temporally spread, so only one mode at one operating point is enhanced. The scheme proposed here takes this into consideration, reinforcing the travelling wave as it appears at the transducer in the previous iteration. This is keystone to the proposed scheme's ability to enhance multiple modes simultaneously.

3.2.3 Signal Processing

The dispersive nature of Lamb waves means that successive excitation sequences grow in length. Additionally, any noise introduced by simulation artefacts or otherwise will be amplified until the experiment becomes unstable. There is a need then for signal processing to reduce the amplification of noise and to truncate the signal.

Firstly a bandpass filter was used to block any irrelevant frequencies, such as those that are outside the frequency range of the transducer and the initial excitation. The filter must have a linear phase, so an FIR design was employed. The filter order was 50, and the -6 dB bandwidth was the same as the transducer used.

Recordings were then cross correlated with the initial stimulus to find the point t_0. t_0 is the lead, τ applied to maximise the correlation of initial excitation, x and the recording, y:

$$t_0 = \arg\max \tau(x \star y)(\tau) \tag{3.6}$$

It is imperative that noise and cross-talk between adjacent elements is rejected. Restrictions were placed on τ:

$$2 \times t_k < \tau < \frac{i}{f_{\min}} \tag{3.7}$$

Here, t_k is the propagation delay in the PZT. The signal must have propag-

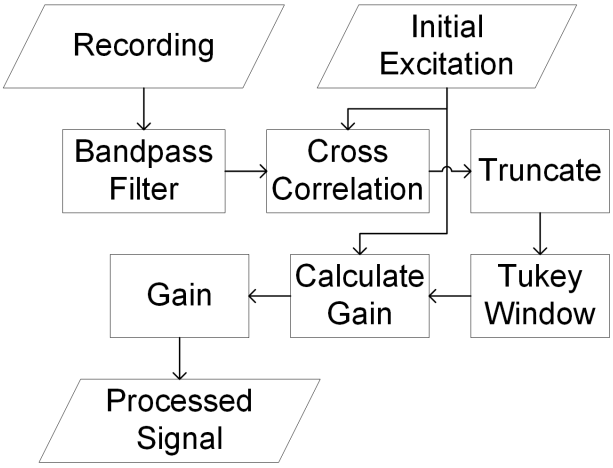

Figure 3.2: Signal processing chain used to reject noise and ensures that the region of interest is re-transmitted.

ated through the first element (t_k, known), through the material (unknown) and through the second element (t_k) before it can be considered a valid correlation. The value t_k can be obtained through a simple pulse echo experiment: With a material of known dimensions and speed of sound, the error between theoretical and actual time arrival will equate to $2t_k$.

$f_{\min}$ is the start frequency of the chirp, $x(t)$. The upper boundary ensures that the bottom term, $n - \frac{t_{d0}}{T}$, of equation 3.5, remains positive. $n = 1$ since $L < \lambda$.

All transmissions should be of length T_t, the length of x. Abrupt truncation of the signal could introduce high-frequency components, so windowing was applied so as to achieve a gradual reduction in amplitude as $t_0 \leftarrow t$ and $t \rightarrow (t_0 + T_t)$. A Tukey window was used here to maximise total energy in the transmission whilst maintaining a gradual reduction in amplitude near the edges.

Finally, a gain was applied to equate the peak value of x and y. The signal processing chain is shown in figure 3.2.

3.2.4 Quantifying Directivity

The 2D Fourier transform method was used to obtain a dispersion curve [5], [89]. This was accomplished by measuring the surface acoustic pressure at

many points in monotonic space. Recordings were then packed together into a matrix, with dimensions of space and time. Taking the two dimensional Fast Fourier Transform (FFT) gave a matrix of frequency against wavenumber. Since recording length and FFT size were conserved, the directivity of the scheme was quantified by comparing the outputs of the FFTs since energy was conserved. The peak value of the first iteration was used as a reference for power calculation.

Experimentally several techniques exist for evaluation of surface displacement; Laser vibrometers [97] and optical fibres [107] are popular choices. Here the transmitting array was used to obtain a dispersion curve for experimental simplicity. The transducer array was placed close to one edge and separated from the others by a much greater distance. Generated waves were reflected by the closest edge of the plate before passing over the array. It was important that the transducer was not moved between comparisons of $+Z$ and $-Z$. Re-positioning the transducer might have affected the coupling, and so the distance to the reflecting edge could not be reliably reproduced. To combat this, the enhancement direction of the scheme was changed whilst leaving the transducer in situ. The array was split in two. In the first experiment, $+Z$ was quantified by exciting toward the reflector from the middle element. In the second experiment, $-Z$ was quantified by enhancing away from the reflector using the other half of the array. For a 64 element array, element 32 transmitted during the first iteration regardless of the enhancement direction. For evaluation of $+Z$, elements 32 through 63 were energised. For evaluation of $-Z$, elements 32 through 1 were energised. Dispersion curves will be identical during the first iteration regardless of enhancement direction. This arrangement is shown in figure 3.3.

3.2.5 Experimental Parameters

Experimentally, a 64 element array probe with a pitch of 0.33 mm and centre frequency of 2.5 MHz was used. The waveguide was a 0.9 mm thick aluminium plate. A high viscosity and high impedance couplant was required to maximise energy transfer between the transducer and the waveguide, so a thin layer of honey was employed between the two. The transducer was placed 120 mm

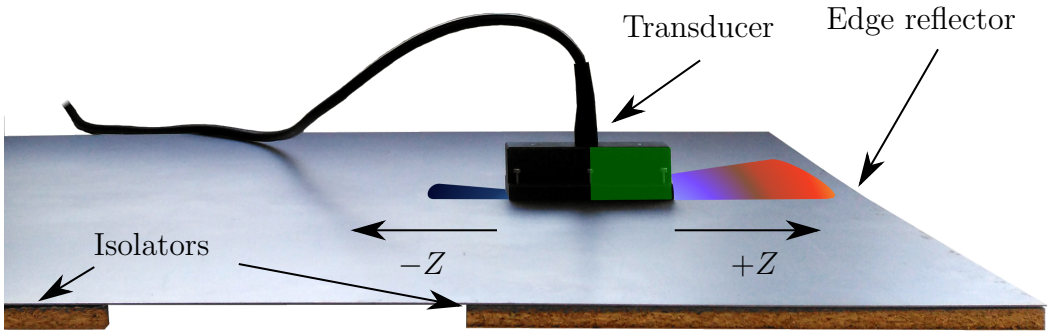

(a) Guided waves are enhanced toward the reflector. The right hand side of the array is excited.

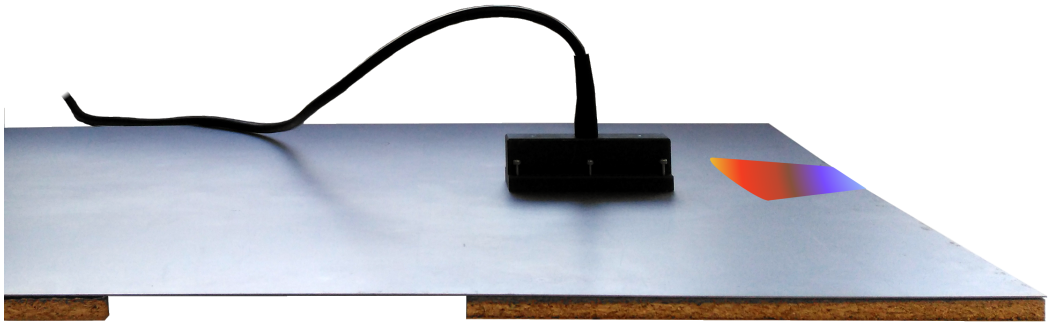

(b) Some time after, the wave packets reflect off the edge and pass over the array. The $+Z$ dispersion curve is acquired.

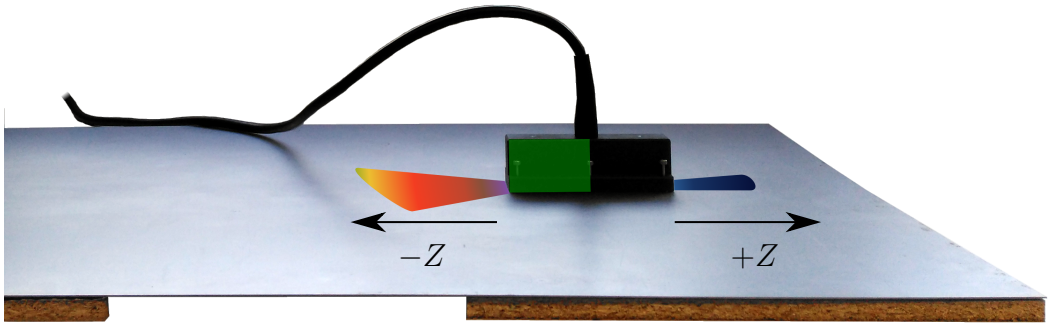

(c) The enhancement direction is changed allowing the $-Z$ dispersion curve to be obtained

Figure 3.3: Depiction of the experimental arrangement. An array transducer was mounted on a metal plate. The plate edge was used as a reflector so that the transmitting array could also be used to acquire a dispersion curve. The array was selectively excited to change the enhancement direction so that both directions can be measured. Between experiments, the array was not disturbed and the first transmitting element remained the same distance from the reflector. Small pieces of wood were placed along the perimeter of the non-reflecting edges to acoustically isolate the plate.

away from the reflecting edge and approximately 1 metre from the other edges. The initial stimulus was a 10 cycle 2.25-2.75 MHz linear chirp, windowed with the Blackman-Harris function.

The first time the experiment was run, the waveforms were unknown. The received, and subsequently re-transmitted waveforms are related to a large number of variables relating to the material and how it disperses. The keystone of this scheme is its ability to excite modes without knowledge of the material's properties. Since the returning waveforms could not possibly be predicted, arbitrary waveform generation was required. Experimentally this was achieved using the 5 level, HRPWM algorithm described in chapter 2.

3.3 Experimental Results and Observations

Figures 3.4, 3.5 and 3.6 show dispersion curves from iterations 1, 4 and 31 respectively. In each case, curves for each direction are presented. Theoretical results, which were calculated using GUIGUW [108], [109] are overlaid in white.

In the first iteration of the scheme, $+Z$ and $-Z$ are almost identical, which is to be expected. In the first iteration, modes A_0, S_0 and A_1 are visible. In the fourth iteration (figure 3.5), the scheme begins to exhibit its enhancing capabilities. In the $+Z$ enhancement direction there is more energy, indicated by dilation around the A_1 and S_0 modes. Figure 3.6 shows the last iteration of the scheme ($i = 31$). Here the enhancing capabilities of the scheme are most apparent. Compared with the first iteration, the most dominant mode in $+Z$, S_0, has increased by 35 dB. Modes A_0 and A_1 have increased by 30 dB. Conversely, in $-Z$, there is only a 10 dB increase in energy. There are vertical stripe artefacts visible in this curve that extend into all wave numbers at approximately 2.5 MHz. The artefacts have a pattern in the frequency domain, suggesting that all channels are affected equally and it is not a spatially-varying problem. Possible causes may be side lobes from the FFT, or ADC distortion. The directional enhancement was achieved without any knowledge of the material's dispersion curves, a requirement of other schemes.

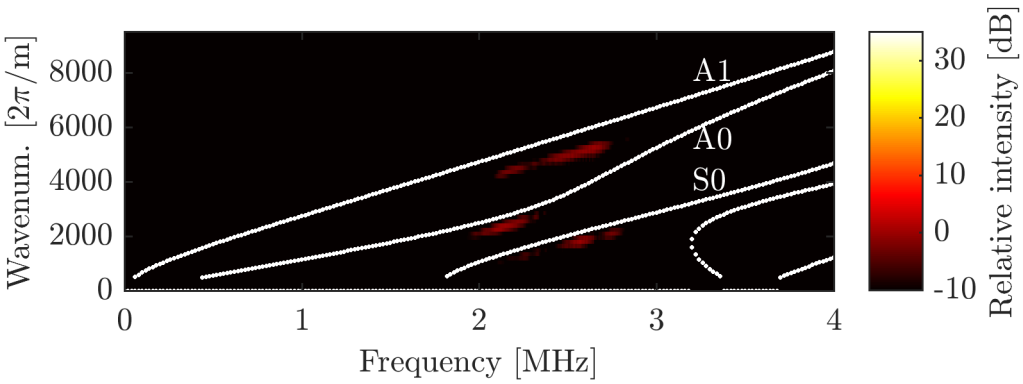

(a) $+Z$

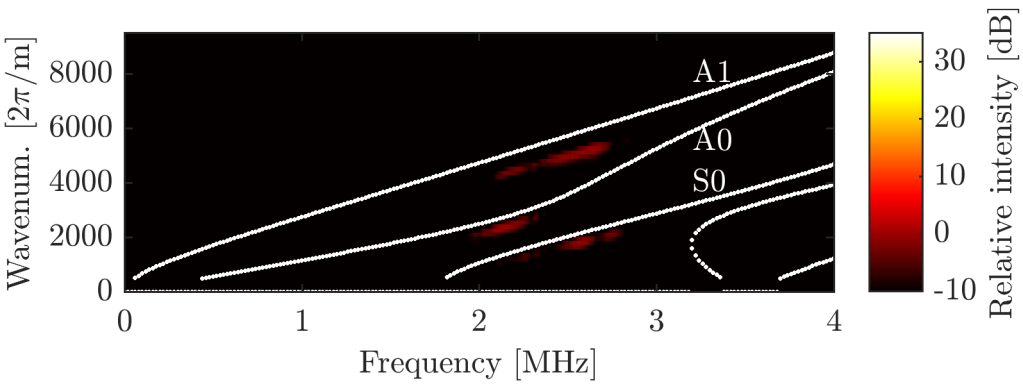

(b) $-Z$

Figure 3.4: Dispersion curves measured in $+Z$ and $-Z$ for the first iteration. The dispersion curves are equal, the guided waves show no preference for either direction.

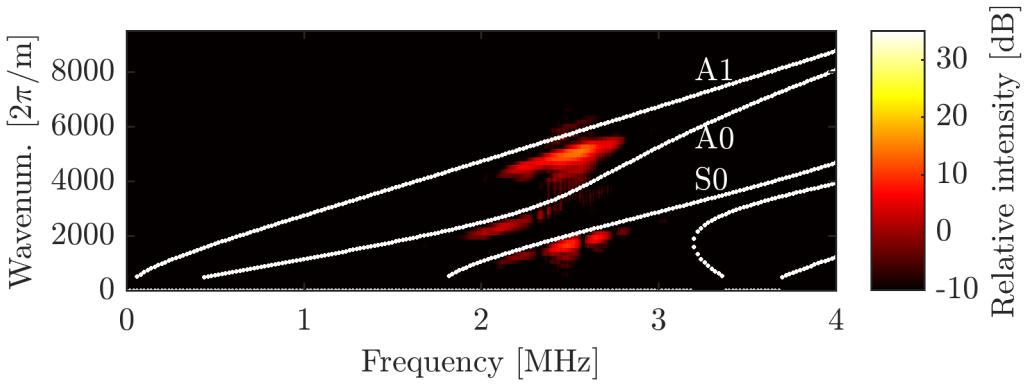

(a) $+Z$

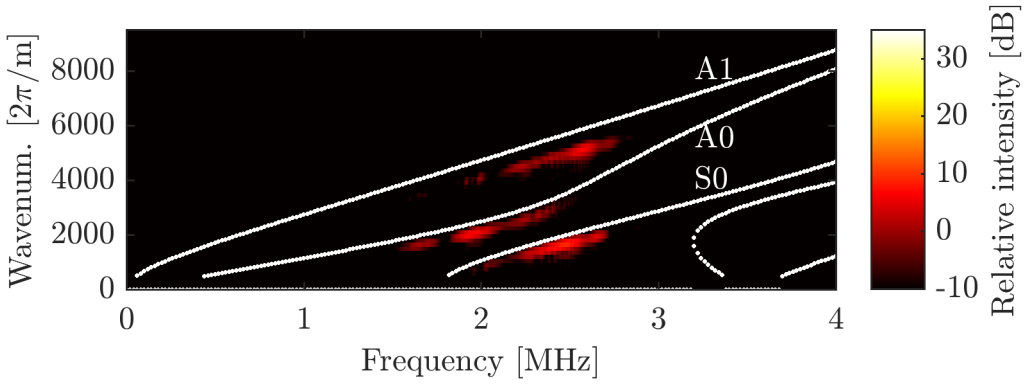

(b) $-Z$

Figure 3.5: Dispersion curves measured in $+Z$ and $-Z$ for the fourth iteration. The scheme begins to demonstrate its steering capability.

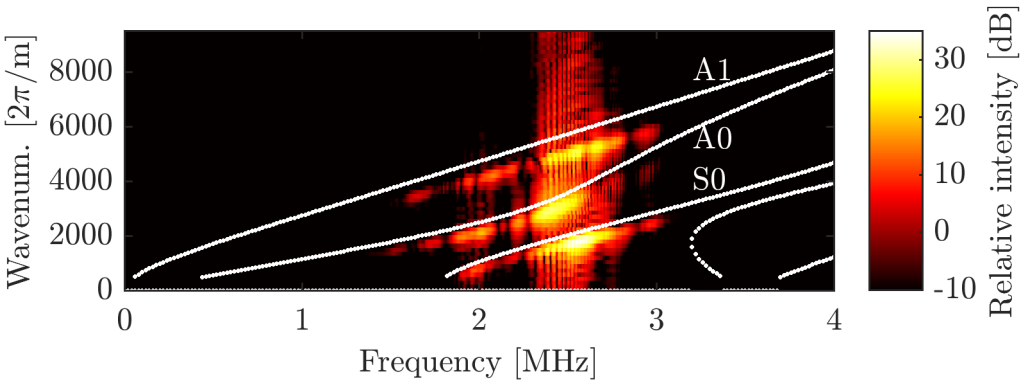

(a) $+Z$

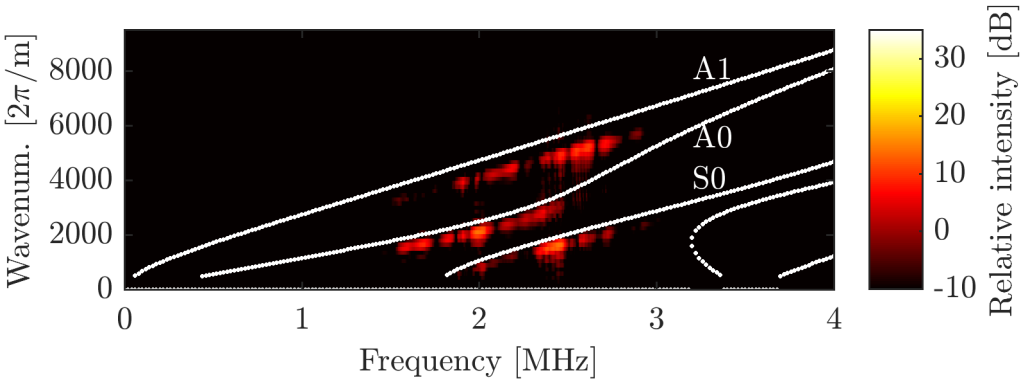

(b) $-Z$

Figure 3.6: Dispersion curves measured in $+Z$ and $-Z$ for iteration 31. In the final iteration, the scheme shows preference for $+Z$ as more energy is present

3.4 Simulated Inspection

In this section, the recursive feedback scheme will be applied to two inspection problems. The simulated transducer and excitation frequency will remain the same between problems, but different materials will be used. The first is chosen to highlight the scheme's ability to excite several modes without prior knowledge of the material's properties. In the second, defect localisation and detection will be carried out.

The transducer had 8 elements and the pitch was 3 mm. Each element was 400 μm wide and the excitation was a 700 - 800 kHz linear chirp.

3.4.1 Contaminated Lap Joint

Lap joints consist of two plates that are glued together with an overlap and are commonplace in aeronautics. Causes of failures include inclusions (contamination) and voids. These are caused by poor curing, poor surface preparation or stress [110]. A cross-section of a lap joint with an inclusion is shown in figure 3.7.

When poor quality lap joints are subjected to guided waves, mode conversions, phase velocity changes and attenuation occur when the waves interact with contaminants. For example, the amplitude of the S_0 mode can indicate the existence of a delamination [111]. However, the A_0 mode is most sensitive to bond state and exists often [112]. Fully cured bonds convey the most energy but inclusions may introduce fluid modes. As the guided waves cross the

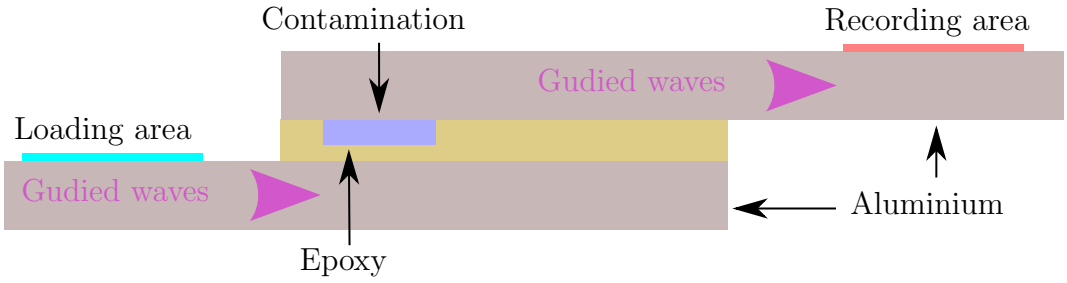

Figure 3.7: Diagram of the simulated lap joint that has been contaminated. Two plates are epoxied together. Guided waves were generated in the lower plate and couple into the top plate.

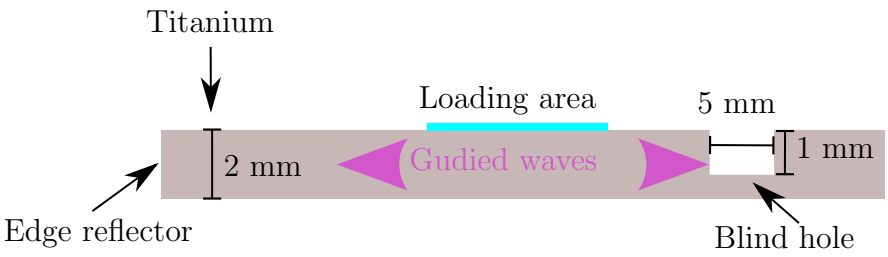

Figure 3.8: Diagram of the simulated plate with a blind hole. Guided waves were generated and enhanced in both directions.

overlap, the A_0 mode will become a multilayer mode ($2h$) [112].

In this experiment, a lap joint was modelled using an FEA tool (PZFlex, WAI, USA). For the plates, 2 mm thick aluminium sheets were used. 600 μm thick epoxy and a 200 μm thick inclusion of castor oil was used for the defective joint. Approximately a third of the 60 mm wide overlap was consumed by the defect and it was placed 500 μm from the incoming edge of the epoxy.

Recursive feedback was performed on the lower of the two plates with the aim of generating a guided wave toward the joint. The process was repeated on an uncontaminated joint so that a comparison could be made.

3.4.2 Defect Localisation in a Titanium Plate

In this second numerical experiment, recursive feedback was applied to a 500 mm wide, 2 mm thick titanium plate with a defect. At one end lay the edge, and at the other end lay a blind hole, 5 mm in diameter and 1 mm deep. This is shown in figure 3.8. Note that the distance from the loading area to the hole and edge is irrelevant since the attenuation was relatively low over the range (< 0.5 dB).

Here, recursive feedback was used in two ways. Firstly the scheme was used to excite toward the edge of the material. In the second operation, the waves were directed toward the hole. The out of plane surface displacements over the transmitting area were monitored for reflections. Comparisons between the two enhancement directions should indicate where the defect lay. The higher intensity reflections from the two directions will indicate the location of the defect. Exact localisation is difficult because of the dispersion of the

propagating waves. However, this can be compensated for [113]. Dispersion curves were acquired to observe any specific attenuation or reflection of modes.

3.4.3 Results and Observations

Figure 3.9 shows the dispersion curves for a lap joint with and without contamination. The dispersion was acquired from the top of the two plates. The out of plane surface displacements were recorded at several locations.

The same process was applied to the defective plate experiment, the results of which are presented in figure 3.10. The results are given in relative intensity (dB). In the case of the lap joint, the reference is the maximum value taken from the non-contaminated recording. In the case of the defective plate, the maximum value from the edge enhanced direction dispersion was used.

Returning to the uncontaminated lap joint, two modes are visible, A_0 at the top and S_0 at the bottom. The A_0 mode is the most predominant. Both modes are centred around the 700 kHz-800 kHz frequency range which was the bandwidth of the excitation waveforms. The same is true for both the dispersion curves in figure 3.10.

There was a significant loss of energy in the A_0 mode when the contaminant was introduced into the lap joint. Either the contaminant absorbed A_0 entirely or there was general attenuation of signals and a mode conversion took place from A_0 to S_0. By comparing with the dispersion relation of the known good joint, it can be shown the bond was defective.

In the defective titanium sheet (figure 3.10), A_0 and S_0 modes can also be seen. In the top image, guided waves have been excited toward the edge and thus away from the defect. Although the enhancement direction was away from the defect there was some small reflection from the residual energy propagating in the opposite direction. The modes are not complete in the edge direction, and there has been some loss of both modes at 700 kHz. When the guided waves were directed toward the defect, a 10 dB increase of A_0 and a 5 dB increase in S_0 was observed. From this magnitude increase, it can be deduced that this was the direction of the defect.

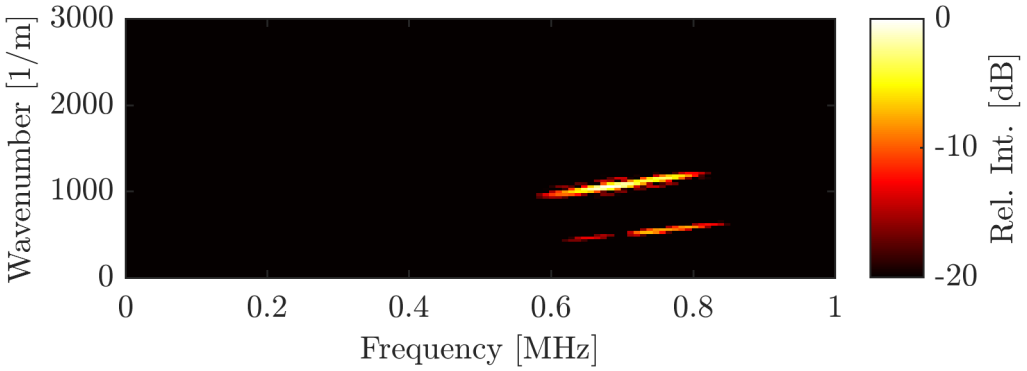

(a) Uncontaminated lap joint

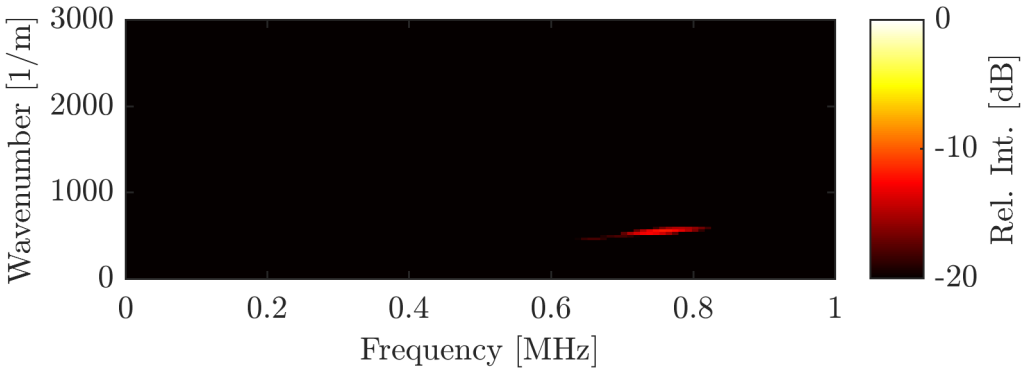

(b) Contaminated lap joint

Figure 3.9: The dispersion relations of lap joints with and without contamination. The peak value of the uncontaminated has been used as a reference. Attenuation and mode conversions have occurred in the contaminated case.

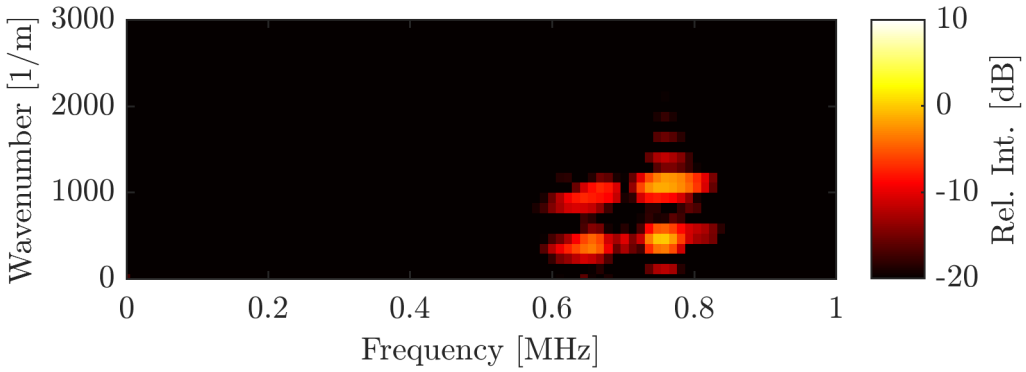

(a) Reflected from Edge

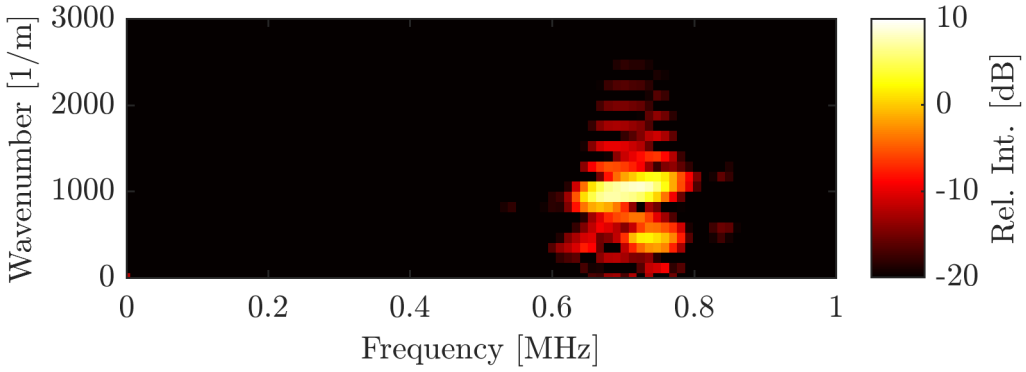

(b) Reflected from Defect

Figure 3.10: Dispersion relations reflected from a defect in each enhancement direction. Top: Guided waves were enhanced in the opposite direction to the defect so there was only a small reflection from the defect. Bottom: Guided waves were enhanced toward the defect so there was a much larger reflection.

3.5 Source Influence

Lamb waves can exist in rods, thin plates [66] and cylinders, where the boundaries are in close proximity [84]. When the surface is loaded, Lamb waves form, which are the superposition of bulk and longitudinal waves [46], [84]. Lasers [114], EMATs [68] and ultrasound transducers can all be used to generate Lamb waves. EMATs are often the preferred source for buried pipes and where source influence is undesirable. Large bonded PVDF and PZT 2D apparatus are usually used in SHM [70], [73], [88], [94], [95], [113], [115], [116]. Bonded PVDF is sometimes preferred in SHM because of its low cost and low source influence [71]. PZT which can be bonded to curved surfaces [117] has shown great range however [118], [119]. PZT ultrasound transducers have more source influence, but the effects are well understood [14]. Moveable PZT transducers arrays are more commonly used for the inspection of plates [69] and pipes [61]. Single crystal materials look promising, which might enable generation of very long range guided waves [120].

When using an array transducer a couplant is usually required for proper transduction. The choice of couplant is often dictated by the application and so the scheme has been tested with various couplants to assess its robustness to different environments. Couplants of oil, water and no couplant (air) were tested in simulation. Dispersion curves measured for oil and water in each enhancement direction are shown in figures 3.11 and 3.12 respectively. The same simulation parameters have been used as in figure 3.1, however only 7 iterations of the scheme have been executed to conquer the increased simulation time incurred modelling the air. In addition, a $\lambda/4$ matching layer and a $\lambda/8$ thick wear plate have been included in the simulation. Oil and water behave almost identically, with a 15.6 and 15.5 dB peak enhancement achieved with each couplant respectively. This can be attributed to their similar acoustic impedances. Using no couplant (not shown) performed extremely poorly; only very low-frequency components of the windowing function coupled into the waveguide and no enhancement was apparent. The peak value from the enhanced direction of each couplant was used as a power reference.

As with any contact ultrasonic experiment, the influence of the transducer can affect the results. There are two particular nuances of this experiment

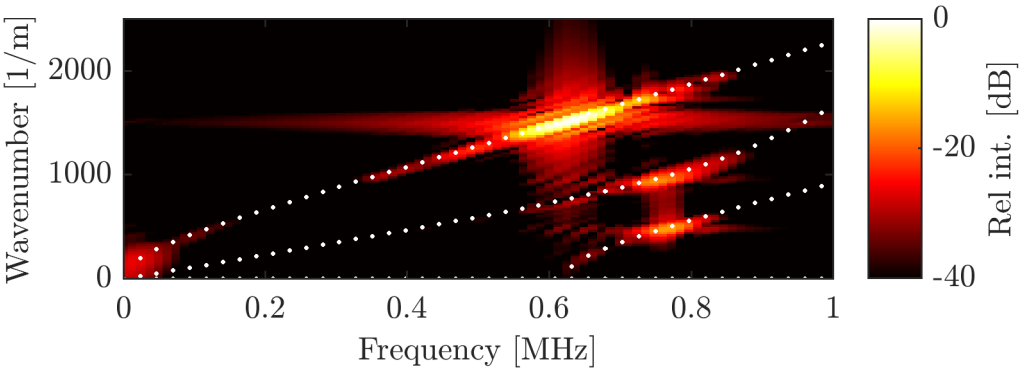

(a) Positive direction ($+Z$)

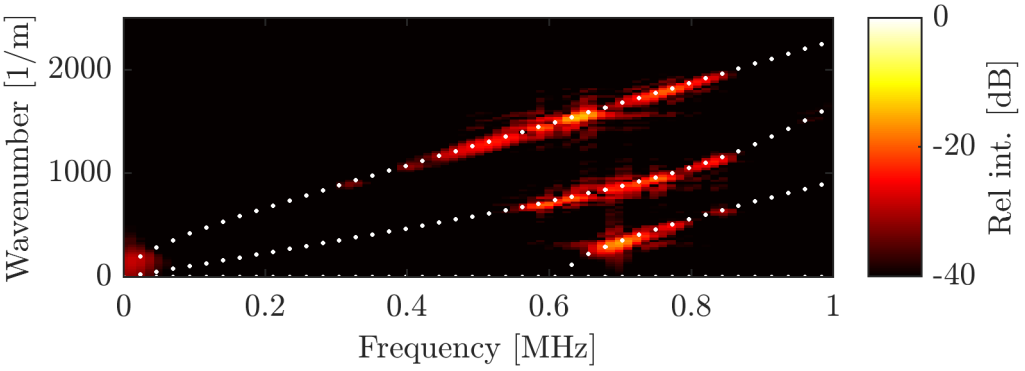

(b) Negative direction ($-Z$)

Figure 3.11: Results of enhancement using an oil couplant.

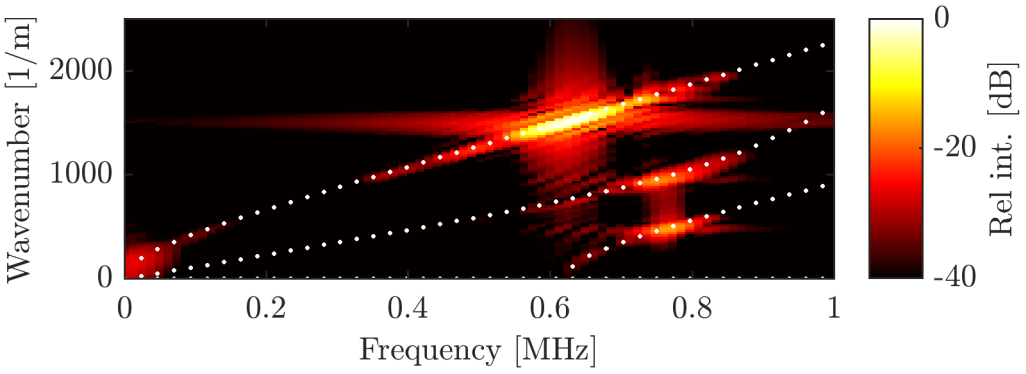

(a) Positive direction ($+Z$)

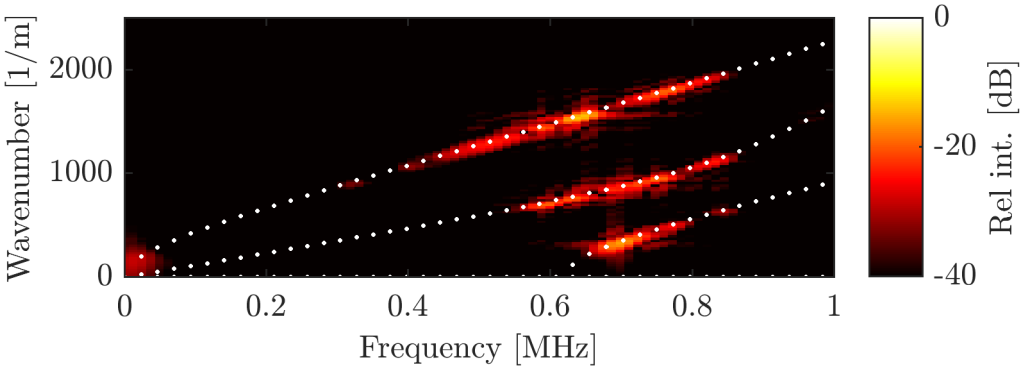

(b) Negative direction ($-Z$)

Figure 3.12: Results of enhancement using a water couplant.

which are noteworthy. First is the effect of loading applied to the transducer. Presuming that the contact area for each element in the array is far smaller than the wavelength of mode m [105], the coupling coefficient between the waveguide and the array element is:

$$C_{\mathrm{m}}(z) = S * \frac{V_{\mathrm{m}}^{*} \cdot T \cdot \hat{k_1}}{4P_{\mathrm{mm}}} e^{-i\beta_{\mathrm{m}}(z-z_0)} \tag{3.8}$$

Here, S is the area that the given element contacts the waveguide, V_{m} the particle displacement distribution, T the surface traction and P_{mm} is the power density. $\hat{k_1}$ is the unit vector normal to the waveguide. The convolution $S * ...$ has been used in place of an integral, since $a * f(b) = a \int f(b)$. z_0 is the location of each element in the array.

This equation describes the coupling coefficient of a particular mode with distance. When the dot product with $H(\omega)$ is made, the amplitude of a given mode at a given distance can be found which was given earlier in equation 3.2. $H(\omega)$ described the wave propagation while $C_{\mathrm{m}}(z)$ describes the influence that each element has on the amplitude. More detail on the derivation of these equations is available [105] but is beyond the scope of this section.

The significance of this $C_{\mathrm{m}}(z)$ term to this section is that as source loading is increased, modes with a wider particle displacement distribution will increase in magnitude more than modes with a narrow displacement. For this reason, the pressure applied to the transducer should be carefully considered when comparing the magnitudes of modes.

The second noteworthy influence of the transducer is particular to the recursive feedback scheme. The scheme reinforces modes as they are presented to the transducer. It is possible that under the correct conditions modes of the system may be reinforced rather than only of the waveguide. If the transducer is modelled as a single mass on top of the waveguide, then damping may occur. More significantly, individual matching and wear plate layers may incur the creation of waves not dis-similar to multilayer modes. Fortunately, a typical $\lambda/4$ thick matching layer is thin compared to the waveguide and so when separated by a wear plate and couplant is likely to have only a small influence on the experiment. Any system modes will likely convert to single layer plate modes at the boundaries of the transducer. Bounds were applied to the cross-

correlation algorithm (3.5). The bounds were defined in equation 3.7 and were chosen to further discourage system modes, as acoustic energy that has not travelled twice through the non-active layers of the transducer were temporally discriminated. Observations from simulations that include these layers confirm this. Finally, since the experimental results are free from spurious modes and align well with theoretical results it can be concluded that plate modes have been enhanced as opposed to system modes when the given experimental parameters were used.

3.6 Discussion

For the experimental results, the dispersion curves display good SNR, attributed to good coupling between transducer, honey and waveguide. It is possible to generate Lamb waves using air-coupled transducers, but mode choice is limited and the transducers are intolerant of small changes in angle [121]. Additionally, an initial excitation centred around the transducer's centre frequency was chosen to maximise energy in the waveguide. The dispersion curves show that most of the energy was between 2-3 MHz, as expected.

Figure 3.13 shows how the amplitude ratios for each direction change with respect to frequency. For each iteration, the difference between the maximum value in $+Z$ and $-Z$ at each frequency was calculated. Only the bandwidth of the chirp was considered. The green line represents the first iteration, this line is almost completely flat indicating there is almost no difference in power in each enhancement direction. The red line represents the fourth iteration. Here there is a peak increase of approximately 12 dB in the frequency range of the excitation. In the final iteration, which is represented by the blue line, the peak amplitude ratio has increased even further to a maximum of 34 dB. Although some general increase in enhancement with each iteration is apparent in this graph, a better metric is power density which can be obtained through numerical integration of the linear amplitude ratios. The power densities are shown in table 3.1. The power reference here is the power density from the first iteration.

The choice of initial excitation will change which modes may propagate,

Table 3.1: Power densities for different iterations

Iteration	Power Density (dBHz)
1	0
4	20.96
31	51.39

although unlike other schemes, the scheme will enhance all valid modes. For example, a broadband impulse will excite many modes across a large frequency range. Conversely, with a narrowband linear chirp, only modes with a non-infinite velocity in the frequency range of the linear chirp can be observed. While the designer is still in the process of finalising experimental parameters, it can be desirable to use a broadband linear chirp to increase the chances of exciting a mode, or to excite multiple modes. However, it should be noted that using a broadband signal reduces temporal resolution of defects [122]. The choice of initial excitation is critical to the success of the scheme. Experimentally and in simulation, a very narrow chirp was used for the initial excitation in the scheme. The use of a chirp facilitates pulse compression which allows the signal processing chain to approximate the transport time of the guided waves between elements. For these reasons, impulse excitations are not appropriate as they cannot be resolved in a bandwidth limited system. The higher the time-bandwidth product (TB) the more accurate the approximation of the delay. However, the bandwidth factor is limited by the transducer. So the length of the excitation must be increased, which in turn reduces resolution. Conversely, a reduction in the excitation length means less energy can propagate in the waveguide but TB is reduced. A balance must be struck. Despite this analysis, the reduced power budget available when undertaking remote NDT inspections will likely have the biggest influence on the choice of excitation. Approximately 2 kW peak power was required during firing using the experimental parameters given here.

It may be difficult to direct the waves in materials that are either extremely thin or thick. This is because for a given frequency, f, wavelength λ decreases, and the scheme presumes that $L < \lambda$. Since only low order modes are being generated, there is no risk of the guided waves interacting with micro defects. Since $L < \lambda/2$, the array meets the spatial Nyquist limit and simplifies the

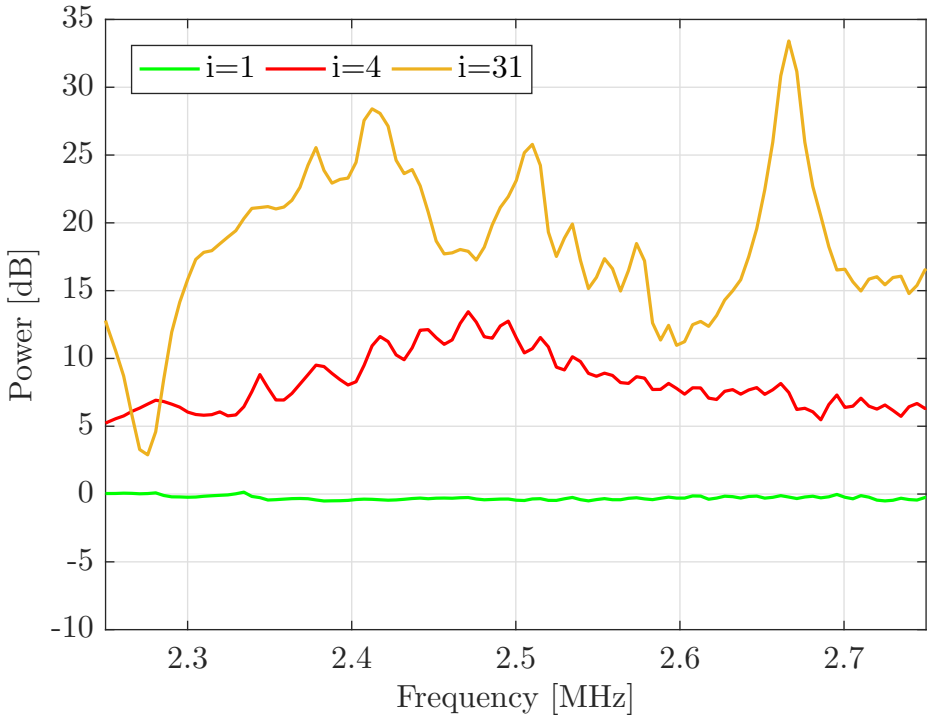

Figure 3.13: Amplitude ratios between each enhancement direction are compared for iterations 1, 4 and 31. The results are given in dB across the bandwidth of the transducer

experimental arrangement for measuring the resulting dispersion curves.

The signal processing chain consists of frequency filtering, cross-correlation and windowing. The chain is simple, and although difficult to implement with simple electronics, it can be easily achieved with software signal processing. Since no part of the scheme is real-time, the computational requirements were minimal. On a high-end desktop computer (Intel XEON E5-1620, 64GB RAM), each iteration took approximately 500 milliseconds to process including firing. Thus, with a 32 element transducer, a full 32 iterations were executed in approximately 16 seconds, although there is plenty of scope for optimisation. Most of this time constituted uploading TX waveforms to the UARP. Approximately 1 GB of memory was required.

If the waveguide or transducer are changed, the scheme will, of course, need to be re-executed. As the results indicate, the more elements used the better the power density and enhancement. The number of elements used however

is limited by the number in the array and the available computation time for deriving the waveforms for inspection.

The focus has been on the directional enhancement of low order modes, which can be easily separated with Fourier analysis. Mode control could be achieved through dispersion reversal which might make the scheme useful at higher frequency-thickness products where modes cannot be separated as easily during an inspection. Changes to input stimulus and additional boundaries applied to equation 3.6 might be required to achieve this.

For the simulation results, further investigation of the lap joint dispersion might indicate more about the defect to the engineer. The exact cause of loss of the A_0 mode might become apparent if a multi-layer dispersion relation were acquired from the overlap of the two materials. Phase velocities might also pertain to the composition of the inclusion.

The method used here for the inspection of the bond requires knowledge of the dispersion relationship of a known good bond for comparison. Alternatively, the dispersion of the guided waves prior and post entry to the bond could be compared to identify the flaw.

With the defective titanium plate, computational limitations meant that only 8 pressure loads were applied to the material. This achieved a 10 dB increase in power when directed toward the defect. Practically, it is feasible that this increase would be much larger as modern transducer arrays often contain 64 or more elements and it has been shown experimentally that the recursive feedback scheme's ability to direct guided waves improves as more elements are used.

3.7 Conclusion

Guided waves have many biomedical, NDT, and SHM applications. Their versatility makes them attractive in all these fields. Whilst Lamb waves are complex, they are now well understood, which has made research into their generation more accessible. They consist of many modes of oscillation, where each mode can be used for the inspection of different types of defects.

Control over direction is desirable as it allows localisation of defects, al-

though some processing is required to compensate for the dispersion if an accurate location is required. Whilst beamforming techniques do exist for the directional enhancement of guided waves, they require knowledge of the thickness of the specimen and its dispersion curves, which may be inaccessible to the operator. Arrays have been applied to solve this problem.

A scheme was devised for the uni-directional enhancement of Lamb waves. It required no knowledge of the material's dispersion curves. In the scheme, the first element of the array generates multimodal Lamb waves in the waveguide, while the adjacent element records the Lamb wave. In the next iteration, the recording is played back. The process is repeated until all elements are transmitting. In these several short iterations, the scheme can quickly resolve parameters required for direction enhanced guided wave inspection. From this point onward, guided wave inspection can be undertaken freely as excitations appropriate for the waveguide and transducer have been found.

The scheme was first demonstrated in a simulation where increased deformation was visible in the direction of the array's spatial influence. Based on equations relating to an existing scheme, a signal processing chain was devised to facilitate experimental validation, where the effect of uni-directional enhancement became apparent in iteration 4. Each successive iteration showed an increase of energy in the positive enhancement direction compared with the first iteration. When all elements were transmitting during iteration 31, an increase of 34 dB was observed in $+Z$, where only a 10 dB increase was observed in $-Z$ compared to the energy deposited from a single element. As further evidence, amplitude ratios between enhancement directions were compared for several iterations across the bandwidth of the chirp. Following numerical integration of this data between 2.25 and 2.75 MHz, it was shown that the power density increased between iterations.

Returning to simulation, the scheme was used to inspect two specimens. The first was a lap joint, a cured epoxy joint between two aluminium sheets. The lap joint was compared with an otherwise identical joint with an inclusion of castor oil. The second application was a titanium sheet with a blind hole defect.

For the defective plate, acquired dispersion curves from the transmitting area showed that there was a 10 dB increase in reflected power from one

direction. This indicated that the recursive feedback scheme can correctly discriminate the direction of a defect. With the lap joints, guided waves were generated in the bottom plate which propagated through the bond into the top plate. Dispersion relations acquired from the top surface showed that attenuation of the A_0 mode occurred when the bond was contaminated.

The source influence of the transducer was discussed as it may reduce the effectiveness of the scheme. Numerically, it was shown that the scheme could possibly reinforce modes of the system rather than of the plate alone, although this was not observed in simulation or experimentally. Additionally, it was shown that the traction applied to the transducer may change the amplitude of individual modes. In a simulation, several couplants were tested to verify the robustness of the scheme, as couplant choice is often dictated by the inspection environment. A wear plate and matching layer were included in the simulation and it was shown that oil and water performed well, achieving a 13 dB enhancement over seven iterations. Under the same operating conditions however, air performed extremely poorly exhibiting no directional enhancement.

This work shows that it is possible to control the direction of Lamb waves using an array transducer. The strategy described within does not need any prior knowledge of the material and is able to excite multiple modes whilst directing the guided waves. This may increase the accessibility and effectiveness of guided wave testing.

Chapter 4

Induction and Observation of Guided Waves in Bone

The behaviour of guided waves (GW) is highly related to the mechanical properties of the waveguide they are travelling in. Since the bone cortex is a relatively thin (< 10 mm) structure, it can host GWs at ultrasonic frequencies, and so researchers are actively investigating ways to obtain bone dimension and health data from ultrasonic GW measurements. One potential application is the diagnosis of osteoporosis, since existing techniques, such as dual X-ray absorptiometry, are expensive and involve repeated exposure to ionising radiation. Another potential application that is proposed here is measurement of skull bone thickness, which needs to be known in order to conduct transcranial therapy. Both settings provide unique challenges. In long bone, which is affected most by osteoporosis, the limited area which can be used for acoustic coupling, drastically reduces the quality of any dispersion measurements. In the transcranial therapy setting, the data must be co-registered with the therapeutic elements for it to be useful. For long bones, a new signal processing technique was used to introduce frequency-dependent phase shifts, which temporally aligns multiple transverse guided wave observations. This then allows typical beamforming steps, such as sum, to be used to prove or disprove the existence of guided wave modes through constructive interference. Multiplication was used to improve the contrast compared to an existing Fourier method. Although this technique produced artefacts that could be removed with simple

frequency filtering, the contrast of the high-order modes was improved when applied to ex vivo and in vivo bone. Numerically the technique was shown to improve the S_3 and A_3 mode intensity by 6 dB and 13 dB respectively compared with the existing Fourier method. Experimentally, it was found that the spectral leakage was lower than with currently used techniques to measure phase velocity along with improved sensitivity to high order modes. The technique could improve the reliability of osteoporosis diagnosis with ultrasound, but may also prove useful for acquiring dispersion images in NDT.

For skull bones, guided waves were generated and observed using a simulation of a typical transcranial array. A geometric relationship was found between the angle of incidence and the sonication point which was used to define a delay profile for the array. Guided waves were induced in skull and aluminium models, and a relationship between thickness and group velocity was found, although windowing and Hilbert transforms were necessary to remove the bulk-reflections. The estimated maximum thickness error using this technique was < 0.25 mm. The results showed that a therapeutic-geometry array could be used to measure skull properties using GW. Since the data is co-registered with the therapeutic elements, this method could be used to improve the accuracy of thermal treatments in the brain.

4.1 Introduction

In this section, the acoustical and mechanical properties of bone are introduced along with two potential applications of bone-guided waves.

4.1.1 Bone Types and Their Physical Properties

Bone is a complex viscoelastic composite [123]. It is anisotropic and governed by no less than five elastic coefficients, making it transversely isotropic [124]. At the mesoscale, bone is inhomogeneous, however, minimum representative volumes have been identified to allow homogenisation techniques to be used [125]. The long femur and tibia bones are comprised of cancellous, also called trabecular, *spongy* bone at the jointed ends, and marrow-filled tubular sections in the middle called cortical bone. Cancellous bone has been well-characterised

Table 4.1: Bone properties including speed of sound (SOS) used for modelling in the chapter,

Property	Symbol	Value (Cortical)	Value (Trabecular)
Density	ρ	$1969\,\mathrm{kg\,m^{-3}}$	$1055\,\mathrm{kg\,m^{-3}}$
Long. SOS	C_L	$3476\,\mathrm{m\,s^{-1}}$	$1886\,\mathrm{m\,s^{-1}}$
Shear. SOS	C_S	$1760\,\mathrm{m\,s^{-1}}$	$650\,\mathrm{m\,s^{-1}}$

[126] and characterisation of cortical bone, which can host guided waves [127], [128], continues.

It has been shown that in the transverse direction, an increase in porosity contributes to a decrease in compression and shear bulk wave velocities [129]. The trend is weaker in the axial direction however, meaning that porosity contributes to the anisotropy of the material. The Young's modulus of cortical bone has been measured [130] and strong correlations between the diagonal stiffness coefficients and density have been discovered. There are still many challenges facing full in vivo measurement of bone however [131]. Namely, the influence of the exterior soft tissue which has now been measured [132], and coupling which is made difficult because of variations in soft tissue thickness over the bone length. To combat the latter, probes have been developed to remove the error associated with poor alignment [133]. Despite the influences of the soft tissue, modes of the cortex can still be extracted with an inversion procedure [127].

Skull is essential to protecting the brain, and like long bone, is also a multi-layered hard tissue that is a combination of the two bone types. The layers can vary in thickness between a wide range of values which means that varying phase aberrations affect the coherence of any sound wave propagating through it. It, like all bone, is highly absorbing, so when exposed to high-intensity sound fields, heats rapidly [134]. Bone is therefore highly attenuative compared to other tissues [135].

The basic acoustic properties of bone, which are used throughout this chapter, are summarised in table 4.1. Figure 4.1 shows the composition of the two bone layer types in skull.

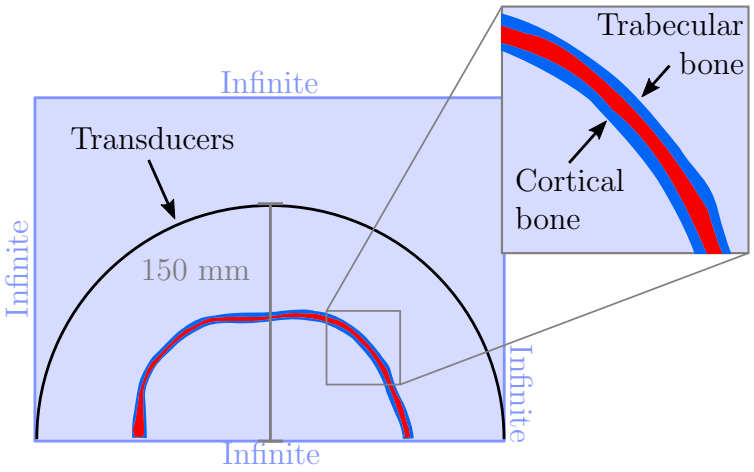

Figure 4.1: Cross-sectional view of assembly of the two bone types in skull. The skull was obtained by vectorising a CT scan of a healthy adult male [136]. Also shown: Boundary layers and dimensions used in subsequent simulations.

4.1.2 Applications of Guided Waves in Bone

Skull and long bones are thin (< 10 mm) media, so can both host guided waves. Since the mechanical properties of any media are highly related to the propagation behaviour of guided waves, observation of these waves has numerous biomedical uses.

In this section of the chapter, two applications of guided waves in bone are described. The first, osteoporosis assessment, is actively researched. A second, new potential application of using guided waves to assist transcranial therapy is introduced.

For Diagnosis of Osteoporosis

Osteoporosis is a disease where bone strength diminishes, drastically increasing the risk of a stress fracture. Of the 200 million women worldwide which it is estimated to effect [137], post-menopausal women are the most susceptible because of a drop in oestrogen levels. As the disease is not usually discovered until after a break, the world health organisation recommend screening women aged 65 or older [138].

Currently, the standard for identifying brittle bones is dual-energy X-ray absorptiometry (DXA). DXA works by irradiating the entire body with two

different intensity X-ray beams. When soft tissue is subtracted, bone mass density (BMD) can be measured. The BMD is then compared with a reference mean. Patients with a T score 2.5 deviations lower than this reference are considered osteoporotic [139].

There are several problems with this technique. It is not quantitative and it requires exposure to harmful ionising radiation. Practically speaking, the unwieldy size and high expense of DXA machinery make it of limited use for screening purposes. Authors also point out that BMD is not the only contributor to bone strength; structural properties such as thickness, cross-sectional area and moment of inertia are all contributing factors [123]. Furthermore, BMD cannot account for bone's complex microstructure of cracks, porosity and crystallinity which all provide a mechanism for breakage [123]. Diseases such as type 2 diabetes may result in a reduction of bone quality but not in a reduction of BMD [140].

Researchers in the 1990s identified ultrasound as an alternative approach [141], [142]. Several commercial ultrasonic systems were produced and correlations between the speed of sound (SOS) and BMD were discovered. However, as some indicate, a lack of understanding of results and standards meant quantitative ultrasound (QUS) was never properly adopted [143]. While trabecular bone loss has been the hallmark of osteoporosis, researchers continue to identify the importance of cortical bone in healthy [144] and healing bone [145]. With the recent discovery of additional guided wave modes from axial testing, there has a been a resurgence in QUS. Authors have found that the microstructure and elastic properties of bone effects QUS in axial transmission [146]. Recent work shows sex hormone levels and higher osteoporotic fracture risk align with QUS results [147]–[149]. All of these observations indicated that QUS may eventually supersede DXA, although a full understanding of bone quality and its relationship with acoustical properties is required first.

To complicate matters, there is currently no agreement about which guided wave signal to use. Proponents of first arriving signal (FAS) have shown that the velocity can be used to determine the thickness of the cortical bone [150]. This is not reliable however as the FAS may correspond to a flexural mode rather than a lateral wave if the thickness is less than one wavelength [151]. Conversely, the group velocity of the fundamental flexural guided wave mode

can determine the thickness of cortical bone [152]. This chapter concerns itself only with guided modes.

Potential for Transcranial Therapy Guidance

Focused ultrasound has been used extensively to treat numerous diseases [15], [153], [154] and provide palliative care [155], [156]. By focusing ultrasonic energy to a point using either an acoustic lens or phased array techniques [29], [157], tissue can be heated until ablation or to induce hyperthermia [158]. Researchers have begun focusing ultrasound in the brain [159] to ablate tissue or to modulate neurons [160], [161]. However, this is made difficult by the skull's properties discussed at the start of this chapter. Large amounts of energy are therefore required to achieve the desired heating at the target point. The effect is that the hard-soft tissue interface approaches unacceptable temperatures when exposed to high intensity focused ultrasound (HIFU). Experiments with cadavers have shown that the interface may reach 49 °C higher than the focus during typical exposures due to attenuation [162].

To combat this, researchers have astutely developed new transcranial therapeutic arrays. The arrays consist of a large number of elements [163]. The large element count means that local tissue heating is reduced as the acoustic power is distributed across a larger area, so the localised intensity is lower. Phased array techniques are then used to focus a beam to the target [159], [164], [165]. Unfortunately, beam steering is made difficult because skull's acoustic properties vary across its entire volume. In order for the energy to arrive in phase at the focal point, these aberrations must be compensated for.

Compensation of the phase aberrations is achieved with a computed tomography (CT) scan using time reversal [159]. There are a number of downsides with this technique, however. The first is that this adds a third point of failure and expense to the existing magnetic resonance imaging (MRI) and ultrasound required for therapy. It also requires exposure to harmful ionising radiation. The CT scan can only be performed before therapy and cannot compensate for patient motion or changes to the skull. Most significantly, however, is that the CT scan is not co-registered with the therapeutic array. This means that small errors in the location of elements or the patient could translate to incorrectly-

located ablation. One seemingly obvious solution to this might be to use the therapeutic array to image the skull with ultrasound. However, this is made difficult by the high attenuation of the skull bone and the limited resolution that can be achieved at non-attenuated wavelengths.

Estrada et al. have recently modelled and experimentally proven the existence of guided waves in murine skulls[1]. It is proposed here that these waves may be used for an alternative or additional imaging modality to guide transcranial therapy.

4.1.3 Objectives

In any case (skull or long bone), to acquire bone properties from guided wave measurements, models must be fit to incomplete experimental dispersion curves with an exhaustive search, although genetic algorithms have been applied to speed up the fit process [167]. Dispersion curves can be generated by solving the Lamb equations, but it has been suggested that normal lamb wave theory is limited when applied to regular bones [76]. With a supplementary group velocity filter, authors have solved the lamb equations to fit curves to experimentally obtained data [168].

The dispersion relation of guided waves may be presented in several ways. Phase velocity (C_{ph}) and wavenumber (k), both as a function of frequency are the most common. Although wavenumber relations are easier to obtain, interpretation is difficult as the curves do not have an easily identifiable shape or order of symmetric and antisymmetric modes. The phase velocity is the easiest to interpret as the modes are more readily distinguished, and changes in thickness usually result in an exact linear shift in the frequency domain. This is therefore the preferred form in literature [169].

In long bone, authors have obtained phase velocity dispersion measurements using two dimensional Fourier analysis, but this requires a high number of spatial measurements to detect higher order modes, which are necessary for a reliable fit to models. Unfortunately, only a small area of the tibia and radius are available for inspection clinically.

[1] H. Estrada, J. Rebling and D. Razansky, 'Prediction and near-field observation of skull-guided acoustic waves', *Physics in Medicine and Biology*, vol. 62, p. 4728, 2017.

In skull, there is comparatively less literature available on the subject. Although fundamental to this work, guided waves have only been observed in the near-field using optoacoustic excitation. This work should be extended by attempting to observe these guided waves in the far field with a concave configuration phased array transducer, typical of the type currently used therapeutically. Since the behaviour of bone-guided waves is so interlinked with the properties of the bone waveguide, GWs could be used as an alternative or additional imaging modality to guide transcranial therapy.

In summary, the objectives of this chapter, are as follows:

- Observe guided waves in both skull and long bone
- Devise a new method to measure phase velocity dispersion to improve the SNR of high order modes
- Measure skull properties, such as thickness, using skull-borne guided waves

4.2 Methods for Inducing Guided Waves

Schemes for inducing guided waves in bone are described in this section. Initially, the technique for inducing guided waves in ex vivo long bone is described. Subsequently, two types of purpose-built hardware (AZA and EVA) are introduced. Finally, a sonication technique suitable for the skull in a therapeutic context is described.

4.2.1 Induction in Ex Vivo Long Bone

Prior to an in vivo study, ex vivo experiments were conducted on a tibia bone harvested from a young bovine. The ex vivo study provided an opportunity to experiment with signal processing techniques, without the influence of soft tissue. Great care was taken to avoid damage to the bone when removing the soft tissue because scratches and cuts on the surface would create early reflectors or degrade transduction. Soft tissue was first manually removed from the sample using a scalpel. Following this, it was soaked in biological

Before mechanical tissue removal with the joint and cartilage still attached.

After soaking in washing powder

After soaking in a NaOH solution for 72 hours.

Figure 4.2: The ex vivo bone during different stages of the preparation process

washing powder (Ariel, Proctor & Gamble, UK) but was later moved to a 0.01 M sodium hydroxide (NaOH) solution to accelerate the cleaning process [170]. The sample was soaked for a total of 72 hours. The cleaning process is depicted in figure 4.2. To maintain its acoustic properties, the sample was stored in water when not in use. This process is known to minimise damage to the bone [170]. Any influence on the acoustic properties as a result would have been minor and the bone would have remained representative of an in vivo cortical bone waveguide.

The bone provides unique challenges because of its attenuating properties and uneven surface. In these experiments, a single element transducer was used to induce guided waves in the cortical bone waveguide whilst a phased array transducer was used to receive the guided waves. To achieve good coupling, a water-based gel was used in conjunction with a spring-loaded mount. The transmitting and receiving elements were placed close together to overcome bone's attenuation and achieve sufficient SNR. The separation used was approximately 30 mm.

Since bovine cortical bone is typically thicker than in humans [171], the frequency-thickness product is higher (mmMHz), so clinically used frequencies (1 MHz) have a tendency to excite higher order modes in bovine samples. A variety of stimulus were tested and a chirp was found to be the best at providing enough energy and bandwidth. A 1 MHz unfocused transducer (V303, Olympus NDT, Japan) was excited with a 1-1.5 MHz 100 cycle chirp. A 64 element probe (FPA 2.5, General Electric, USA) with a pitch of 0.33 mm

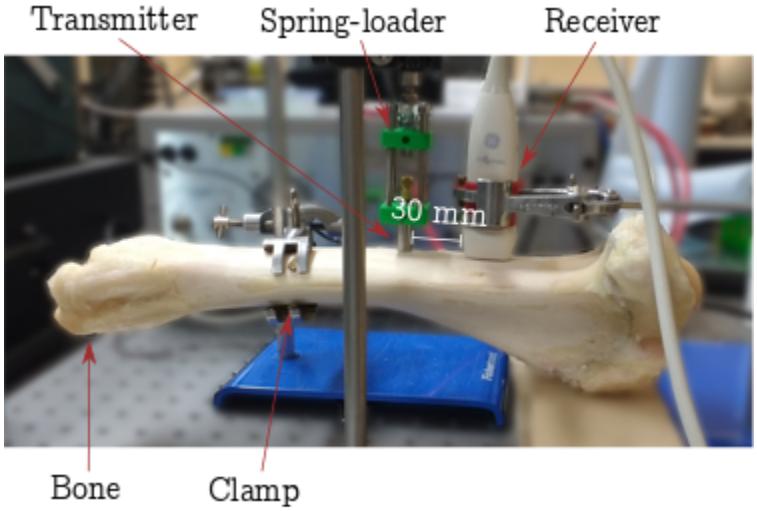

Figure 4.3: Picture showing arrangement of transmitter and receiver in the ex vivo long-bone experiments

was used for receiving the guided waves. Unlike the transmitter, its centre frequency was 2.5 MHz, but its high bandwidth of approximately 70% meant that it was able to detect the guided waves. The flattest area of the bones was used. The arrangement is depicted in figure 4.3. The clamp shown in the figure applied very little pressure and was far enough from the region of interest to not influence the propagation of any guided waves.

The incoming guided wave signals were digitised by the UARP II at a sampling frequency of 80 MHz. The UARP triggered a signal generator to produce the chirp which was amplified with a linear amplifier (A150, E&I, USA), such that the peak voltage supplied to the transducer, V_{pp} = 300V. The interconnects are shown in figure 4.4.

4.2.2 Induction in In Vivo Long Bone

For the in vivo study, a bespoke transducer was used that consisted of 24 receiving elements between two transmitting arrays. The transmitting and receiving arrays were separated by approximately 1 cm of kerf. The data was obtained from two prototype systems, code-named AZA and EVA [133] with the full consent of the participants and ethical approval. The transducers and excitation scheme of each system differed slightly and are summarised in

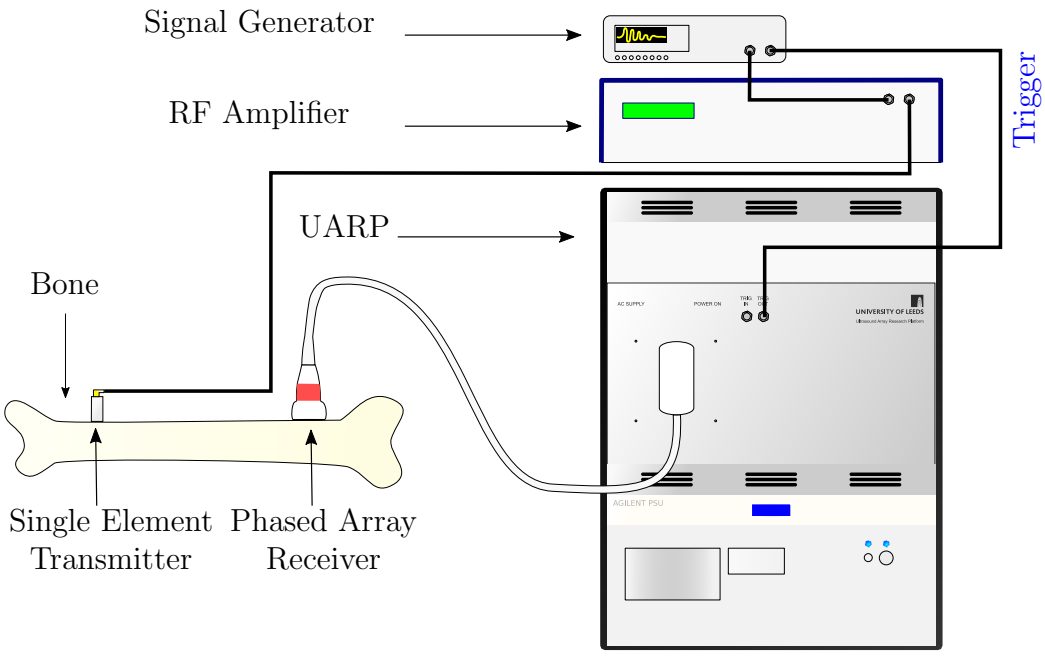

Figure 4.4: Interconnect used for capturing guided waves in bone. The UARP continuously triggers the signal generator to produce the desired a chirp. The bone was insonified with guided waves via a transducer and amplifier

Table 4.2: Specifications of the EVA and AZA systems

	AZA	EVA
Centre frequency	0.5 MHz	1 MHz
Pitch	1.2 mm	0.8 mm
Excitation scheme	Cortex focused	Iterative pulsing

table 4.2. Data was acquired by Kay Raum and Johannes Schneider of Berlin-Brandenburg School for Regenerative Therapies. The probes were developed at the Laboratoire d'Imagerie Paramétrique.

The two transmission arrays in each probe consisted of 5 transmitting elements. The unique arrangement of transducing elements allowed poor coupling from a rotation out of plane to be negated. If coupling between one of the transmission arrays and the bone was poor then data generated from the other transmission array could be used. In the EVA system, each transmitter was excited in turn and a recording was made. In the AZA system, the 5 elements were used to focus ultrasound at the cortex to maximise the guided wave energy. A continuous 2D FFT on the received signals allowed trained op-

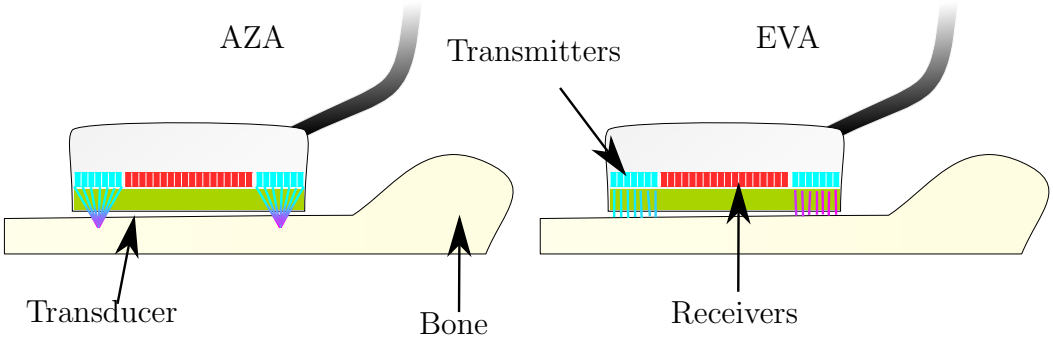

Figure 4.5: Diagram showing arrangement of transmitting and receiving elements in the EVA and AZA system transducers. In the AZA system, the elements are used to focus sound onto to the bone cortex, whereas in the EVA system, each element is excited in turn with a pulse.

erators to confirm good coupling was achieved. A diagram of both transducers is shown in figure 4.5.

4.2.3 Induction in Simulated Skull Bone

Skulls were modelled as hollow, approximately-spherical shapes that change internal (R_1) and external (R_2) radius over their spherical angles. The propagation of guided waves in spheres is complex [172]–[175] and leads to the propagation of many novel types of wave structures. Since this work concerns itself only with GW induction in a 3 layer model using curved geometry transducers, skulls were modelled as cylinders that extend infinitely into the $+Z$ and $-Z$ half spaces to simplify modelling. Cylinders were used because they can be modelled in 2D space, improving simulation efficiency. Aluminium cylinders were first considered to validate the technique as the thickness can be easily adjusted, and the high velocity of sound reduced the number of computational elements. A total of 32 different-thickness cylinders between 2 and 10 mm were considered.

Following this, three-ply skull models were simulated. Three nominal thicknesses of 3.97, 5.37 and 8.46 mm were considered. The skull consisted of a trabecular layer between two layers of cortical bone. The skull shape was ob-

tained from a CT scan of a healthy adult male[1], which was then vectorised so that the thickness of each layer could be adjusted. The nominal radius of the inner trabecular layer and the internal radius of aluminium phantoms was 87 mm. For the skulls, the percentage thickness of each layer remained constant; 35% and 29% for the cortical and trabecular layers respectively. The transducers and medium were surrounded by infinite half spaces of water. Absorbing boundaries were used at the fringes of the space. The simulation layout is shown in the introduction to this chapter in figure 4.1.

For simulation, the finite element analysis software (PZFlex, WAI, USA) was used. The maximum frequency considered was 2 MHz and the element size was 16 times smaller than the wavelength in the slowest material. Water was the slowest material used in the simulation, so the element size was approximately 740 µm. The time step for each element was adjusted automatically by the software with a time stability constant of 0.9 used. The total simulation width was 322 mm and the height was 161 mm. Each simulation was run for 108 µs.

To induce lamb waves in the media (skull or aluminium), obliquely incident plane waves were generated. Experimentally (not shown), it was found that an incidence angle of 60° was effective at exciting lamb modes in ex vivo human skull. The curved geometry of the therapeutic array meant that the angle of incidence was not the same as the plane wave steering angle. Figure 4.6 depicts the relationship between the two. Here, the blue shape represents a cross section of a skull, and point P is chosen to be insonified. To achieve the desired angle of incidence, a number of elements were selected from angle ϕ with a width of w. The elements generate a plane wave at an angle γ. The distances from the transducers and from point P to the geometric centre are R_t and R_2 respectively. R_1 is reserved for the inner radius of the skull. To calculate ϕ the following equation was used:

$$\phi = \theta - \sin^{-1}\left(\frac{R_2 \sin(\theta)}{R_\mathrm{t}}\right) \tag{4.1}$$

[1]R. Sharma and F. Gaillard. (2018). Platybasia, [Online]. Available: `https://radiopaedia.org/articles/platybasia`.

Once ϕ is known, the steering angle γ can be calculated with the following:

$$\gamma = \theta - \phi \tag{4.2}$$

Generally, it can be said that,

$$\gamma \neq \phi$$

Elements within a bounding box of width w were used to generate the plane wave. To calculate the steering delays for each element, the Cartesian grid was first rotated about the transducer's geometric centre and then again by the coordinates of the edge element:

$$\mathbf{C} = \left[\mathbf{B}\left\langle \begin{smallmatrix} \cos(\phi) & -\sin(\phi) \\ \sin(\phi) & \cos(\phi) \end{smallmatrix} \right\rangle - \mathbf{A}1_p^T\right] \left[\begin{smallmatrix} \cos(\gamma) & -\sin(\gamma) \\ \sin(\gamma) & \cos(\gamma) \end{smallmatrix}\right] \tag{4.3}$$

Here, $\mathbf{B}$ represents the selected elements' Cartesian coordinates. $\mathbf{A}$ is a vector containing the edge coordinates and is subtracted column-wise (p) from the rotated $\mathbf{B}$ coordinates. This is so the subsequent rotation of γ is performed around the edge element. The y coordinates of $\mathbf{C}$ now equal the distance to an imaginary plane at an angle γ to the elements. These distances y can be used to calculate the correct delays. For clarity, the rotation points have been included in figure 4.6.

The transducer consisted of 128 pressure loads distributed evenly between 0 and π radians. The nominally convex radius of 150 mm was increased by the thickness of the aluminium cylinder and half the thickness of the skulls. This was so that the distance between the surface and transducers remained constant between simulations. All selected transmitting elements were excited with a broadband Blackman-Harris shaped wavelet. Hamming window apodisation was applied to reduce side lobes. For the aluminium models, the centre frequency was 200 kHz. Whereas for the skull models, 67 kHz was used.

Unlike long-bone, only group velocity was considered. Whilst phase velocity would be preferable as it gives more information, it requires a reference phase which cannot be easily obtained with the geometry used. Figure 4.7 shows the range $[a - b]$ of frequency-thickness products that were considered for the aluminium. In this range, the changes in group velocity of the F$(1, 1)$

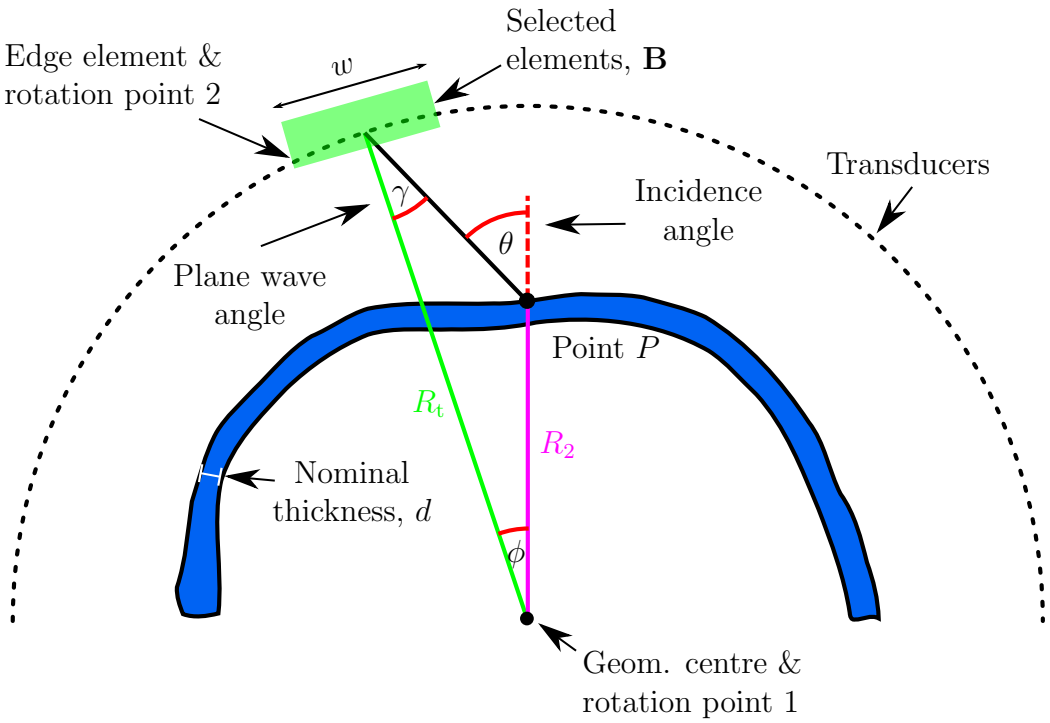

Figure 4.6: Geometry of simulation, the blue represents the vectorised skull shape and the dashes represent the transducers. The correct transmitting transducers must be selected from the array to achieve the desired angle of incidence. The steering angle differs from the angle of incidence, so the element coordinates are rotated about the two indicated points first.

and F$(1,3)$ modes should be visible. Similarly, figure 4.8 also shows the group velocity for the first order flexural modes in skull, with the three considered fd products shown with red lines. Both of these figures were generated using GUIGUW [109].

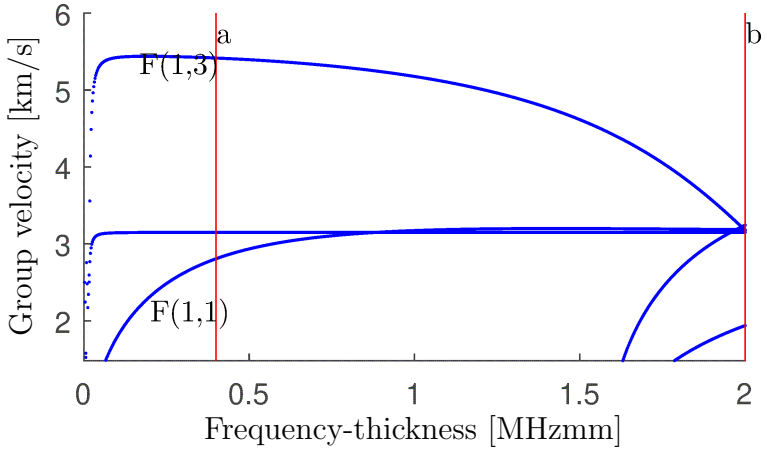

Figure 4.7: The group velocity of the first order flexural modes in an aluminium cylinder. The red lines show the range of thicknesses that were considered.

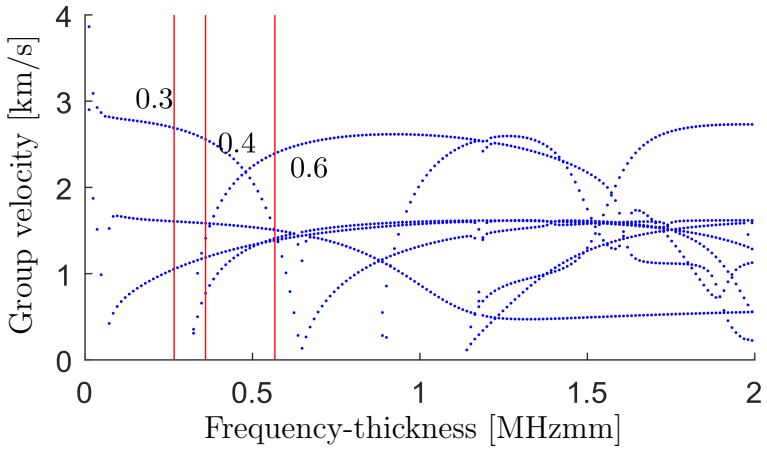

Figure 4.8: The group velocity of first order flexural modes in a three layer skull cylinder. The red lines show the three different thicknesses of skulls that were considered.

4.3 Phase Velocity Measurement in Long Bone Using Phase Shift and Multiply (PSAM)

A number of techniques already exist to measure phase velocity with varying suitability and effectiveness. In anisotropic solids, a π shift [176] or zero crossing [177] in time can be introduced through displacement, to measure phase velocity. This is difficult to achieve reliably at high frequencies [176] and is particularly inappropriate for lamb waves as they are multi-modal. The amplitude spectrum method is more appropriate for solids with close proximity boundaries but is still not applicable to multi-modal waves [178]. When dealing with only low order modes, a wavelet transform may be used to separate modes [179].

The two dimensional Fast Fourier transform (2D FFT) is most commonly used for the separation of modes in time domain signals [89], [180]. Fourier analysis can also be performed on smaller segments of the recorded signals to produce time-frequency plots [181]. By measuring the surface displacement at many points along the surface of a waveguide, a matrix of time-space dimensionality can be obtained. When the Fourier transform is applied, a wavenumber-frequency map can be generated. Since $k = 1/\lambda = f/C_{\text{ph}}$, elements can be re-arranged to form a phase velocity dispersion map [71], [182]. This works well but requires a prohibitively high number of spatial measurements to detect higher order modes. Due to the aforementioned limitations of skull bones; attenuation and soft tissue influences, this method is ineffective. For the accurate assessment of bone using QUS, a technique that is able to achieve a high SNR from a small spatial area is necessary.

To overcome these limitations, some authors have used singular value decomposition (SVD) [182], [183] with the AZA and EVA systems to filter the modes before applying the FFT. This technique is highly effective at removing noise. However, there are some limitations, SVD is a statistical method and relies on reliably receiving the spatial plane wave on all elements of the transducer which cannot be guaranteed. The technique also requires two thresholds be heuristically chosen, which may be prone to error.

In this section, phase shifting is applied to allow the temporal alignment of

modes, such that additional beamforming-style mechanisms may be employed. As an example, multiplication will be used to implement a DMAS-style (delay multiply and sum) beamformer[1] in an attempt to increase the contrast of modes.

Using short time Fourier transform (STFT), experimentally obtained group velocity has shown good agreement between bone and a hollow cylinder models [185]. More recently, however, authors have shown a free plate model can best predict the guided waves propagating in tubular bone-mimicking phantoms [186]. This follows 3D simulation work by others that show cortical tubular shells have identical SOS to plates of the same thickness [151]. Accordingly, an aluminium plate will be used to explain the principals and demonstrate the technique.

4.3.1 Premise

Consider a transducer mounted normally to a waveguide as shown in figure 4.9. The in-plane direction of motion is labelled Z. As the acoustic guided waves travel across the surface of the transducer, the out of plane displacements can be recorded and concatenated to give a matrix $\mathbf{M}$, of dimensionality time and space. An example is given in figure 4.10. In this instance, a 5 mm thick aluminium plate has been loaded over a very small area (< 100 μm) in an FEA simulation (PZFlex, WAI, USA). A 1.5 MHz centre frequency Blackman-Harris shaped pulse was used for the load. Both low order Rayleigh-like modes and high order modes are visible.

The Rayleigh-like S_0 mode is the most apparent as indicated by the dark line. Other modes are visible which appear more faintly. The general angle at which grouped wave packets appear in the image is dictated by the group velocity.

An infinitely fast wave would appear as a completely horizontal line, i.e., faster waves appear to be more horizontal than slower waves. This is because they move faster across the transducer array and thus travel more distance in

[1] G. Matrone, A. Savoia, G. Caliano *et al.*, 'The delay multiply and sum beamforming algorithm in ultrasound b-mode medical imaging.', *IEEE Trans. Med. Imaging*, vol. 34, no. 4, pp. 940–949, 2015.

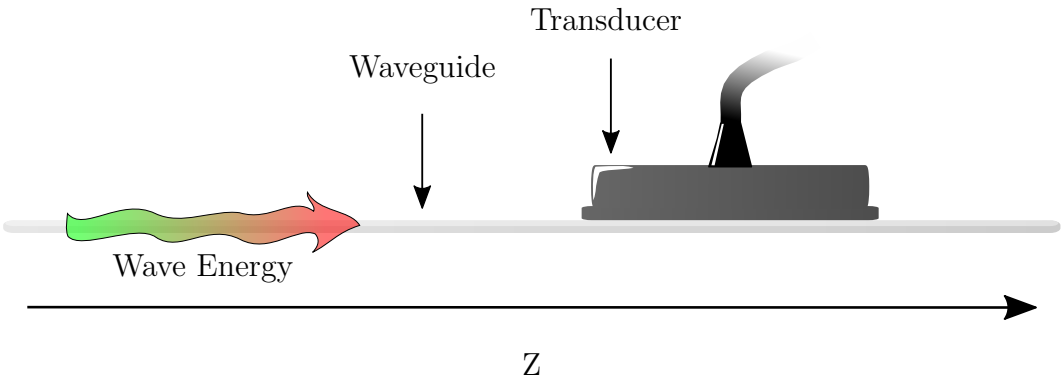

Figure 4.9: Diagram showing how out of plane displacement of guided waves are commonly recorded. Guided waves travel over the surface of a transducer mounted to the waveguide. The out of plane displacements can be recorded with a transducer.

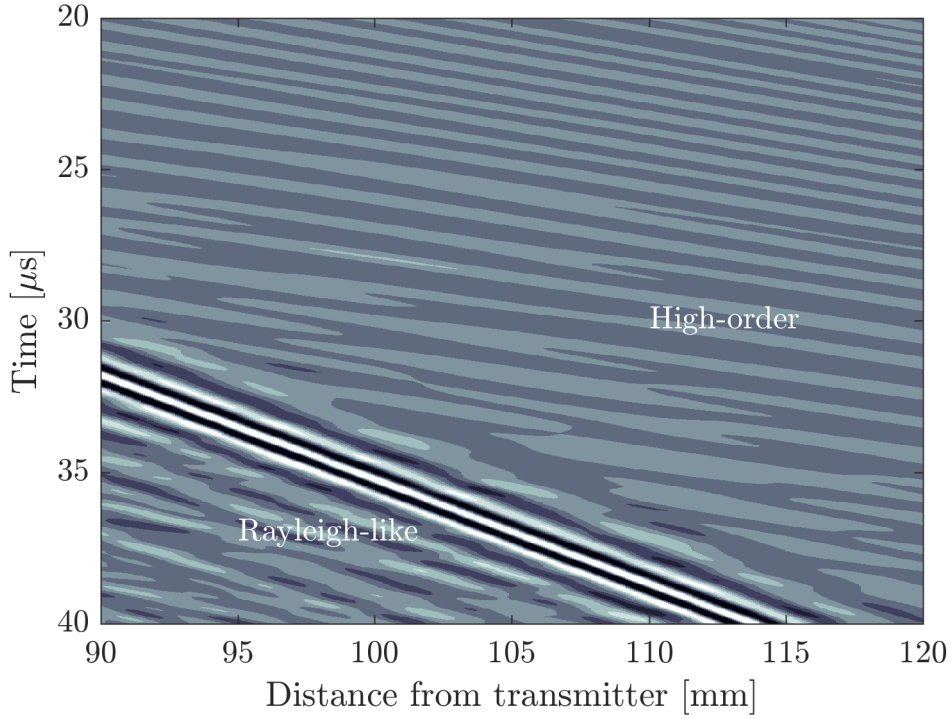

Figure 4.10: Matrix **M**. Out of plane surface displacements are concatenated to create a matrix of dimension space and time. High order and rayleigh-like modes are visible.

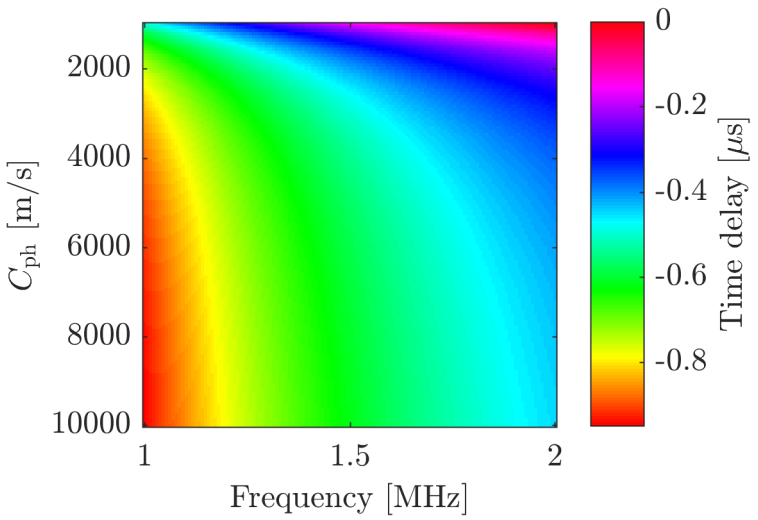

Figure 4.11: Time delays required to temporally align modes with a 0.5 mm pitch transducer. The delays change as a function of both frequency and phase velocity.

the same time. Conversely, modes' packets with a slower group velocity will approach a vertical line as they only achieve a small Z displacement in the same time. In addition to a group velocity, lamb waves also have a related phase velocity. Both velocities are frequency related. Within the time-space representation of modes, phases are visible as peaks and troughs within the group.

4.3.2 Phase Shifting

When the temporal frequency of these guided waves is known, delays can be applied to each element of the array transducer to temporally align particular modes, such that when they are summed, constructive interference takes place. Thus, when the engineer has knowledge of a specimen's dispersion curve and excitation frequency, delays can be chosen so as to assess the existence of a particular mode[1]. This relationship is described in equation 4.4.

[1]J. Li and J. L. Rose, 'Implementing guided wave mode control by use of a phased transducer array', *IEEE transactions on ultrasonics, ferroelectrics, and frequency control*, vol. 48, no. 3, pp. 761–768, 2001.

$$\lambda = \frac{L}{\beta + (t_0/T)} \tag{4.4}$$

Here, λ is wavelength, L is pitch, β is an arbitrary integer and t_0 is the delay increment to be applied to each element. T is simply $1/f$. Substituting $C_{\text{ph}} = f\lambda$ and $T = 1/f$ means the time delay can be expressed as a function of phase velocity and frequency, as in equation 4.5 ($\beta = 1$).

$$t_0 = \frac{L}{C_{\text{ph}}} - \frac{1}{f} \tag{4.5}$$

This, of course, means that different delays are required to extract individual frequency components for a given phase velocity. Figure 4.11 shows the required delay for a given frequency and phase velocity using a fixed 0.5 mm pitch transducer. It can be seen in the figure that the required delays change continuously with frequency, so achieving temporal alignment irrespective of the frequency or phase velocity is challenging.

Fortunately, as any time domain signal can be expressed as an infinite sum of its constituent frequency components, frequency dependent delays, which are phase shifts in the frequency domain, can be applied to the incoming signals to achieve alignment irrespective of frequency.

Digital Implementation

Consider $\mathbf{A}_{N,M}$, a time domain signal of N samples recorded at interval n from element m of an array transducer. Its discrete Fourier transform (in time only) is $\mathbf{X}_{\Phi,M}$, where ϕ is the interval of frequency. This is described in Equation 4.6 and defined in 4.7.

$$\mathbf{A}_{N,M} \xrightarrow{\mathscr{F}} \mathbf{X}_{\Phi,M} \tag{4.6}$$

$$\mathbf{X}_{\phi,M} = \sum_{n=0}^{N-1} \mathbf{A}_{n,m} e^{\frac{-j2\pi n\phi}{N}} \tag{4.7}$$

These complex coefficients represent the amplitude and phase of an exponential function. When these weighted exponential functions are summed, the

original time domain signal can be obtained.

A delay in the time domain maps to a phase delay in the frequency domain. Equation 4.8 describes this relationship when a delay of D samples is applied to the original time domain signal.

$$\mathbf{A}_{n-D,m} \xrightarrow{\mathscr{F}} e^{\frac{-j2\pi\phi D}{N}} \mathbf{X}_{\phi,m} \tag{4.8}$$

D can be replaced by $D(\phi, m, C_{\text{ph}})$, a function of frequency, element position and phase velocity to achieve the required phase shift for each frequency:

$$\mathbf{A}_{n-D(\phi,m,C_{\text{ph}}),m} \xrightarrow{\mathscr{F}} e^{\frac{-j2\pi\phi D(\phi,m,C_{\text{ph}})}{N}} \mathbf{X}_{\phi,m} \tag{4.9}$$

To form function D, first the substitution

$$f = \frac{\phi f_{\text{s}}}{2N}$$

is applied to equation 4.5, yielding 4.10.

$$\frac{L}{C_{\text{ph}}} - \frac{2N}{\phi f_{\text{s}}} \tag{4.10}$$

Here, f_{s} is the sampling frequency and the assumption is made that when $\phi = N$, $f = f_s/2$, the Nyquist limit. This simply converts a frequency into its corresponding bin number in a discrete Fourier transform (DFT), presuming of course that the DFT produces N frequency bins in the range $[\frac{-f_s}{2}, \frac{f_s}{2}]$.

Since equation 4.10 describes the real time delay applied in seconds per element, $D(\phi, m, C_{\text{ph}})$ can be derived by multiplying each instance of m by mf_{s} to obtain a value in samples for each element:

$$D(\phi, m, C_{\text{ph}}) = m\left[\frac{Lf_{\text{s}}}{C_{\text{ph}}} - \frac{2N}{\phi}\right] \tag{4.11}$$

This however means that as $\phi \to 0$, $D \to -\infty$, which would be impossible to implement, so a square window is applied to function D:

$$D(\phi, m, C_{\text{ph}}) = \begin{cases} m\left[\frac{Lf_{\text{s}}}{C_{\text{ph}}} - \frac{2N}{\phi}\right], & \text{for } \phi > 0, \\ 0, & \text{for } \phi = 0 \end{cases} \tag{4.12}$$

Finally, a frequency-space domain matrix, $\mathbf{P}_{\Phi,M}$ can be produced for a given phase velocity as follows:

$$\mathbf{P}_{\phi,m} = \begin{cases} \exp\left[\frac{-j2\pi\phi m(\frac{Lf_s}{C_{\text{ph}}} - \frac{2N}{\phi})}{N}\right]\mathbf{X}_{\phi,m}, & \text{for } \phi > 0, \\ \mathbf{X}_{\phi,m}, & \text{for } \phi = 0 \end{cases} \tag{4.13}$$

At this point, the matrix $\mathbf{P}$ contains a phase shifted guided wave signal from each element of the transducer. The signals are in the frequency domain, and phase shifts have been applied so that for the given phase velocity, all the frequency components are in phase. This forms the basis of the phase shifting aspect of the algorithm.

4.3.3 Generating a Dispersion Curve

The described process is then repeated for each phase velocity, o, in a user-defined search space to produce a three dimensional matrix, $\mathbf{E}$. The dimensions are space, frequency and phase velocity. $\mathbf{E}$ then contains phase-aligned frequency domain data for a total of O phase velocities, where each o indexes one value of C_{ph}. The formal definition of this matrix is as follows:

$$\mathbf{E}_{\phi,m,o} = e^{\frac{-j2\pi\phi D(\phi,m,C_{\text{ph}})}{N}}\mathbf{X}_{\phi,m} \tag{4.14}$$

Applying the inverse Fourier transform in the frequency domain only, returns the matrix to the time domain. At this point, summation in the dimension m would cause the temporally aligned waves to constructively interfere. Conversely, the wave packets that were not aligned would destructively interfere. To enhance this process as much as possible, multiplication was used instead:

$$\mathbf{Y}_{N,o} = \sum_{i=1}^{M-1} \mathscr{F}^{-1}\{\mathbf{E}_{\Phi,i,o}\} \times \mathscr{F}^{-1}\{\mathbf{E}_{\Phi,i+1,o}\} \tag{4.15}$$

$\mathbf{Y}$ is a series of time domain signals for each evaluated phase velocity index, o. Constructive interference will have taken place at particular frequencies and phase velocities. In the implementation described here, multiplication was used, although other signal processing techniques may be used to find the

Table 4.3: Simulation parameters for small and large area tests

	Large Area Sim.	Small Area Sim.
Spatial Interval	0.07 mm	0.4 mm
Total Area	80 mm	30 mm
Discrete Measurement Points	11429	75

temporal alignment of modes such as summation or cross-correlation.

Finally, to transform the matrix into the familiar frequency-velocity matrix, **S** is found by re-applying the Fourier transform as in equation 4.16.

$$\mathbf{S}_{\Phi,o} = \mathscr{F}\{\mathbf{Y}_{N,o}\} \tag{4.16}$$

4.3.4 Comparison with 2D FFT

To demonstrate the PSAM technique a comparison was first made with the 2D FFT method using the data obtained earlier from the simulated 5 mm thick aluminium plate. Two dimensional Fourier analysis was performed and the subsequent matrix was transformed into the C_{ph} domain using the substitution ($C_{ph} = f\lambda$). This process was then repeated but with a reduced measurement area and increased interval more typical of a transducer that would be used experimentally. The results from the FFT were then compared with PSAM using the same data set. The parameters for each test are summarised in table 4.3. In both cases, the sampling frequency remained at 100 MHz.

The large area simulation in figure 4.12 shows a phase velocity map generated from Fourier analysis. The modes are clearly distinguished and have good definition. The high order modes S_3 and A_3 are visible. Figure 4.13 shows the FFT and PSAM results for the decimated small area simulation data. Both results were normalised by the largest non-rayleigh wave mode. Theoretical results produced by GUIGUW [73], [108], [109] are overlaid. In both cases, the definition is reduced. PSAM has a large artefact near 0 MHz, but with the parameters used, it is inconsequential as it could be easily separated from the modes using simple frequency filtering. Despite this, PSAM is better at extracting the higher order modes.

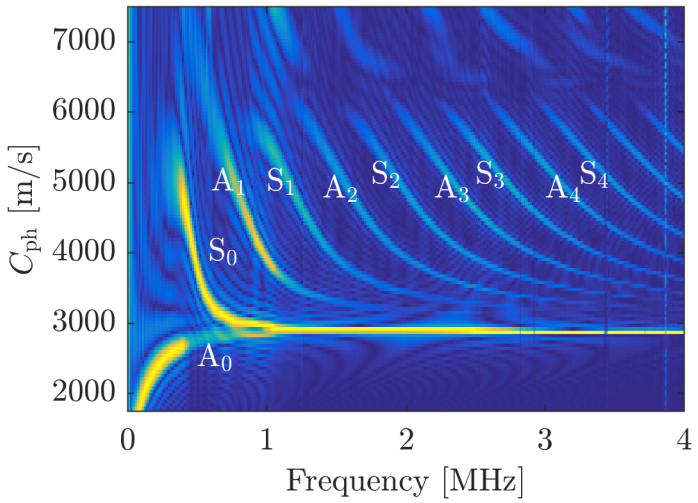

Figure 4.12: Dispersion obtained using FFT from a large area of an aluminium wave guide (simulation data).

The green line at 4200 $\mathrm{m\,s^{-1}}$ shows the phase velocity where the two schemes were compared in figure 4.14. This velocity was chosen because several modes can be observed in one dimension easily. The PSAM and FFT results are represented by the orange and blue lines respectively. At this phase velocity, both were able to extract the first 3 orders of antisymmetric and symmetric modes. At A_3 though, the FFT method begins to show a loss of sensitivity and there is a false-peak between A_1 and S_2 which may be a SH-mode wave. PSAM appears less sensitive at S_2, which may be due to a disruptive beamforming artefact that effects all phase velocities at that frequency. However, the amplitude of the S_3 and above modes are higher with PSAM: The FFT method was not able to resolve the S_4 or A_4 modes. Most significantly there was a 6 dB and 13 dB increase in the S_3 and A_3 modes respectively.

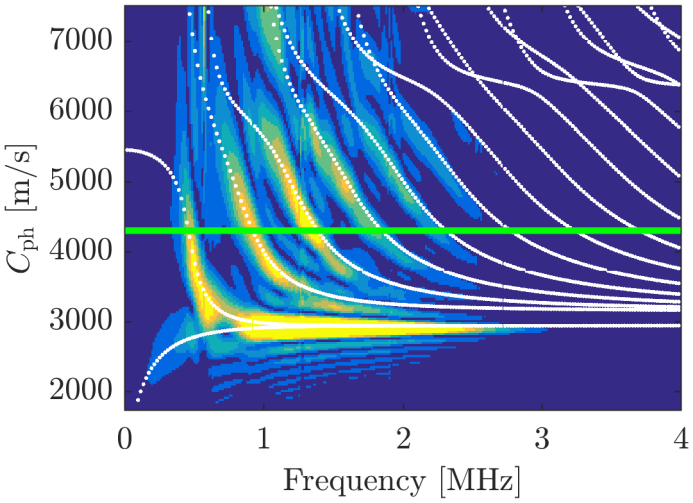

(a) FFT

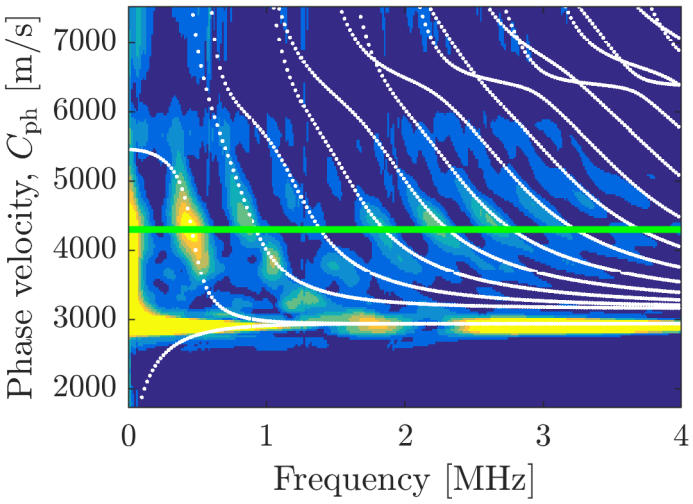

(b) PSAM

Figure 4.13: Dispersion curves obtained using both FFT and PSAM from a smaller sized area of an aluminium waveguide. The green line shows the point at which the phase velocity resolution is considered. Model data is overlaid in white (simulation data).

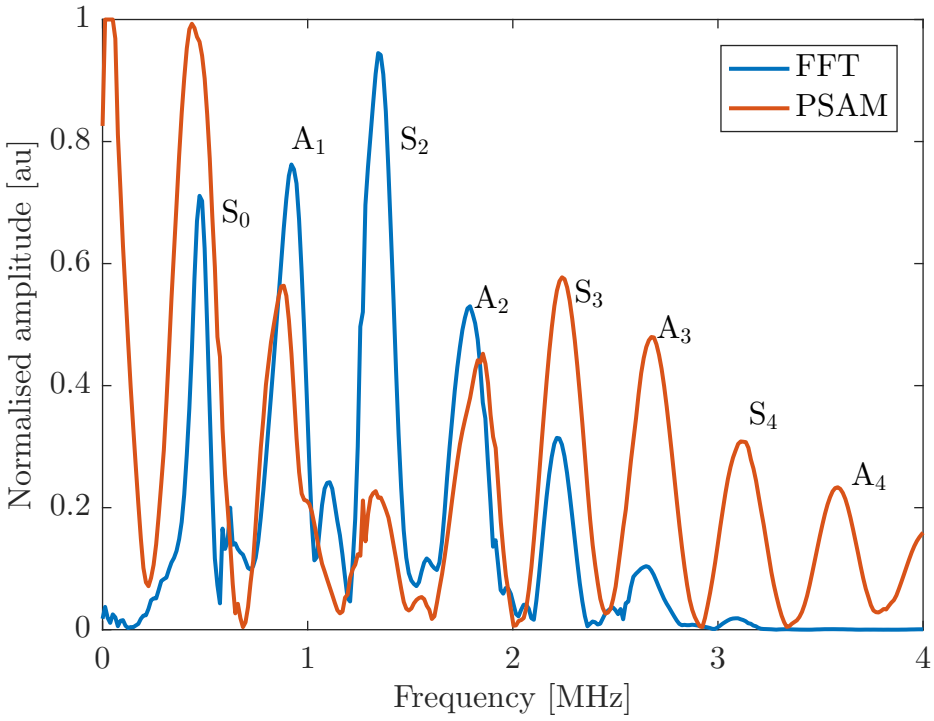

Figure 4.14: Detected modes at 8100 ms^{-1} using PSAM and FFT. The results are normalised. PSAM is able to resolve higher order modes.

4.4 Long Bone Results

The creation of dispersion curves with a high contrast is necessary to properly fit models and thus determine bone properties. Methods for inducing guided waves in long bone have previously been described and so in this section, the results from applying PSAM to the long bone data are provided and evaluated.

4.4.1 Ex Vivo

Figure 4.15 shows dispersion obtained from the bovine sample using FFT and PSAM techniques. Overlaid is a speculative 4.7 mm low porosity ($< 3\%$) model. The images show Raleigh waves well aligned with the theoretical model. For PSAM, the image also shows A_4, A_3 and S_3 but no model data is available for the latter so this alignment cannot be verified. The FFT results are similar although there is slightly more noise in the low-velocity region around 1 MHz. There is also an additional artefact at 1.25 MHz, that does not appear in PSAM results and can't be aligned to any of the modes.

4.4.2 In Vivo with EVA System

To improve the SNR of the results from the EVA system, a sparse array technique was employed that is described in the next section. However, due to the operational differences between the two systems, it was not possible to apply this technique to the AZA system data. Consequentially, for the sake of brevity, only successfully coupled and conditioned data from the EVA system is presented here. The remaining results have been placed in appendix A at the end of this thesis.

Additional Signal Conditioning

The spatial constraints of the transducer mean that the high number of receiving elements used in simulation and in the ex vivo experiment cannot be afforded. Fortunately, the redundant number of transmitting elements meant that a sparse array imaging technique could be used. If an ideal plate model is presumed, a shift in $-Z$ in transmitting element is the same as a shift in

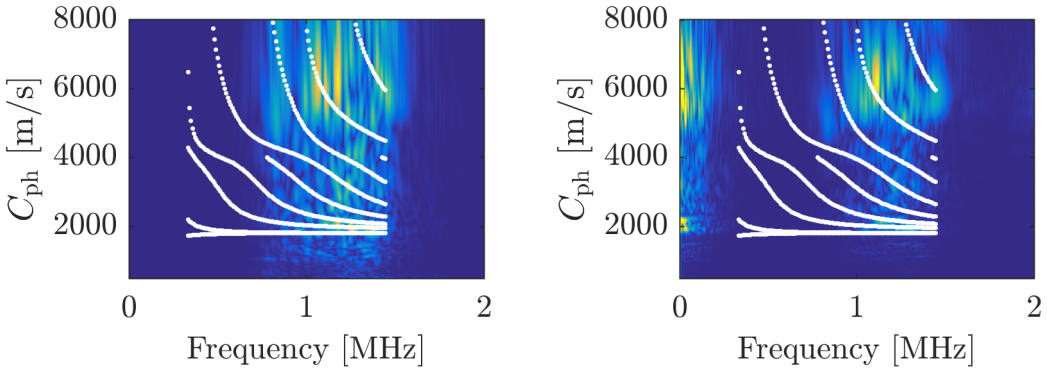

(a) FFT (b) PSAM

Figure 4.15: Dispersion obtained from bovine tibia using FFT and PSAM. A 4.7 mm low porosity bone model is speculatively overlaid.

$+Z$ of the receiving array (with a stationary transmitter). In both cases, the distance between the transmitting element and the first receiving element increases and all receiving elements are subject to the same attenuation resulting from the increase in distance. This is depicted in figure 4.16. Utilising this principle allowed a matrix that exceeded the real size of the receiving array to be produced.

The small step size between transmitting elements means there was inevitable overlap. However, this was advantageous because the averaging effect improved the SNR. There were R total receiving elements (index r) and Q total transmitting elements (q, per direction), thus the size of the sparse array was $R + Q - 1$. Of course, columns closer to the centre of the new sparse array had a larger amplitude because those segments had more contributing signals. When the matrix was averaged, those central segments had a smaller weighting than their counterparts at the fringes of the matrix because they had a higher overall amplitude.

The column density $\mathbf{D}$, represents the number of overlapping columns in the final matrix. For 4 receiving elements and 3 transmissions, the column density would be,

$$\mathbf{D} = [1, 2, 3, 3, 2, 1]$$

because there are two columns in the centre where there are 3 overlaps, and

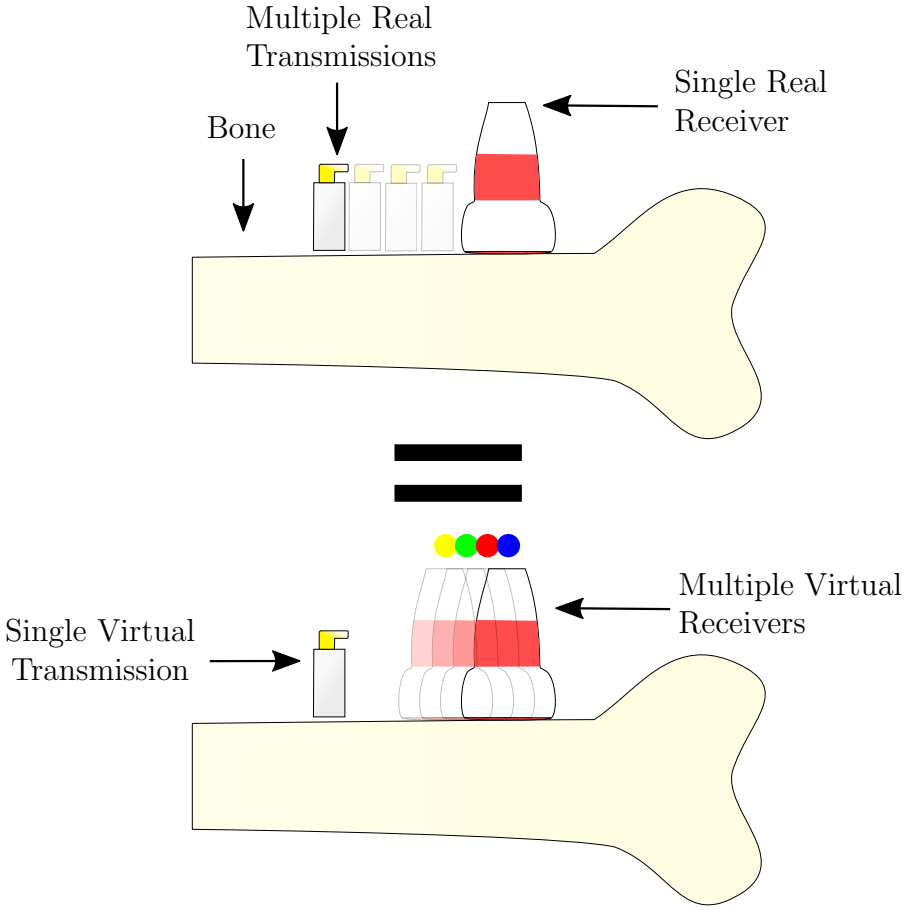

Figure 4.16: Sparse-array technique used to increase the number of sampling points for the EVA system experiments. A shift in the position of the transmitter is considered equivalent to a shift in the receiving array position, which causes overlapping of the obtained data. Each of the coloured dots represents each separate matrix that was obtained.

only one at the edges and so forth. **D** was calculated from the weight matrix, **W**, where each column and transmitter number is represented by horizontal and vertical co-ordinates respectively. Matrix **W** was generated as follows:

$$\mathbf{W}_{ij} = \begin{cases} 1, & \text{for } j \in [i, i+R-1] \text{ where } i \in [1, Q] \\ 0, & \text{otherwise} \end{cases} \tag{4.17}$$

Which, for $R = 4$ and $Q = 3$ would produce a matrix as follows:

$$\mathbf{W} = \begin{pmatrix} 1 & 1 & 1 & 1 & 0 & 0 \\ 0 & 1 & 1 & 1 & 1 & 0 \\ 0 & 0 & 1 & 1 & 1 & 1 \end{pmatrix} \tag{4.18}$$

The weight vector **D** then is the sum of matrix **W** in the transmission dimension, i:

$$\mathbf{D} = \Sigma_{i=1}^{Q} \mathbf{W}_{i,j} \tag{4.19}$$

The sparse-array image was appropriately weighted by column-wise dividing the image by **D**. Each column of the sparse transmit matrix was effectively divided by the number of contributing columns.

Dispersion Curves

Prior to measurement, subjects underwent a micro CT scan, and from this data, model dispersion curves were generated and compared with those obtained experimentally.

Figures 4.17 shows a dispersion curve obtained using both FFT and PSAM on the EVA system. The chosen direction has superior coupling. Here, the EVA data tend to align well with the models except for the S_0 mode, which appears at a much lower phase velocity and is likely caused by the known influence of the silicon coupling material [183]. Even with this alignment issue, the S_0 mode which appears at approximately 0.5 MHz is present, although it is much less intense with the FFT technique. Due to the reduced spectral leakage of the technique, PSAM has better separation of the S_1 and A_2 modes, although the latter cannot be verified because there is no model data available.

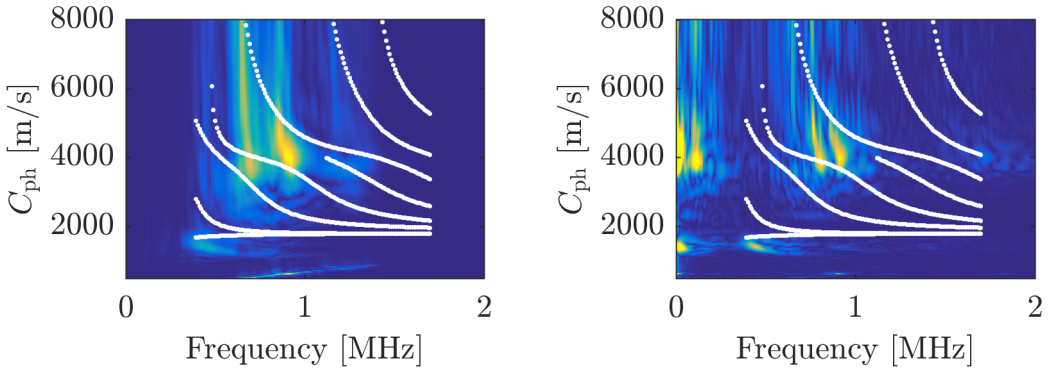

(a) FFT (b) PSAM

Figure 4.17: Dispersion obtained using the EVA system from direction 2 using both FFT and PSAM techniques. Model data acquired from a micro CT scan is overlaid in white.

4.5 Skull Results

Although a technique for inducing guided waves in skull has already been described, additional processing was required to extract the guided waves, which is described here. Dispersion curves from mathematical models were generated using GUIGUW and compared with the results obtained.

4.5.1 Group Velocity Changes

The majority of the energy in the field of view will consist of bulk reflection from the boundary between the water and medium. However, as the faster guided waves move around the cylinder, it becomes easier to separate the leaking energy from the reflection due to the difference in SOS. For this reason, an arbitrary transducer in the array, some small angle from the insonified area is chosen to acquire the signals. A large angle makes temporal windowing easier as the leaking waves become more separated from the reflected energy. However averaging effects are introduced; any changes in the waveguide that effects propagation will be less localised. Conversely, a small angle makes windowing more difficult but provides more localised information about the waveguide acoustic properties. In simulations, a liberal value of 70° was used. Figure 4.18 shows a snapshot from a simulation and demonstrates how after a

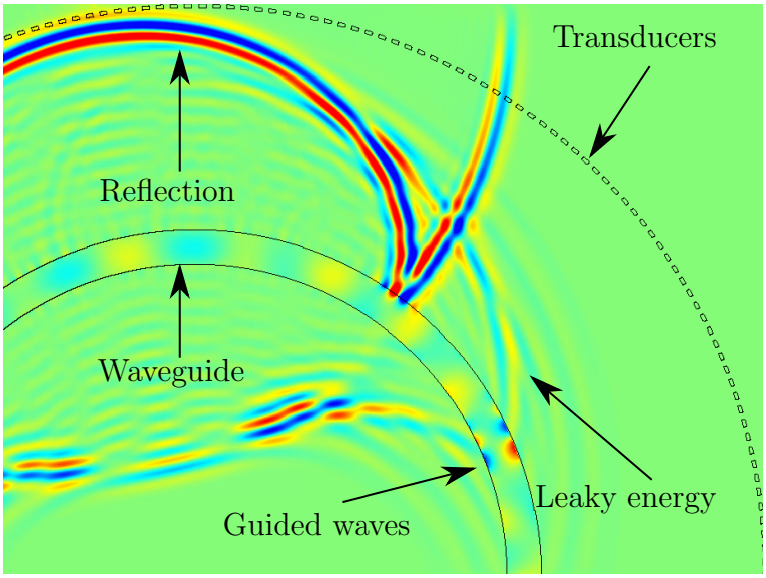

Figure 4.18: Snapshot from the simulation of the aluminium model. Guided wave modes travel faster than the reflected energy in an aluminium cylinder so can be temporally extracted using a transducer displaced from the source.

small amount of time the higher velocity guided waves are separated from the reflected energy (figure 4.19 for skull).

Accordingly, temporal windowing was first applied based on the propagation distance. Following this, the signal underwent a Hilbert transform to extract the envelope.

Figure 4.20 shows the signal envelopes for different thickness of cylinders. Each vertical line in the image is the Hilbert transform of the received signal for each thickness. The intensity was calculated by using the maximum observed amplitude as a reference. From the transformed signals, propagation time was subtracted. Each line was then concatenated together to form the image. Although the frequency is consistent between simulations, the thickness increases and so the fd (frequency-thickness) product also increases. Guided waves are known to change group velocity with changes in fd product, which is demonstrated in the figure. There is a change in the group velocity of two of its modes as fd increases. The theoretical group velocity is overlaid in white.

Similarly, figure 4.21 shows the results for the skull models. The envelopes for captured waveforms from the three different thicknesses of skulls are shown. Blue, red and gold represent 3.97, 5.37 and 8.46 mm respectively. Since the

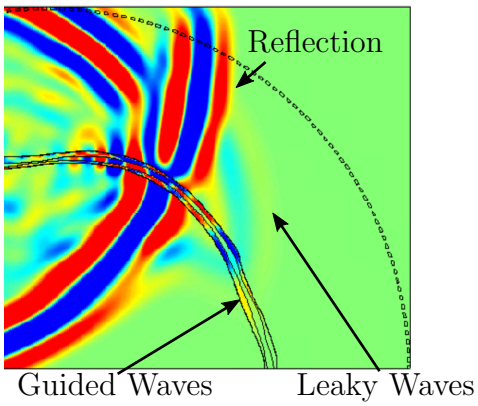

Figure 4.19: Snapshot from the simulation that demonstrates that three-layer skull models can host guided waves. Energy from these guided waves leak into the surrounding fluid.

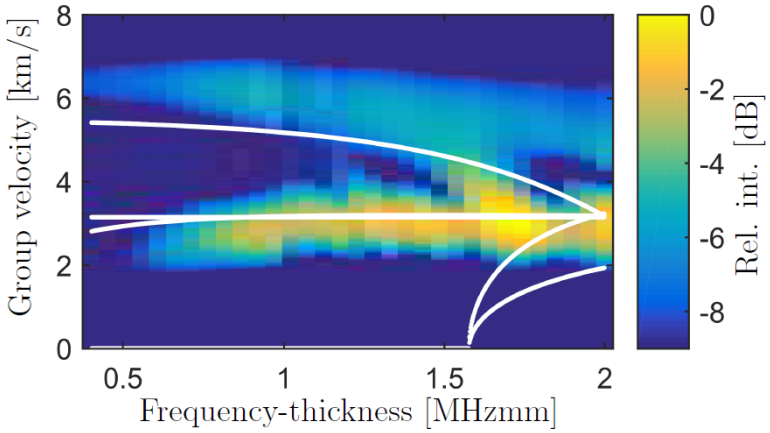

Figure 4.20: The group velocity of the leaking modes for different thicknesses (since frequency is constant). There is a small difference between the measured results and the modelled data, which are shown in white.

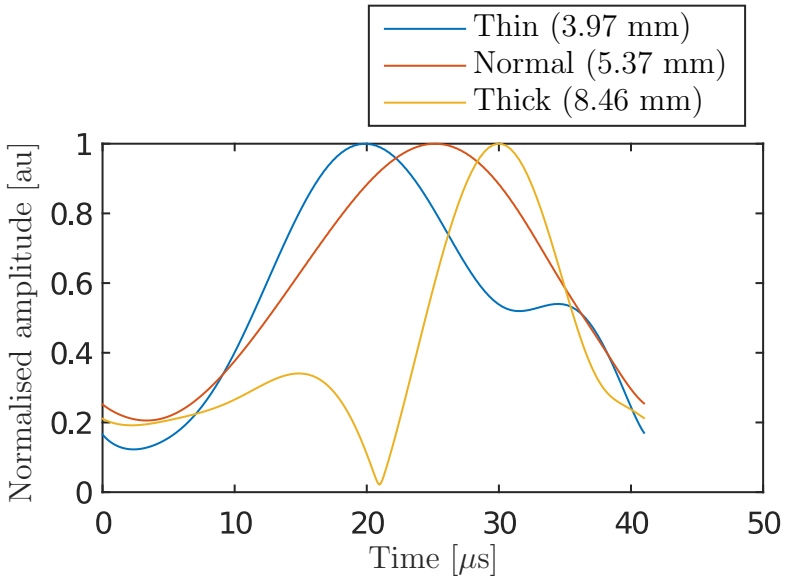

Figure 4.21: The envelopes of guided waves leaking from the simulated skull for each thickness. The signals indicate that the group velocity changes as the skull thickness does.

distance between the waveguide and the transducer is fixed a later arrival in the envelope is indicative of a reduction in group velocity. Just as with the aluminium cylinders, as thickness increases so does the time of arrival (a reduction in velocity).

4.6 Discussion

4.6.1 Performance of PSAM

When the algorithm was applied to ex vivo bone, the improvements were not profound like those in the simulation results. In this instance, the reverse was true and the FFT appeared had better performance as there was resolve of more modes. However the correctness cannot be fully verified because the exact bone dimensions and properties were unknown, and so the fit was only estimated. Despite the high element count of the receiving transducer, the results have a poor SNR and the low number of dected modes demonstrate the need for bespoke systems like AZA and EVA. Another cause of the poor SNR was the high frequency-thickness of the experiment.

For the in vivo experiments, the agreement between the experimental data and the models is good, but this may be due to the large size of the EVA time-space space matrix afforded by the sparse array technique used. The most obvious issue with the PSAM technique in the results is the addition of strong subharmonic frequency components. However, as with the simulation results, the components could be easily separated in the frequency domain and have no influence on the identification of the modes. It is possible that these harmonics are the result of the multiplication step used in the algorithm. PSAM does have reduced spectral leakage and appears to excel in separating closely spaced modes. The areas of sensitivity are small however and may be as a result of the highly nonlinear[1] nature of multiplication based beamformers; strong correlations in signals appear much more profound than they would with a linear beamformer like DAS. Just as with simulation there is also improved detection of the higher order modes. The overall contrast was improved with PSAM.

4.6.2 Validity of Skull-borne GWs as a Therapy Guide

For GW to be useful as therapy guide it must be possible to do the reverse of what has been demonstrated, i.e., predict the skull thickness or other parameters from measurements. There may be multiple ways to do this including sonicating the skull with several discrete frequencies. One technique proposed here is to give each thickness a unique signature based on the difference between the two mode velocities. Figure 4.22 shows the group velocity of the two modes across the thickness range 5 to 7.5 mm (1 to 1.5 mmMHz) from figure 4.20. The values were found from the locations of the wave packet maxima.

The major mode refers to the higher amplitude wave packet which is likely F(1, 1) while the minor mode refers to F(1, 2). To give each thickness a signature the two velocities were subtracted to produce the orange line. From this line it can be seen that each thickness has a unique value which could be used to estimate thickness from GW measurements. As the thickness increases, the velocity difference reduces. At 7 mm, the value increases slightly, but may be

[1] As in nonlinear function. Unlike sum based beamformers which are commonly referred to as being linear.

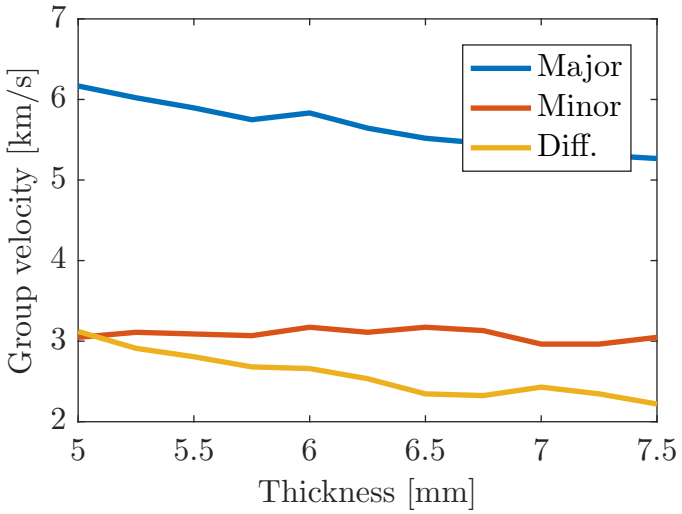

Figure 4.22: Difference in wave packet velocities in the thickness range 5 - 7.5 mm from figure 4.20. The major (blue) velocity is the slower, high amplitude packet and minor is the faster, but lower amplitude packet. The difference between the two is shown in orange.

as a result of an incorrect wave packet maxima location. There is a discernable difference in the value between the intervals considered, so it can be deduced that the thickness measurement accuracy is < 0.25 mm.

Returning to figure 4.20, there is some disagreement between the simulation and theoretical results, particularly for the mode $\mathrm{F}(1,2)$, which is likely the result of fluid loading. A full study into the effects of fluid loading on the waveguide is beyond the scope of this chapter, but it is expected the wave shapes of the excited modes mean that they are susceptible to changes in velocity. Figure 4.23 shows the wave shapes for both modes at the two different frequency-thickness products. The waves propagate in three dimensions at all times, circumferentially (θ), radially (r) and along the cylinders axis (z). The shapes are presented as displacement along the radius of the cylinder. The wave shape's amplitudes are normalised so they can be easily compared with each dimension. By comparing the amplitude of the shape in each dimension it is possible to determine where most of the displacement exists at a given operating point. It can be seen that mode $\mathrm{F}(1,2)$ has low radial and circumferential displacements which will likely change the velocity of these modes as

they propagate through a fluid [84].

With regards to the skull models, figure 4.8 should again be considered. At the fd operating points considered, a reduction in the speed of the fastest mode F$(1,3)$ was expected with these experimental parameters and was observed. Therefore, the results show that it is possible to excite guided waves in a three-layered skull model using the unconventional geometry. It was also shown that the nominal thickness has an impact on the velocity of these guided waves.

A number of simplifications were made in the modelling, however. Firstly, a cross section of skull was modelled instead of a full 3D model, which reduced the number of computational elements by a factor of 1520. This compromise is permissible though as this work concerned itself primarily with the challenge of exciting guided waves in a curved skull model with a concave transducer. Further modelling should be conducted to determine the influence of the skull shape and artefacts on measurements.

With respect to array modelling, 128 elements were used, which is perhaps denser than what would be available in clinical systems, where only 1024 elements are used to cover the whole skull [187]. To aid simulation performance, frequencies lower than what is clinically available were used. Experimentally, increasing the excitation frequency and reducing the element density will induce grating and side lobes. It will also mean that the generated plane wave would need more distance to form. Experiments in ex vivo skull (not shown) showed that the angle of incidence did not influence guided wave propagation as it typically would in normal waveguides. Therefore the small distance should not have much impact, as only the part of the wavefront at the correct angle will convert into guided waves anyway.

Further mathematical analysis should be conducted with respect to mode propagation. The influence of overall speed of sound with respect to individual layers should be considered. Dispersion curves for a fluid-loaded 3 layer skull should also be calculated. This would allow a measured arrival time to be converted to specific layer properties. Algorithmic approaches for converting these observations into exact quantified are also needed. Least squares algorithms and neural networks may prove useful here.

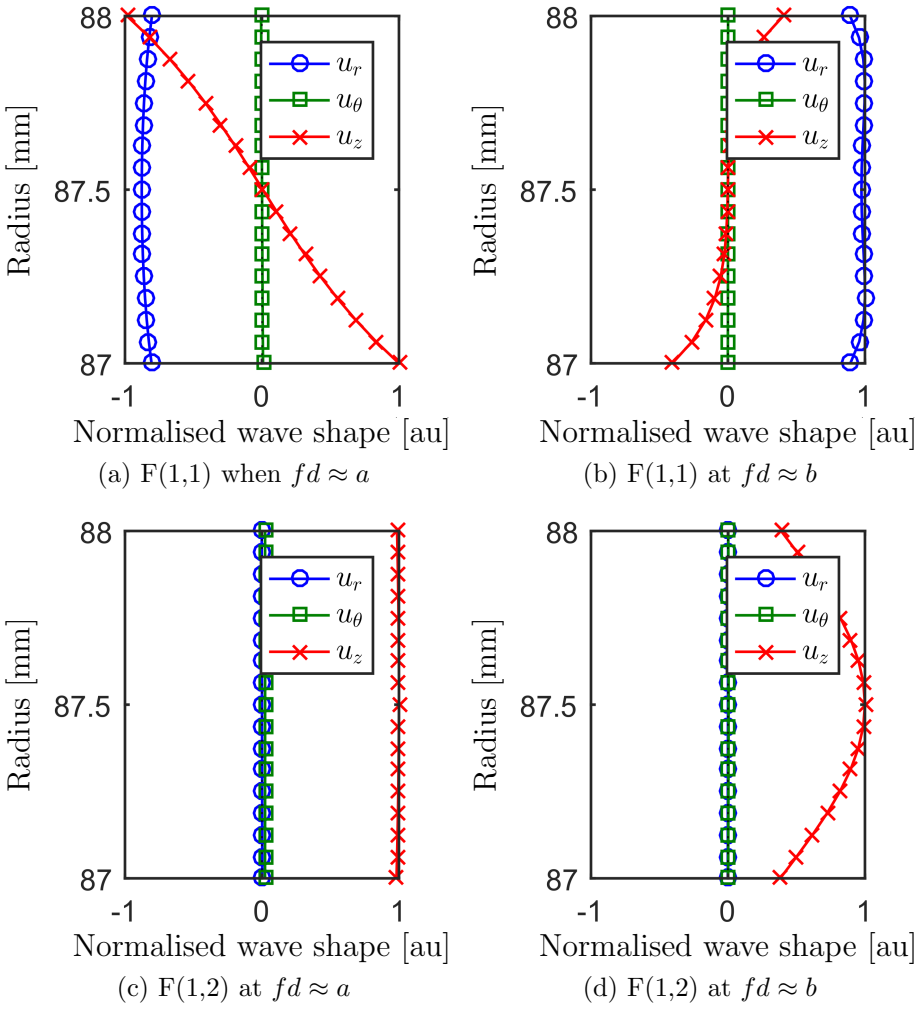

(a) F(1,1) when $fd \approx a$

(b) F(1,1) at $fd \approx b$

(c) F(1,2) at $fd \approx a$

(d) F(1,2) at $fd \approx b$

Figure 4.23: Wave shapes for different frequencies and modes in aluminium. The wave shape changes according to frequency and mode. u_r is displacement in the radius, u_z is displacement along the length of the cylinder, u_θ is displacement in the circumference

4.6.3 Prospects

Both of the presented schemes would likely benefit from signal processing development. For the long bone experiments, SVD, which has been shown to greatly improve the SNR of GW bone measurements, should be applied in conjunction with the PSAM algorithm. The skull experiments could also greatly benefit from the application of SVD. By making multiple observations around the array, SVD could be used to extract the guided waves from the signals that are superimposed with the reflections, due to their differing velocity. This could improve the localisation of the technique as currently, signals are separated temporally which means chosen receiving elements must be some distance away from the transmitters to allow the faster waves to separate.

Furthermore, tomography could also be included to improve localisation. A full 3D implementation would allow plane waves to insonify the skull at numerous locations from multiple directions. Tomography could then be used to calculate a localised difference in skull properties. This could be used to generate a thorough map of thickness change that is co-located with the therapeutic array.

The PSAM algorithm suppressed the S_2 mode considerably, but this artefact of nonlinearity could be calibrated out in a way that would not impinge on the recovery of other modes. This is common practice with other nonlinear beamformers. The algorithm was shown to improve the contrast of the higher order modes in simulation, but the results did not translate as well to the in vivo and ex vivo experiments. This is because there is currently little experimental or theoretical data available on the higher order modes of bone. However, there is still a significant contribution with the presented PSAM technique. Until higher order mode data is known, which the PSAM technique could be used to characterise, other applications of PSAM such as NDT should be considered. In metal plate inspection for example, where the attenuation of these higher order modes is much lower, PSAM could be used to enhance their detection. Additionally, the algorithm is not limited to using multiplication; the phase shift step could be used to support other beamforming techniques, and researchers are invited to continue this investigation. Accordingly, the phase shift code has been provided in appendix B.

For the skull models, it was shown that the properties of the skull could be ascertained from guided wave measurements made using a phased array transducer in a concave configuration. Transcranial arrays will continue to increase in density making localised detection of skull properties more plausible. Currently, however, not enough is known about how these guided waves propagate around the complex multi-dimensional water-loaded structures, to draw exact properties from the measurements. So as with long bone, a more thorough theoretical understanding is required.

Even with the improvements to the signal processing, it seems it would be difficult to obtain phase aberration data at a resolution that could compete with existing CT methods. However, the measurement of attenuation which was not considered seems highly plausible. To the best of the author's knowledge, clinical transcranial systems do not currently compensate for varying attenuation in the skull. This information cannot be obtained from a CT scan or from pulse-echo measurement, but could from GW measurements.

4.7 Conclusions

The behaviour of guided waves in bone is sensitive to a number of mechanical properties of the bone waveguide. Two potential applications were presented here: Osteoporosis assessment, and skull measurement for transcranial therapy. For the former, the understanding of cortical guided waves continues to improve, but obtaining accurate dispersion curves from a small, highly attenuating area of the skeleton remains challenging. For skull measurement, any data obtained needs to be co-registered with the therapeutic array to be useful. This also poses challenges because of the unusual geometry.

For long bones, a signal processing technique was designed to remove dispersion from the bone, achieving temporal alignment of multiple transverse observations of the highly dispersive waves. This allowed beamforming techniques to be used to highlight the existence of certain modes that align at a given phase velocity. Multiplication was used and it was found in simulation that this was effective at highlighting particularly high-order modes, although it did introduce low-frequency noise. Experimentally, it was found that the

spectral leakage was lower than with currently used techniques to measure phase velocity along with improved sensitivity to high order modes again.

Further work is required to remove the introduction of the low-frequency noise and to apply SVD which may be used to achieve the high-quality curves necessary for model fitting. Unfortunately, the high order modes are highly attenuated and not properly understood in bone, so the technique may be more useful in other fields such as NDT which will be explored in the future.

For the skull aspect of the investigation, a scheme for generating guided waves in skull was described. To test it, simplified skulls were modelled using finite element analysis. The proposed technique involved selecting an area of skull to be inspected and choosing a number of elements from a typical transcranial array to achieve the required angle of incidence tangential to the skull. For each element in the array, delays were applied to a wavelet excitation to produce an angled plane wave. The obliquely incident waves interacted with the skull to produce guided waves.

To separate the guided waves from reflected spectra, temporal windowing was used, followed by a Hilbert transform to estimate the group velocity. A number of different thickness aluminium models were considered along with 3 thicknesses of skull. Measurements from the aluminium models were compared with theoretical dispersion curves and exhibited the expected behaviour with respect to changes in velocity. However, there was some disagreement in the exact value, likely due to the effects of water loading which was not considered. In skull, a decrease in velocity with an increase in thickness was observed which was also expected. Further efforts should be focused on; signal processing to improve localisation, and experimental work to better understand the effects of fluid loading and to select more appropriate modes. The modelling should also be extended to consider attenuation, as localisation of absorption differences cannot be achieved with existing CT technology, and the requirements for localisation are much lower than for thickness.

Overall, this chapter has shown that guided waves have numerous biomedical applications. The bespoke research platforms used here (AZA/EVA/UARP) provide access to the raw, un-beamformed, data and precise control of the transmission sequencing, which has promoted the development of two novel GW induction and observation methods tailored for bone. Both schemes of

work could be eventually integrated into commercial systems, to fulfil currently unmet clinical needs.

Chapter 5

HIFU Drive System Miniaturisation Using Harmonic Reduced Pulse Width Modulation

Switched excitation has the potential to improve on the cost, efficiency and size of the linear amplifier circuitry currently used in HIFU systems. Existing switching schemes are impaired by high harmonic distortion or lack array apodisation capability, so require adjustable supplies and/or large power filters to be useful. A multi-level PWM topology could address both of these issues but the switching-speed limitations of transistors mean that there are a limited number of pulses available in each waveform cycle. In this study, harmonic reduction pulse width modulation (HRPWM) is proposed as an algorithmic solution to the design of switched waveforms. Its appropriateness for HIFU was assessed by design of a high power 5 level unfiltered amplifier and subsequent thermal-only lesioning of ex vivo chicken breast. Three switched waveforms of different electrical powers (16, 26, 35 W) were generated using the HRPWM algorithm. Lesion sizes were measured and compared with those made at the same electrical power using a linear amplifier and bi-level excitation. HRPWM produced symmetric, thermal-only lesions that were the same size as their linear amplifier equivalents ($p > 0.05$). At 16 W, bi-level excit-

ation produced smaller lesions but at higher power levels large transients in the acoustic waveform nucleated undesired cavitation. These results demonstrate that HRPWM can minimise HIFU drive circuity size without the need for filters to remove harmonics or adjustable power supplies to achieve array apodisation.

5.1 Introduction

High intensity focused ultrasound (HIFU) is a non-invasive surgical technique that is used to generate coagulative necrosis in tissue through localised thermal ablation [188], [189] and other mechanical effects [190], [191].

The main application areas of HIFU are the treatment of soft tissue tumours [192], [193] in liver [194], kidney [154], prostate [195], [196], breast [197] and in the brain [198], [199]. HIFU is not limited to the treatment of soft tissue tumours, and exploration of new avenues such as triggered drug delivery [200], treatment of bone tumours [201], neurological disorders [202], ectopic implantation [203] and pain management [155], [204] continues.

Single element transducers with a fixed focus have traditionally been used to achieve the desired intensities for ablation [205]. Recently though, high power therapeutic arrays are increasingly used [153] as they can facilitate dynamic focal position for hyperthermia [206], [207] and ablation[1]. Large arrays on the order of 1000 elements are essential in transcranial therapy to spread the acoustic heating in the skull [208], [209]. Since the attenuation and phase aberrations induced by the skull vary considerably across its surface [210], [211], the phase and amplitude of the excitation waveform of each element must be adjusted [159], [164], [165]. Other uses of array transducers include rib sparing in the treatment of liver [42], [212], [213], volumetric treatment of uterine fibroids [214] and surgery on the prostate [215]. Whilst the ability to excite each element in the array with a different waveform is essential to transcranial therapy, it is also highly desirable in other applications as it facilitates array

[1] F. Xiaobing and H. Kullervo, 'Control of the necrosed tissue volume during noninvasive ultrasound surgery using a 16-element phased array', *Medical Physics*, vol. 22, no. 3, pp. 297–306, DOI: 10.1118/1.597603. eprint: https://aapm.onlinelibrary.wiley.com/doi/pdf/10.1118/1.597603.

apodisation which reduces side lobes, linear frequency modulation to reduce grating lobe energy [39], phase shift keying [216] to suppress standing waves and beam steering [217].

In HIFU systems each array element is typically connected to a linear power amplifier so that the system can deliver the high electrical powers (> 15 W) necessary for tissue ablation. Each amplifier is in turn connected to its own waveform generator to achieve the necessary phase and amplitude control. This arrangement has low harmonic distortion, meaning that the electrical waveform does not contain undesired harmonics of the fundamental component. Whilst this is desirable, there are a number of disadvantages including high cost, low efficiency and large size [27]. This is increasingly problematic as higher density arrays continue to be developed. Additionally, the large numbers of passive components which are prevalent in these designs limit their usefulness for catheters and in MRI environments [30]. For HIFU array treatments to be more financially and practically accessible, improvements should be made to the driving circuitry [27].

In this thesis, a harmonic reduction pulse width modulation (HRPWM) amplifier is proposed to reduce the size and cost of the excitation circuitry currently used in HIFU array systems. Comparisons will be made with existing excitation techniques numerically and experimentally.

5.2 Switching Schemes and Amplifier Design

As discussed in chapter 2, switched mode circuits have numerous advantages over linear amplifier designs [29], [30]. Unlike linear amplifiers, the input of each transducer element is connected to transistors that rapidly switch between a discrete number of voltage levels to approximate the desired waveform. Operating the transistors in their saturated region increases the efficiency but may produce powerful third and fifth harmonics in the electrical waveform [32]. For example, when a simple bi-level excitation is used, the third and fifth harmonics are only 10 dB and 15 dB less powerful than the fundamental component. These harmonics can be within the bandwidth of HIFU transducers which are highly resonant devices that produce acoustic energy at their harmonics [218],

[219]. These harmonics could cause unwanted effects [220], such as disruption of the focal region [30], heating of the transducer [221] and the generation of grating lobes [1].

5.2.1 Switching Schemes

A number of switching schemes have been proposed as an alternative to linear amplifiers. Bi-level has been shown to minimise the footprint of driving electronics and improve efficiency. Amplitude control can also be achieved by adjusting the duty cycle [222], but this regime still requires additional fixed-frequency filtering components in the circuit design to remove harmonics. These filters are large, MRI incompatible [223] and limit the use of frequency modulated waveforms.

Tang & Clement demonstrated that introducing a predetermined off period between the two levels can be used to disrupt the periodicity of the third harmonic[1]. This has been implemented in an MRI compatible catheter system [224]. Alternatively, additional levels can be introduced to the circuit to implement staircase converters. This naturally disrupts the generation of harmonics [225] and several authors have demonstrated harmonic reduction this way at ever increasing frequencies and powers [221], [226]. However, the constraints placed on the waveform with these techniques mean that each array element would require its own adjustable supply to achieve apodisation which is costly and cumbersome.

Amplitude control in a switched system can be achieved using PWM and has been successfully applied to ultrasonic imaging [21]. Here the circuitry is continually switched at a higher rate than the frequency response of its load. The load acts as a bandpass filter causing averaging of the drive voltage across one switching period. The pulse width is then modulated to achieve the desired instantaneous amplitude. It is possible to drive a HIFU transducer with PWM, but the combination of high power and frequency, mean that a limited number of pulses per waveform are available, and thus amplitude control may not be

[1]S. C. Tang and G. T. Clement, 'A harmonic cancellation technique for an ultrasound transducer excited by a switched-mode power converter', in *Ultrasonics Symposium, 2008. IUS 2008. IEEE*, IEEE, 2008, pp. 2076–2079.

reliable.

HRPWM is a five-level PWM scheme with carriers algorithmically designed specifically to reduce the number of pulses in each cycle whilst retaining amplitude control and actively implementing harmonic reduction [227]. It has facilitated a number of medical imaging and NDT applications [3], [22], [228], but this study is the first time it has been used for HIFU.

5.2.2 Circuit Operation

Previous publications on HRPWM have utilised 5-level integrated pulser ICs to excite the transducer. These integrated devices have limited total continuous power ratings, so are not suitable for the continuous wave (CW) operation necessary for HIFU. For this study, a purpose built 5-level pulser bridge circuit was designed using discrete components to facilitate high power CW operation.

Figure 5.1 shows the structure of one bridge of the pulser. Each pulser is made up of three identical bridges, providing $\pm V_1$, $\pm V_2$ and GND rails. The full schematic and printed circuit board (PCB) design have been made available online [8]. Each bridge consists of two capacitive level shifter circuits, an NMOS power transistor for the negative rail, a pair of PMOS transistors for the positive rail, and two pairs of diodes to prevent the MOSFET body diodes becoming forward biased. Two PMOS transistors are used in parallel as the series resistance of each PMOS device is about twice that of the NMOS transistors. The pulser is controlled by driving the six MOSFET gates, two per bridge. The PMOS transistors are controlled by the active low signals $\overline{A_0}$, $\overline{A_{1+}}$ and $\overline{A_{2+}}$ where a 0 V pulse will turn the MOSFET on, and +12 V will turn it off. For each NMOS transistor, a +12 V pulse on the active high control signals A_0, A_{1-} and A_{2-} will turn it on, and 0 V will switch it off. These control signals require relatively high switching currents due to the large capacitance of the MOSFET gates, and as such are driven using MOSFET drivers (Analog Devices ADP3654) with current limiting resistors. As the gates are referenced to high voltage power supplies ($V_n \approx 30$ V), capacitive level shifters are used to isolate the gates from the control circuitry. The level shifters use series capacitors that are biased to the supply voltages via a combination of a parallel

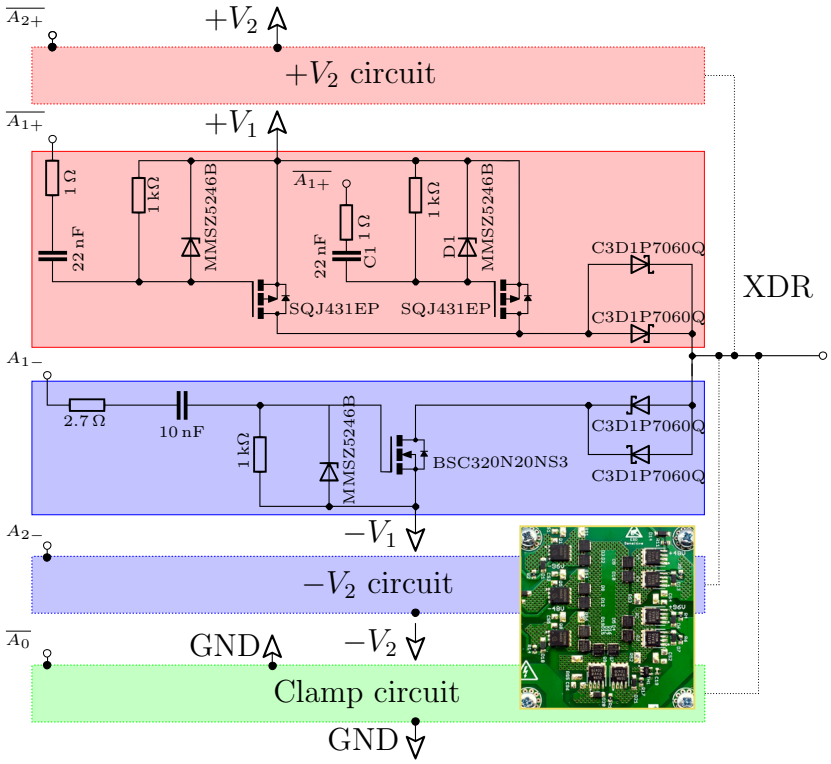

Figure 5.1: Part of the circuit design used in this study [8]. The red areas represent components used for positive levels, whilst blue represents areas used for negative and green for ground (clamp). The circuit output is connected to the transducer element without filters. Inset: The active area of a fabricated card which consumes approximately 25 cm^2 of space

resistor and Zener diode. When the high voltage power supplies are turned on the capacitors will rapidly charge up to the supply voltage through the Zener diode, which protects the gates. When the input control signal side of the capacitor is driven to "On" (+12 V for NMOS, 0 V for PMOS), this change in voltage will be reflected as an equal change at the gate, becoming $-V_n + 12$ V and $+V_n - 12$ V for NMOS and PMOS respectively. Similarly, when the control signal is driven to "Off", the gate side of the capacitors will return to the supply voltage $\pm V_n$. Due to the bleed resistor in the level shifter, the $\overline{A_{1+}}$, $\overline{A_{2+}}$, A_{1-} and A_{2-} control signals cannot be driven to "On" indefinitely, being limited to approximately 1 ms on-time. This is not an issue for ultrasound applications as each gate is typically turned on for less than a microsecond. The pulser circuit was fabricated on a PCB, with an active area of approximately 25 cm^2 as shown inset in figure 5.1. Sixteen channels of the drive circuit were connected to an FPGA development card (5SGSMD5N, Altera, USA). The transmit waveforms were then designed using MATLAB (Mathworks, USA) and uploaded via PCI Express to the FPGA. Each channel could be operated individually with up to 41W output power for 30 seconds of CW, or combined in parallel for higher output powers.

5.3 Numerical Study: Effect of Harmonic Distortion on Lesioning

Numerical simulations were undertaken to assess the effect of harmonic distortion from switched excitation on lesion formation. The simulation considered a single element transducer where amplitude control can be achieved by adjusting the power supply. This allows the effects of harmonic distortion to be isolated from any amplitude control capabilities that are necessary for array systems.

2D simulations were performed in the pseudo-spectral simulation package k-wave [229]. A typical concave HIFU transducer with a diameter of 64 mm, a natural focus of 63 mm and a centre frequency of 1.1 MHz was simulated. The transducer transfer function consisted of a low pass, 50 order FIR filter that rejected energy at harmonic four and above. The element size in simulation

was 112 µm and had 646×531 elements of which 20 in each dimension formed the absorbing boundaries, leading to a total area of 64 mm $\times$ 78 mm.

Bi-level and HRPWM excitation schemes were considered in conjunction with a linear amplifier. A 50% duty cycle square wave was used for the simplest of the switched schemes, bi-level excitation. For HRPWM, transitions to each level are set to achieve the desired magnitude of the fundamental component whilst ensuring that any switching-induced harmonics destructively interfere. Pertinent to the algorithm is that its carriers can change in frequency and phase, allowing the waveforms to be designed to give only one or two pulses per half cycle. This ensures robust control of amplitude and thus acoustic intensity using a minimal number of switching events. The acoustic wattage produced by the transducer was maintained between schemes. This allowed the effects of harmonic distortion in the presence of tissue to be assessed. To this end, the virtual power supply of each of the schemes was adjusted so that when the transducer transfer function was applied they all produced 26 W of acoustic power. In addition to control by supply rails, the HRPWM scheme is also able to modulate its own amplitude so it was arbitrarily set to produce waveforms at 70% duty cycle prior to adjustment of the power supply. Figure 5.2 shows bi-level and HRPWM schemes in the frequency and time domains. The two example excitations are compared with a perfect sinusoidal excitation by a linear amplifier which is shown in grey. Three cycles of the excitations are shown. In the frequency domain, the highest 20 dB of normalised amplitude is shown across the frequency response of the transducer. The location of the second and third harmonics of the transducer, where the electrical conversion efficiency is highest, are indicated by the lines f_2 and f_3. Below 20 dB, any energy is considered irrelevant. Neither the sinusoidal or HRPWM excitation has observable frequency content outside the fundamental component. The bi-level scheme has harmonic distortion at f_3, that could be converted into acoustic energy. The transducer was placed in water and a 45 mm thick medium that best represented chicken muscle [51], [230] was placed at the transducer's focal point. The medium's acoustic and thermal parameters are presented in table 5.1.

Nyborg's heating equation [231] was modified to calculate the total heat

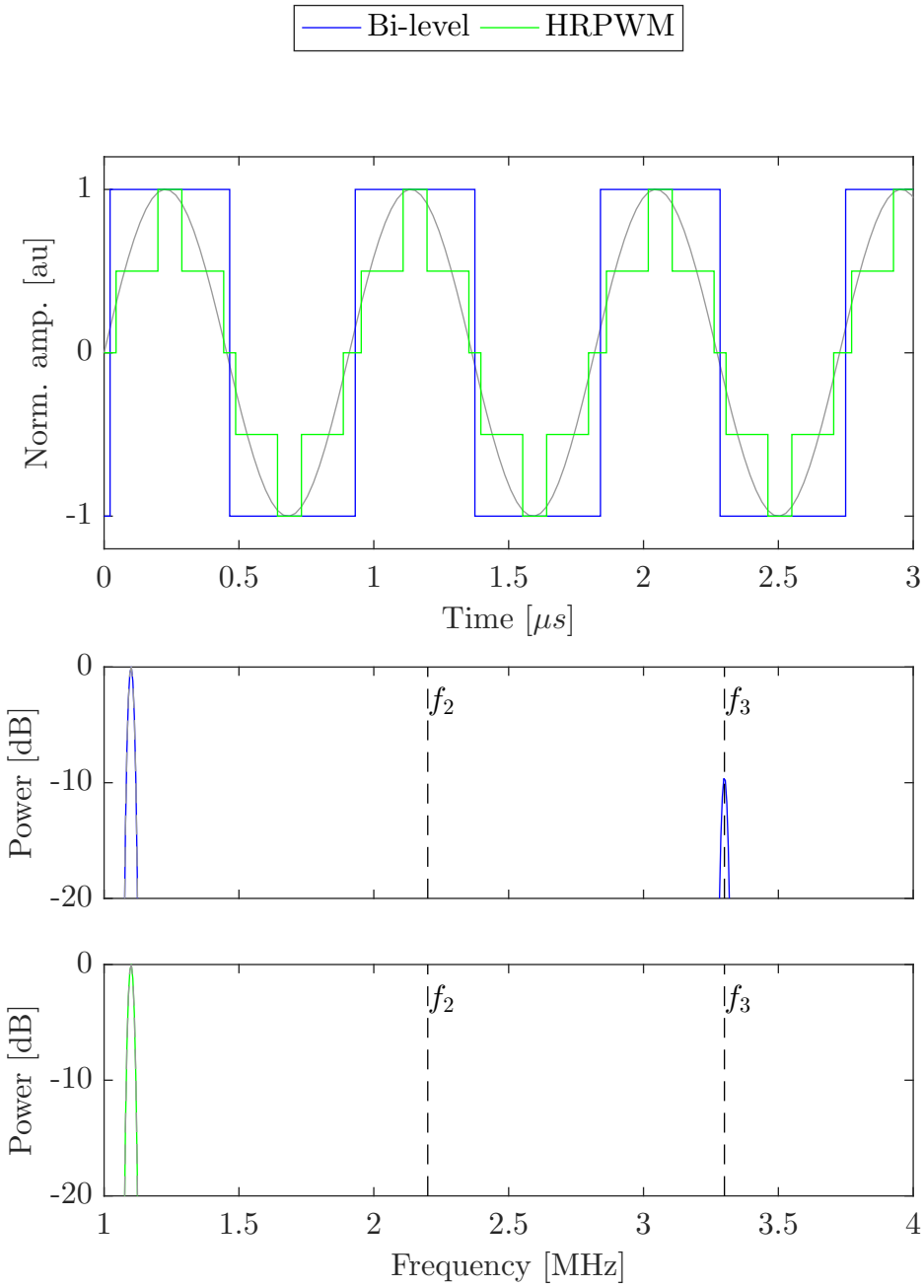

Figure 5.2: Time and frequency domain plots of the 1.1 MHz bi-level and HRPWM excitations used in simulation. Ideal linear amplifier results are shown in grey for comparison. The second and third harmonics of the transducer are indicated by the black lines f_2 and f_3.

Table 5.1: Medium properties used for modelling

Property	Symbol	Value
Speed of sound	c	$1520\,\mathrm{m\,s^{-1}}$
Density	ρ	$1020\,\mathrm{kg\,m^{-3}}$
Thermal conductivity	Λ	$0.5\,\mathrm{W\,m^{-1}\,K}$
Specific heat	C	$3600\,\mathrm{J\,kg^{-1}\,K}$
Ambient temperature	T_0	$37\,^{\circ}\mathrm{C}$
Attenuation	α	$1.1\,\mathrm{dB/MHz^{1.5}cm}$
Parameter of nonlinearity	(B/A)	6.4

generation by the ultrasound at the first 6 harmonics:

$$Q = \sum_{h=1}^{h=6} \alpha_h p_h^2 / \rho c \tag{5.1}$$

Where p_h and α_h refer to the magnitude of the pressure and absorption at harmonic h. Pennes' bioheat transfer equation [232] was then used to calculate the temperature rise in the medium for each exposure made with each scheme. Exposures were made for 20 s before cooling for a further 10 s, to account for perfusion. The starting temperature was 37 °C. From the thermal exposures, CEM43 was calculated [233]. A lesion map was then created from the area of tissue where CEM43 exceeded 240 minutes, which is the default value for the simulation package and also the reported damage threshold for prostate tissue [234]

5.4 Experimental Study: Lesion Volume Control with PWM

A key advantage of the HRPWM scheme is the ability to apodise arrays without the need for independently adjustable power supplies or external filters. It is essential that this apodisation can occur at electrical powers relevant for HIFU therapy. In this part of the study, assessment of the scheme's amplitude control capability was made by comparing lesioning efficacy with a linear amplifier. A reduction in amplitude should reduce the lesion volume and vice

versa. Additional comparisons were made with bi-level excitation. The aims of the experimental study were to both augment the simulation results and to assess the capability of HRPWM to control acoustic intensity and duration at lesioning levels.

For the linear amplifier experiments a signal generator (33600A, Agilent, USA) was connected to 45 dB linear power amplifier (A150, E&I Ltd, USA) (figure 5.3).

5.4.1 Sample Preparation, Lesioning and Analysis

Ex vivo chicken breast was used for the lesioning study. Fresh chicken breasts were lesioned within 18 hours of purchase and were refrigerated at 4 °C when not used. The tissue was cut into cubes approximately 55 mm × 55 mm × 40 mm. The samples were then degassed in a 1% (v/v) phosphate buffer solution for 4 hours. To ensure repeatability between samples, they were placed in a holder marginally smaller than their cut size so that they were slightly compressed in all directions. The sample holder had acoustic windows on opposite sides of approximately 50 mm × 50 mm (figure 5.3).

Lesioning was performed with a single element focused HIFU transducer (H-102, Sonic Concepts, USA) in conjunction with the manufacturer provided impedance matching network, although it contained no frequency-filtering components. The transducer had a centre frequency of 1.1 MHz, a focal distance of approximately 63 mm and a diameter of 64 mm. The -6 dB beamwidth size data was obtained from the datasheet and is 1.33 mm in diameter and 10 mm long. To co-locate the centres of the transducer focus and the samples, an alignment target was temporarily attached to the inside of the sample holder, prior to the start of the first exposure. Using a hydrophone (Y-107, Sonic Concepts, USA) co-located and confocal with the centre of the HIFU transducer, the transducer was pulse-echo aligned onto the target. The sample holder was attached to a CNC machine stage which was programmed to move to 5 fixed locations spaced 20 mm apart. This meant that the 5 lesions were always made in the same places and at a fixed depth of 20 mm in each sample. Sonications were performed in a tank of degassed, deionised water which was maintained at 28 ± 1 °C using an immersion circulator. This temperature was chosen to be

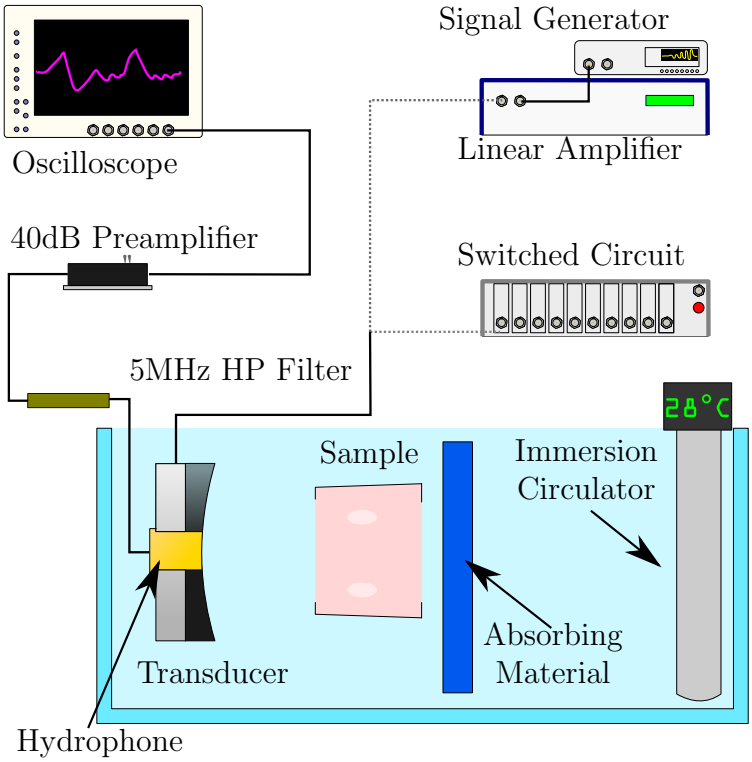

Figure 5.3: Schematic of the experimental apparatus used in this study. Not shown: current probe, matching network, CNC machine

representative of in vivo tissue without causing premature denaturing of the sample.

To attenuate post-focal energy and prevent reflections, 10 mm of absorbing material was placed behind the samples. This arrangement is depicted in figure 5.3. The samples were sonicated for 20 s. Between exposures, the tissue was allowed to cool for 10 s, to allow the bulk temperature of the tissue to return to ambient. Immediately after all the exposures were complete, samples were sliced through the centre of the lesions, revealing two halves of each lesion. Photographs of each lesion were taken next to a ruler and an identifying code. Using image analysis software (ImageJ, National Institutes for Health, USA), the pixel/size ratio was calculated and then the lesion cross-section area was measured using an ellipse area tool.

For the lesioning efficacy of different excitation schemes to be compared, the aim was to ensure that damage to the tissue was predominantly thermal

in nature and not from mechanical effects such as acoustic cavitation and/or boiling [235]. Three measures were taken to ensure that mechanical damage was reduced. Firstly, a passive cavitation detection (PCD) system was used [235]. Secondly, exposure times and intensities within the limits of previously published lesioning work (in chicken breast) were used [236]. Thirdly, lesions were inspected for unusual shapes that may suggest boiling.

For the PCD system the hydrophone was connected to an 11-bit oscilloscope (MSO-5104A, Agilent, USA) via a 5 MHz high pass filter (THP5P554100B, Allen Avionics, USA) and a 40 dB preamp (SPA1411, Spectrum, Germany). The high pass filter was used to remove any reflected energy from the HIFU transducer's first 3 harmonics and to avoid saturation of the oscilloscope's input. The oscilloscope was run in segmented mode and was set to record up to up to 256 waveforms of 250 µs length. The trigger threshold was set slightly above the noise level at 380 mV. The trigger hold-off was set to 50 ms so that data from up to 12.8 s of the exposure could be recorded. The number of triggers was recorded for each exposure, and if this number exceeded 10, the lesion was considered to be mechanically rather than thermally formed. Fourier analysis was performed on the recorded signals.

To ensure that each tissue sample was adequately degassed, prior to lesioning, a high amplitude 5 cycle pulse was applied to the transducer to discount the presence of bubbles. Additionally, every tissue sample contained at least one thermal-only lesion made using the linear amplifier.

5.4.2 Considered Schemes and Control of Acoustic Intensity

HRPWM, linear amplifier and bi-level schemes were used. Three different electrical powers for each scheme were considered: 16, 26 and 35 W. Using the beam width from the transducer datasheet and presuming an 80% efficiency, these electrical powers correspond to intensities of 1205, 1958 and 2637 W cm^{-2} respectively. Prior to ablations, with the transducer in-situ but samples removed, the circuit was adjusted to achieve the desired electrical power. For the linear amplifier experiments, the signal generator amplitude was adjusted. For the bi-level excitation, the supply voltage was adjusted but for HRPWM,

the power supplies were fixed and the amplitude modulation parameter was changed.

If knowledge of a transducer's complex impedance is known and a single drive frequency is used to excite the transducer, delivered true power can be controlled by changing the voltage of the waveform [237]. This approach is unsuitable here for two reasons, (1) the switched waveforms contain multiple frequency components that have differing corresponding impedances and (2) the output impedance of the switched circuitry is unknown and so there is potential for high levels of reflected energy.

Instead, a current probe (TM502A, Tektronix Inc., USA) and an oscilloscope (DS06014A, Agilent, USA) were used to measure the total delivered true power. The current probe was placed around the positive input of the matching network. Using a 100 cycle excitation, true power as a function of frequency was then calculated from the real product of the Fourier transformed voltage and conjugated current waveforms:

$$P(f) = Re(V(f) \times I(f)^*) \tag{5.2}$$

The total delivered power across a given frequency range was then calculated from the integral of $P(f)$:

$$P_T = \int_{f_0}^{f_1} P(f)df \tag{5.3}$$

For the experiments 500 kHz and 10 MHz were used for f_0 and f_1 respectively.

Since the electrical and acoustic configuration was consistent between schemes, it was presumed that the acoustic intensity remained the same irrespective of the scheme used. This power measurement approach was calibrated using a purely resistive 50 Ω load before the transducer was connected.

For each intensity and scheme, three lesions were made and measured, leading to a total of 27 exposures.

5.5 Results and Discussion

Figure 5.4 shows simulated lesioning under the three different excitation schemes. The acoustic field would propagate from left to right. The lesions are correctly shaped and axisymmetric although not rotationally symmetric. This is because of pre-focal lesioning due to non-linear propagation [16], [205]. The lesion cross-section areas and their percentage changes from the linear amplifier lesion are shown in table 5.2.

Ideally, each of the simulated schemes would have been calibrated to produce the same acoustic intensity at the focal region. This information cannot be obtained however prior to completion of a free field simulation. Authors have suggested previously that peak acoustic pressures might instead be appropriate to make comparisons between lesioning experiments [238]. However, this does not consider the increased energy that exists in the acoustic waveform when harmonics are introduced. For this reason, each scheme was calibrated using a fixed acoustic wattage at the surface. Despite this calibration, the schemes all produced different lesion sizes in simulation. When bi-level excitation was used, the lesions were smaller (-35%) compared with linear amplifier excitation. This is because more of the acoustic energy was distributed in harmonics and as the higher frequency components were more readily absorbed, less energy reached the focal region. When HRPWM excitation was used the lesion cross-section area was only slightly smaller (-12%) than the linear amplifier lesion. This is likely due to HRPWM having energy at higher order harmonics that are attenuated by the tissue.

The simulation results show that an increase in harmonic distortion of the excitation waveform reduces the lesion size (figure 5.4). The HRPWM scheme had the lowest harmonic distortion of the switched schemes and thus produced a lesion that was much closer in size to the linear amplifier case.

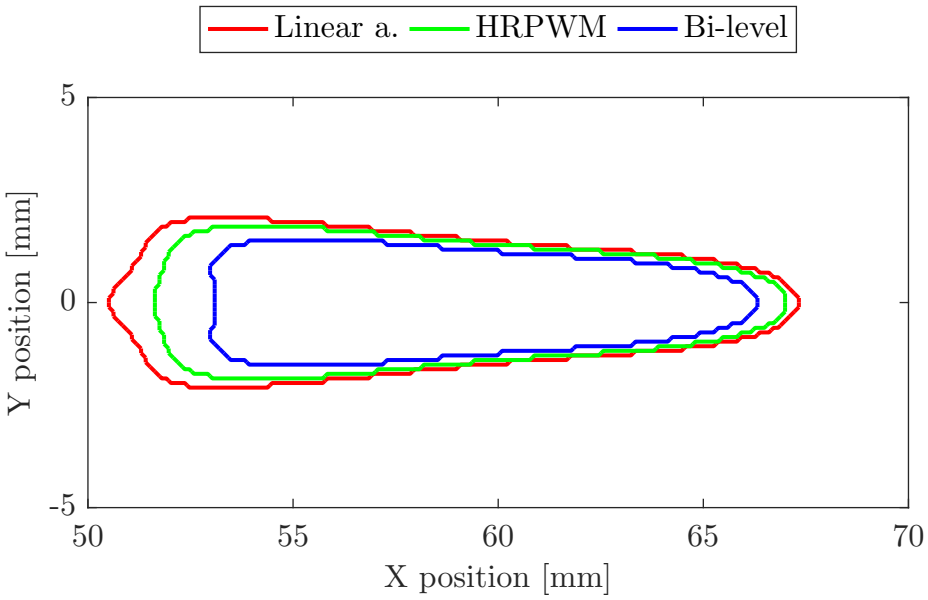

Figure 5.4: Simulated lesioning results. HRPWM and bi-level switched schemes were compared with excitation by a linear amplifier.

Figure 5.5 shows the experimentally obtained averaged lesion cross-section areas for different electrical powers using different excitation schemes. The error bars represent the standard deviation of three repeat measurements. The variance in mean lesion area between the linear amplifier and HRPWM was between +10% and -5%, whereas the variance was between -30% and -45% for the bi-level results. Each set of repeats were tested for normality using the Shapiro-Wilk test which is ideal for small sample sizes [239]. All set of repeats passed the test except for the lesions produced using 35 W bi-level excitation.

Table 5.2: Comparison of simulated lesion sizes with different excitation schemes

Excitation	Lesion Cross Section Area (mm^2)
Linear Amplifier (Ideal)	49
HRPWM	43 (-12%)
Bi-level	32 (-35%)

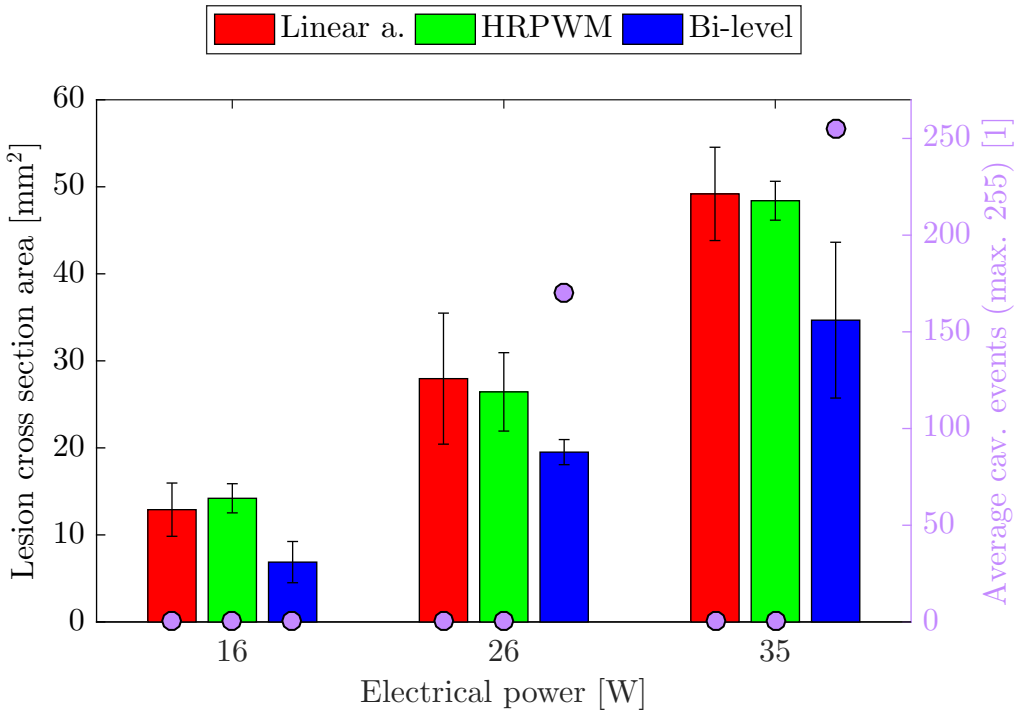

Figure 5.5: Lesion cross section areas at several electrical powers using different excitation schemes. Error bars are calculated from the standard deviation of 3 repeats at each scheme and power. The purple markers show the number of recorded cavitation events on average for each of the excitations.

Table 5.3: Statistical tests

Wattage (W)	Test	Value
16-35	Linear Amplifier	$p = 0.0006$
	Bipolar	$p = 0.0023$
	HRPWM	$p < 0.0001$
16	Lin. vs Bipolar	$p = 0.0543$
	Lin. vs HRPWM	$p = 0.5517$
26	Lin. vs Bipolar	$p = 0.1290$
	Lin. vs HRPWM	$p = 0.7788$
35	Lin. vs Bipolar	$p = 0.0737$
	Lin. vs HRPWM	$p = 0.8264$

Analysis of variance was then undertaken on the lesion cross-section areas to quantify their statistical significance. Tests were performed to assess two attributes, (1) similarity between schemes at the same power and (2) difference in lesion volume at different powers with fixed schemes. The tests and results are summarised in table 5.3. With HRPWM and the linear amplifier lesions, the analysis shows that a change in electrical power yields a change in lesion size ($p < 0.05$) and that the sizes are similar at each power level ($p > 0.05$). The same can be said when comparing the linear amplifier and bi-level lesions, although the size change is not as well discriminated and the difference in size at equivalent powers is more statistically significant ($0.8264 \gg 0.0737$ at 35 W).

As in simulation, with the 16 W bi-level excitation, there is a 47% reduction in the mean lesion area which is attributed to the absorption of harmonics. At the two higher powers however, the reduction in lesion volume is attributed to cavitation. This hypothesis can be confirmed in a number of ways. The average cavitation event count is shown in figure 5.5 by the purple markers is high (> 10) for the two high power bi-level exposures, while it is 0 for all other exposures. The lesion data from the 35 W bi-level excitation also failed a normality test which is indicative of the stochastic nature of cavitation. Mechanical damage is further evidenced by comparing the lesion shapes in figure 5.6. Here, all lesions were made using a fixed electrical power of 35 W but with different excitation schemes. Lesion (a) was made using a linear amplifier and lesion (b) was made using HRPWM. These two lesions are axisymmetric

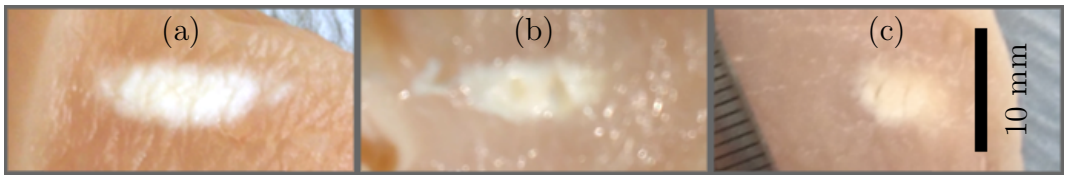

Figure 5.6: Lesions made using 35 W of electrical power. Lesion (a) was made using the linear amplifier, lesion (b) was made using HRPWM. Lesion (c) was made with bi-level excitation and was formed by mostly mechanical effects evidenced by a high number of triggers from the passive cavitation detector.

and ellipsoid in shape which is desirable. They show no evidence of boiling and have a similar cross-section area (a: 53.79 mm^2, b: 47.29 mm^2). Lesion (c) was mechanically-formed using bi-level excitation. The lesion is round instead of cigar-shaped, has a smaller area of 24.34 mm^2 and the cavitation count reached 255 (the maximum possible) during the exposure.

Example signals acquired from the PCD are shown in figure 5.7. The grey line shows an acquired signal during thermal-only lesioning using a 35 W linear amplifier excitation. The spectrum here indicates no cavitation activity. The blue line shows an increase in the noise floor and harmonic generation by the presence of bubbles. This cavitation signal was recorded during a 26 W bi-level exposure. The spectrum suggests stable rather than inertial cavitation. No ultraharmonics are visible, although this is not expected at pressures close to the cavitation threshold [240].

5.5.1 Suitability of HRPWM for Therapeutic Ultrasound

Figure 5.8 shows negative pressure beam plots made with the CNC stage and a 0.4 mm membrane hydrophone (D1064, Precicion Acoustics, UK). The step size was 0.5 mm and the peak negative pressure (PNP) was used as an intensity reference.

The acquired waveforms were deconvolved to compensate for the hydrophone response and then an FIR high-pass filter ($n = 50$, $f_c = 2$ MHz) was applied to separate the higher order harmonics from the waveform. Pressure plots 5.8 (a) and (c) were produced using the unfiltered waveform of bi-level and HRPWM excitations respectively. Plots (b) and (d) show the correspond-

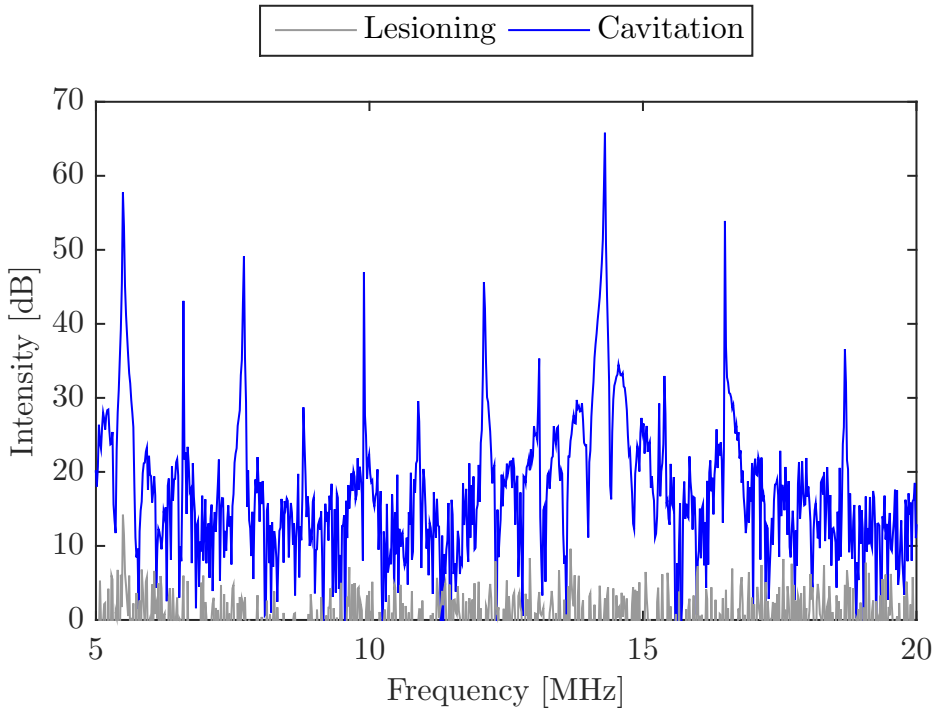

Figure 5.7: Examples of signals from the passive cavitation detector during lesioning. The grey line shows the PCD waveform during thermal-only lesioning with the linear amplifier. The blue line shows the PCD waveform from stable cavitation during a 26 W bi-level exposure. The reference value used for the intensity calculation is from the mean noise level.

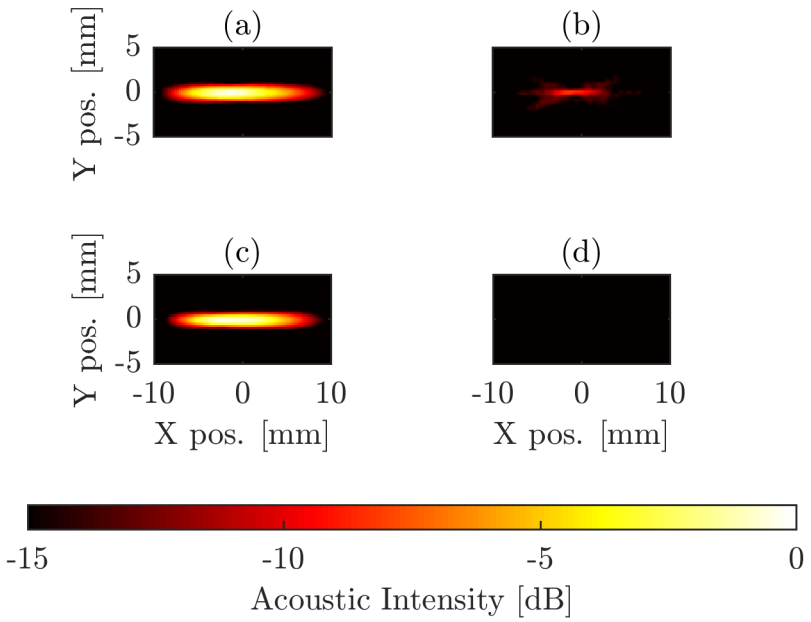

Figure 5.8: Pressure plots made with bi-level (a), HRPWM (c) and third harmonic only with bi-level (b) and HRPWM (d). For (a) and (c) only the highest 6 dB are shown.

ing plots when the fundamental component is removed. For (a) and (c) only the highest 6 dB are shown. The beam plots were made at sufficiently low pressures (< 1 MPa) to minimise the influence of non-linear propagation. Cubic interpolation was applied to the images so that a 1° rotation could be applied to correct for slight misalignment of the CNC machine and the acoustic path.

These results show that harmonic distortion in the bi-level electrical waveform can be observed in the acoustic domain. HRPWM was effective at reducing harmonic content in the waveform as no harmonics were visible above -15 dB. Since the magnitude of the harmonic components in the bi-level pressure plot and electrical waveform were equal (approximately -10 dB @ 3.3 MHz) this supports the model used in simulation that the transducer is almost equally efficacious at its fundamental component as it is at its third harmonic. This was further confirmed from a bandwidth measurement of the transducer (not shown).

The simulation and experimental parameters at 26 W were very similar although the higher ambient temperature used in the thermal simulations meant that simulated lesions were slightly larger. This was compounded by the fact that the simulation model presumed a 100% efficiency of the transducer, where experimentally only values of 80% have been reported [237]. The simulations showed that an increase in harmonic distortion in the excitation waveform can reduce lesion size for a fixed acoustic power. However, experimentally, a reduction in lesion size with HRPWM was not observed as it was in simulation. This is likely because the transducer is much more effective at attenuating harmonics than the FIR filter used in the simulation model.

Experimentally, additional undesirable mechanical effects were observed when using bi-level excitation. The authors believe the cause was the result of waveform shape rather than any inherent harmonic distortion. This suggests that a regular 5-level staircase circuit might suffice, although to the best of the author's knowledge no other appropriate pulse width modulation algorithm exists.

HRPWM's major advantage over other schemes however is its ability to apodise an array without the need for each element to have an independent power supply or filter. This makes it suitable for a number of high-density applications, catheters and MRI environments especially if combined with new

techniques to replace the matching network [241]. The experimental results show that this amplifier design and switching topology can control thermal dose at intensity levels useful in HIFU.

5.5.2 Cavitation Nucleation with Bi-level Excitation

It is expected that the reduction in lesion size with bi-level excitation would be more profound at higher depths as more acoustic energy would be absorbed before the focal region. To compensate, larger pressures could be used, but this is undesirable as it increases the likelihood of cavitation. It was not possible to generate thermal-only lesions using 35 W bi-level excitation. Cavitation activity was also observed during two of the three exposures at 26 W using bi-level excitation. To rule out possible error in power measurement, the acoustic intensity of the bi-level and linear amplifier schemes were compared at each power level. The -6 dB beam width was measured as 1.85 mm using the membrane hydrophone and the time-averaged acoustic power for each electrical power was measured with a radiation force balance (Precision Acoustics, UK) [242]. Due to the harmonic components having different focal positions, bi-level excitation distorted the focal region slightly, but it did not have any significance at the -6 dB threshold. At each power level, the intensities were found to be similar irrespective of the excitation scheme used. This means that the cavitation with bi-level excitation was not nucleated primarily through heating.

Experiments were repeated in an agar phantom to compare with chicken breast and it was found that cavitation was also observed using the 26W bi-level excitation, but not using the linear amplifier, even at higher intensities. The first cavitation event was temporally located at 85 µs after the start of firing, which is approximately twice the propagation time for the natural focal point of the transducer. This suggests that a transient near the start of the waveform was nucleating the cavitation.

Subsequent high resolution ($f_s = 200$ MHz) acoustic waveforms were captured using the membrane hydrophone at the focal point. It was observed that the pressure when using the linear amplifier increased slowly over the first 3 cycles but when using bi-level excitation, there were large negative transients.

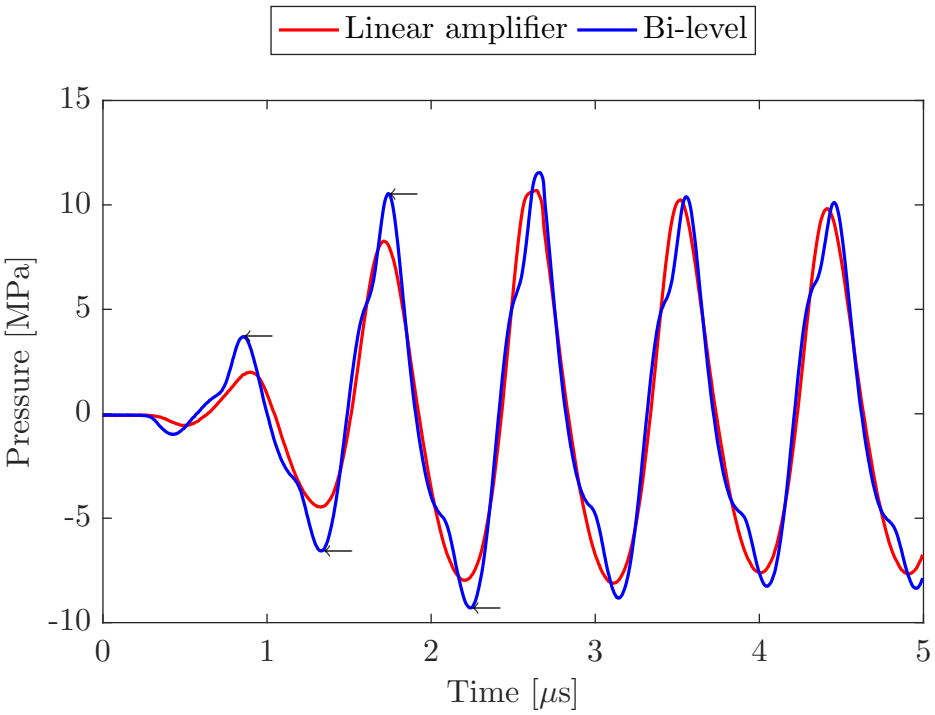

Figure 5.9: Acoustic pressure waveforms recorded near the hydrophone's saturation limit using the linear amplifier and bi-level excitation. The waveform made using bi-level excitation features large negative and positive (not shown) transients that are marked by arrows.

Examples of these transients are shown in figure 5.9. Here bi-level and linear amplifier excitations are shown at equivalent nominal pressures, however at the start, there are a number of transients that exceed this nominal pressure as indicated by the arrows.

Because of the saturation limit of the hydrophone, it was not possible to observe these transients with the highest power bi-level excitation. The values of these transients are shown alongside intensity measurements in figure 5.10. The error bars represent the minimum and maximum values of intensity caused by spatial averaging of the hydrophone and the purple line represent the suspected cavitation threshold.

A high PNP causes cavitation as the high negative pressure causes bubbles to form. The following positive pressure trasient then may instigate interial cavitation. Therefore cavitation nucleation could be attributed to the negative

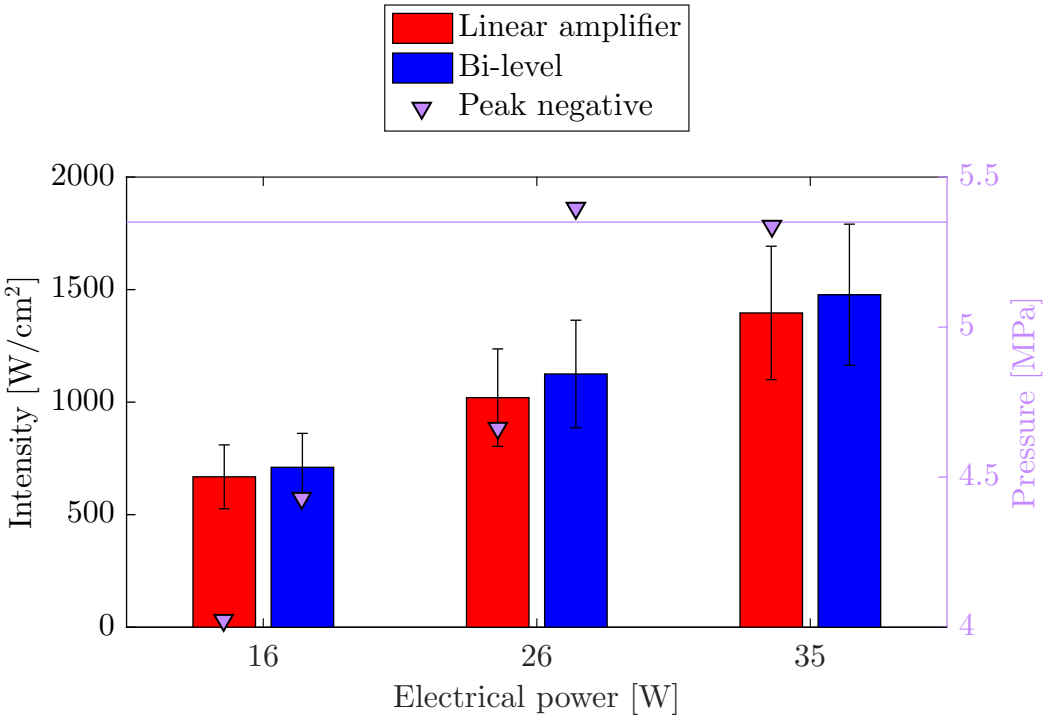

Figure 5.10: The measured acoustic intensity and transient pressure values for linear amplifier and bi-level excitations at all 3 electrical powers. Due to saturation of the hydrophone, it was not possible to obtain pressure measurements for bi-level at 35 W. The pink represents the suspected cavitation threshold.

pressure transients. With 26 W bi-level excitation, the PNP was larger than the PNP with the linear amplifier at both 26 and 35 W power levels. It is also expected that these transients are very close to the cavitation threshold as it was also not possible to produce thermal-only lesions with the linear amplifier at 38 W.

The cause for cavitation with bi-level excitation is not fully understood and warrants further investigation. It likely involves a number of factors including transients pre-conditioning the tissue [243] and focal region distortion which have both been observed and could be exacerbated by nonlinear propagation in tissue.

5.5.3 Secondary Effects from Compensation

The simulation results show that there was a loss in lesioning efficiency with distorted waveforms, however there may be secondary effects caused by the distortion if the pressure was increased to compensate for the attenuation in tissue. The peak positive pressure (PPP) was measured in the simulation results at the fundamental component and it was found that the PPP was 3% lower when using HRPWM and 7% lower when using bi-level. Experimentally it was expected that the pressure difference for HRPWM would be much smaller since the transducer is more effective at attenuating the higher order harmonics than the transfer function used (-30 dB, $f > 5$ MHz).

Clinically, larger depths and higher powers may be used, for example in the treatment of liver tissue. At these depths, focal pressure would be much more significant but could be compensated for by increasing the source pressure. This has clinical implications however as it means the relationship between electrical power and intensity at the focus becomes unknown. Additionally, it increases the likelihood of cavitation and shockwave formation.

Computational limitations mean it is difficult to simulate the depths used clinically in the treatment of liver, however it was possible to repeat the simulations with a slightly thicker medium (60 mm instead of 40 mm) with compensation for the loss of pressure at the focal region. Here, pre-focal lesioning at the surface of the tissue was observed with bi-level excitation. This was a secondary effect caused by the high harmonic content of bi-level excitation but

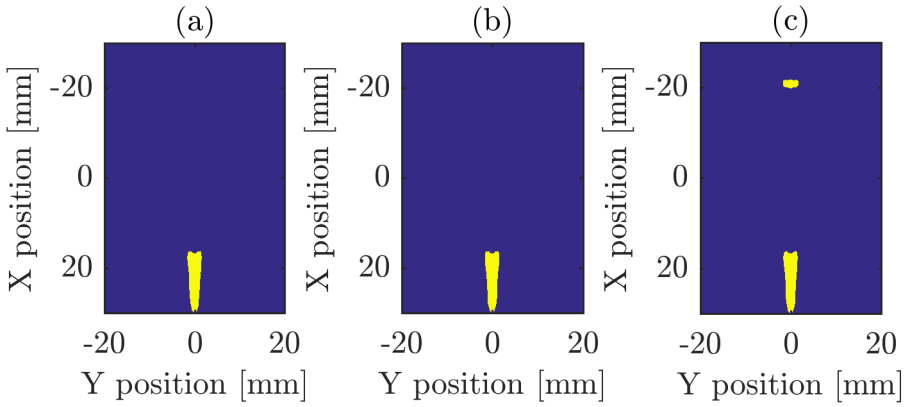

Figure 5.11: Simulated lesioning results when the loss of pressure in the fundamental component is compensated for. (a) was formed using linear amplifier, (b) with HRPWM and (c) with bi-level. Here, the bi-level causes pre-focal lesioning (38.34 mm^2), but HRPWM and the linear amplifier both produced similar sized lesions (32 mm^2)

was not observed using HRPWM. The results are shown in figure 5.11

5.6 Conclusions

HRPWM was compared with linear amplifier and bi-level excitations numerically and experimentally. In simulation, it was shown that increased harmonic distortion in the bi-level excitation waveform reduced the size of lesions. For the experiment, 3 waveforms of different powers were generated by adjusting the modulation parameter of HRPWM. Using these waveforms, lesions in ex vivo tissue were made and compared against lesions made at equivalent electrical powers using bi-level excitation and a linear amplifier. The experimental results showed that HRPWM could produce thermal-only lesions of an equival-

ent size to those made with a linear amplifier. At the lowest power level used, bi-level excitation produced smaller lesions, but transients in the waveform nucleated cavitation at the higher power levels.

The study showed that HRPWM was able to control acoustic pressure at intensities relevant to HIFU. The use of HRPWM will facilitate improvements in efficiency, practicality and cost for HIFU drive circuitry.

Chapter 6

Conclusions

The recent development of ultrasound research platforms has facilitated the experiments described in this thesis, where it was necessary to consider and control the nonlinear behaviour of waves. The thesis covered a broad range of areas from electronic waveform design through to dispersion in bone, which produced 2 journal papers and 5 conference proceedings. A comprehensive summary and conclusions now need to be drawn.

6.1 Motivation and Aims

Sound is a mechanical wave and is often modelled using a simple one-dimensional wave equation. This may be extended in a number of ways to consider attenuation, dispersion and *nonlinear*[1] propagation caused by large finite amplitudes. All these phenomena are frequency related, and with the trend continuing to use higher frequencies, they must now be increasingly taken into consideration. While these phenomena may be useful in guided wave inspection, they are generally a hindrance in other fields of ultrasound. Recently, researchers have developed a number of ultrasound research platforms such as the University of Leeds' UARP II and HIFUARP which the author aided in the development of. These platforms, like others, offer precise control of the transmit-receive sequencing and access to the raw un-beamformed receive data. This has provided a passage for the development of many new imaging techniques. So far how-

[1]Nonlinear propagation due to large signal amplitudes

ever, research has concerned only mostly-linear problems.

Therefore the aims of the thesis were to:

- Introduce the ultrasound platform used throughout the course of the PhD study.
- Introduce several nonlinear phenomena, and;
  - Discuss the implications of them on ultrasound system design.
  - Accordingly make any necessary improvements to the transmit architecture.
- Leverage the capabilities of the open platform design to develop new techniques and advance several existing ones that involve nonlinear phenomena.

6.2 Conclusions and Further Work

In chapter 2, the UARP II and HIFUARP were introduced. Both are based on the same architecture, but the former is transmit-only and is used for high-power therapeutic applications, while the latter serves as a fully-fledged imaging system. They both use a 5-level switched transmit circuits to achieve simultaneous amplitude and reduced harmonic distortion of the excitation waveforms. In this chapter, the desirability of this reduced harmonic distortion is identified from the perspective of nonlinear phenomena and is supported by several numerical experiments. Whilst harmonic distortion was shown to be undesirable, it does place timing constraints on the waveform which, as several bandwidth measurements show, may not be fully necessary. The constraints mean that some of the waveforms produced by HRPWM, a 5-level waveform design algorithm, are invalid for therapeutic excitation hardware. This is due to the speed-limitations of high-current MOSFETs. This, in turn, effects the capability of the hardware to control the power delivered to the array. When all types of hardware and transducers with varying bandwidths are considered, the number of possible waveform-solutions may be non-finite. A genetic algorithm (GA) was used to search this large space and produce more suitable

waveforms. The GA was effective and was able to achieve a granularity of 2% at 3.3 MHz where the existing 5-level schemes could not achieve any. The algorithm could be used to extend the transmit capabilities of existing switched systems and may increase the prevalence of switched electronics in HIFU systems, which could reduce the cost of treatment.

The motivation for the thesis was provided by a substantial number of nonlinear examples, but the described phenomena are by no means exhaustive and more could be considered. The genetic algorithm approach was shown to be effective at controlling any switching-generated harmonics, whilst simultaneously achieving other, seemingly conflicting objectives. Because the fitness function can be easily modified to suit many applications, the algorithm could be used as an effective waveform generation tool inside and outside the area of ultrasonics. It may prove increasingly useful in designs with exotic transducer technologies (eg dual mode use arrays), where elements are sensitive to multiple, non-integer-product frequencies, making schemes like HRPWM too constricting. There are some minor features that could be added to improve its versatility, such as amplitude or frequency modulation. The advent of new gallium-nitride-based switches may eventually render some of these approaches redundant due to the vastly improved switching speeds. However, GAN devices remain extremely expensive and so undermine the cost-saving purpose of using switched excitation. The techniques presented here will still be required to extend the usefulness of older designs and high-density array applications, where it will remain prohibitively expensive to use GAN technology.

The advantages of having such precise control over the sequencing of an ultrasound platform were demonstrated in chapter 3. Here, this new technology was applied to a problem of a nonlinear nature: guided waves. In NDT, these waves are widely used because they can travel great distances, and their multi-modal nature means they are sensitive to a range of defects. However, if one wants to spatially locate a defect, their inherently complex nonlinear behaviour makes traditional beam steering techniques ineffectual. Authors have already devised techniques to steer guided waves, but they require knowledge of the waveguide parameters which may not be known. Using the advanced receive and transmit architecture of the UARP II, a new scheme was devised that reinforced naturally propagating guided waves. The scheme induced a

Lamb wave in the material using the first transducer element and then recorded its propagation using the remaining elements. The adjacent element re-transmitted this recording and the process was repeated for every element. This caused constructive interference, which caused more of the guided wave energy to travel in the direction of the spatial influence of the transducer. The results in chapter 3 show that it is possible to control the direction of guided waves without knowledge of the waveguide's material parameters. This could make GW inspection automated, therefore more affordable and could also prove useful when inspecting units with an unknown composition of materials.

The technique would benefit from additional testing on real-world inspection problems to assess its usability. One concern might be that it enhances the direction of all modes, which may be undesirable since high order modes can be hard to separate. However, this but could be solved by filtering the receive waveforms before retransmission.

Continuing on this theme, guided waves in bone were then explored in chapter 4. Guided wave propagation is readily effected by the properties of the waveguide, and so many of bone's mechanical attributes may be inferred by observing these waves. This has implications in two fields: firstly in the assessment of osteoporosis which is actively researched, and secondly for measurement of skull properties to assist transcranial therapy, which was proposed here. The behaviour of guided waves is usually summarised by dispersion curves in either the frequency-phase velocity form or the frequency-wavenumber form. That being said, the former is preferred because it is more readily interpreted. These curves can be found by re-arranging the output of the two dimensional Fourier transform of a time-space matrix. However, this technique has limited resolve of the high-order modes, particularly when the number of spatial sample points is limited, which is often the case when taking measurements from bone. To improve on this, a technique was devised to temporally align dispersive modes across several transverse observations. In simulation, a multiplication-based method was applied and was shown to improve the intensity of the higher order modes. The technique was then applied to bone, in vivo and ex vivo, where it was found that, compared to Fourier methods, it was less sensitive to poor coupling and was better at extracting high order modes. The ageing population, as well as the inconvenience and

expense of DXA, means that ultrasonic methods are required for screening. Numerically the technique was shown to improve the S_3 and A_3 mode intensity by 6 dB and 13 dB respectively compared with the existing Fourier method. The technique could support the characterisation of the higher order modes in bone necessary for osteoporosis assessment.

With the skull, for any inferred properties to be useful, the induction or observation of waves must be co-located with the therapeutic array. Accordingly, a geometric relationship between the concave array and element time-delays necessary to generate guided-wave-inducing plane waves was found. To test this, simple aluminium cylinders were initially simulated. It was found that even when the distance travelled was subtracted, a change in group velocity of two wave packets was observed as the thickness was changed. This was in agreement with the expected behaviour. Similarly, with simulated skull models there was also a change in the group velocity for different thicknesses. It was shown that properties of the skull could be ascertained from guided wave measurements made using a phased array transducer in a concave configuration. The estimated maximum error using this technique was 0.2 mm. This could improve the accuracy, safety and efficacy of transcranial therapy.

The contribution of the dispersion phase shifting step in this chapter was significant. It could be considered equivalent to the delay stage in many receive beamformers, and other signal processing techniques could be applied to prove or disprove the existence of a correlation between transverse channels. The multiplication stage did introduce low-frequency artefacts, but these could be removed using a simple bandpass filter. Accordingly, the program code will be made freely available online to encourage researchers to improve these results by applying other beamforming techniques. Other applications such as NDT and SHM might benefit from this technique.

Transcranial arrays will continue to increase in density making localised detection of skull properties more plausible. More needs to be known about how these guided waves propagate around the complex multi-dimensional water-loaded structures, to draw exact properties from the measurements. Currently, any phase aberrations that could be measured, would not compete with the existing CT methods. However, measurement of attenuation might be a potential application; to the best of the author's knowledge, clinical transcranial

systems do not currently compensate for varying attenuation in the skull. This information cannot be obtained from a CT scan or from pulse-echo measurement but could be obtained from GW measurements.

In chapter 5, the impacts of the switching schemes that were described in chapter 2 on HIFU were considered. It was proposed, that because tissue attenuation, and thus lesioning efficacy is frequency dependent, there may be implications for heavily distorted excitation schemes. The 5-level HRPWM scheme described previously is advantageous because it can achieve amplitude control which is highly desirable in array HIFU applications. In simulation, it was shown that for a fixed acoustic power, the more distorted excitation schemes produced smaller lesions than their non-distorted counterparts. This was because more of the acoustic energy was attenuated before reaching the focal region. At larger depths, when this was compensated for it caused pre-focal lesioning. Experimentally, it was found that bi-level excitation nucleated cavitation because it caused transients in the acoustic waveform. For the three fixed acoustic powers tested, it was shown that HRPWM produced lesions the same size as their linear amplifier equivalents. The results here and in chapter 2 show that HRPWM could allow switched circuits to become more widely adopted in ultrasound hardware; yielding significant cost savings and miniaturisation.

6.3 Closing Remarks

There are implications of nonlinear phenomena, which need increasing consideration, in a wide range of areas including NDT and biomedicine. Overall it has been shown in this thesis that precise control of the nonlinear phenomena of waves can be afforded when using modern ultrasound research hardware. The methods described may reduce the cost and increase the efficacy of future ultrasound systems.

References

[1] C. Adams, D. M. Cowell, L. Nie, J. R. McLaughlan and S. Freear, 'A miniature HIFU excitation scheme to eliminate switching-induced grating lobes and nullify hard tissue attenuation', in *Ultrasonics Symposium (IUS), 2017 IEEE International*, IEEE, 2017, pp. 1–4.

[2] D. Cowell, T. Carpenter, P. Smith, C. Adams, S. Harput and S. Freear, 'Modified harmonic reduction pulse width modulation (mHRPWM) for switched excitation of resonant HIFU transducers', in *Ultrasonics Symposium (IUS), 2018 IEEE International*, IEEE, 2018, pp. 1–4.

[3] C. Adams, S. Harput, D. Cowell, T. M. Carpenter, D. M. Charutz and S. Freear, 'An adaptive array excitation scheme for the unidirectional enhancement of guided waves', *IEEE transactions on ultrasonics, ferroelectrics, and frequency control*, vol. 64, no. 2, pp. 441–451, 2017.

[4] C. Adams, S. Harput, D. Cowell, S. Freear and D. Charutz, 'Specimen-agnostic guided wave inspection using recursive feedback', in *IEEE International Ultrasonics Symposium (IUS)*, IEEE, 2016.

[5] C. Adams, S. Harput, D. Cowell and S. Freear, 'A phase velocity filter for the measurement of Lamb wave dispersion', in *IEEE International Ultrasonics Symposium (IUS)*, IEEE, 2016.

[6] C. Adams, J. McLaughlan, L. Nie and S. Freear, 'Excitation and acquisition of cranial guided waves using a concave array transducer', in *Proceedings of Meetings on Acoustics 173EAA*, ASA, vol. 30, 2017, p. 055 003.

[7] C. Adams, T. M. Carpenter, D. Cowell, S. Freear and J. R. McLaughlan, 'HIFU drive system miniaturisation using harmonic reduced pulse width modulation', *IEEE transactions on ultrasonics, ferroelectrics, and frequency control*, 2018.

[8] T. M. Carpenter, C. Adams, S. Freear, D. Cowell and J. McLaughlan, *Five Level Switched High Intensity Focused Ultrasound Driver Design*, Jul. 2018.

[9] S. R. Ansari, 'On the physical researches of alB̃iruni', *Indian Journal of History of Science*, vol. 11, 1975.

[10] C. B. Boyer and U. C. Merzbach, *A history of mathematics*. John Wiley & Sons, 2011.

[11] G. Galilei, *Galileo: Two new sciences (translation by stillman drake of galileo's 1638 discourses and mathematical demonstrations concerning two new sciences)*, 1974.

[12] J. W. S. B. Rayleigh, *The theory of sound*. Macmillan, 1896, vol. 2.

[13] H. Lamb, *The dynamical theory of sound*. Courier Corporation, 2004.

[14] J. Rose, 'Recent advances in guided wave NDE', *1995 IEEE Ultrasonics Symposium. Proceedings. An International Symposium*, 1995. DOI: 10.1109/ultsym.1995.495679.

[15] G. Ter Haar, 'Therapeutic applications of ultrasound', *Progress in biophysics and molecular biology*, vol. 93, no. 1, pp. 111–129, 2007.

[16] V. A. Khokhlova, M. R. Bailey, J. A. Reed, B. W. Cunitz, P. J. Kaczkowski and L. A. Crum, 'Effects of nonlinear propagation, cavitation, and boiling in lesion formation by high intensity focused ultrasound in a gel phantom', *The Journal of the Acoustical Society of America*, vol. 119, no. 3, pp. 1834–1848, 2006.

[17] S. Harput, *Use of chirps in medical ultrasound imaging*. University of Leeds, 2012.

[18] E. Boni, C. Alfred, S. Freear, J. A. Jensen and P. Tortoli, 'Ultrasound open platforms for next-generation imaging technique development', *IEEE Transactions on Ultrasonics, Ferroelectrics, and Frequency Control*, 2018.

[19] A. Marzo, T. Corkett and B. W. Drinkwater, 'Ultraino: An open phased-array system for narrowband airborne ultrasound transmission', *IEEE transactions on ultrasonics, ferroelectrics, and frequency control*, vol. 65, no. 1, pp. 102–111, 2018.

[20] E. Boni, L. Bassi, A. Dallai, F. Guidi, V. Meacci, A. Ramalli, S. Ricci and P. Tortoli, 'ULA-OP 256: A 256-channel open scanner for development and real-time implementation of new ultrasound methods', *IEEE transactions on ultrasonics, ferroelectrics, and frequency control*, vol. 63, no. 10, pp. 1488–1495, 2016.

[21] D. Cowell, T. Carpenter, P. Smith, C. Adams, S. Harput and S. Freear, 'Performance of switched mode arbitrary excitation using harmonic reduction pulse width modulation (HRPWM) in array imaging applications', in *Ultrasonics Symposium (IUS), 2016 IEEE International*, IEEE, 2016, pp. 1–4.

[22] L. Nie, S. Harput, D. M. Cowell, T. Carpenter, J. R. McLaughlan and S. Freear, 'Combining acoustic trapping with plane wave imaging for localized microbubble accumulation in large vessels', *IEEE Transactions on Ultrasonics, Ferroelectrics, and Frequency Control*, 2018.

[23] C. Adams, J. R. McLaughlan, L. Nie, D. Cowell, T. Carpenter and S. Freear, 'Excitation of leaky Lamb waves in cranial bone using a phased array transducer in a concave therapeutic configuration', *The Journal of the Acoustical Society of America*, 2017.

[24] R. Krimholtz, D. A. Leedom and G. L. Matthaei, 'New equivalent circuits for elementary piezoelectric transducers', *Electronics Letters*, vol. 6, no. 13, pp. 398–399, 1970.

[25] M. O'Donnell, 'Coded excitation system for improving the penetration of real-time phased-array imaging systems', *IEEE transactions on ul-*

trasonics, ferroelectrics, and frequency control, vol. 39, no. 3, pp. 341–351, 1992.

[26] S. Tang, S. Hui and H. Chung, 'A naturally soft-switched high-frequency gate drive circuit for power MOSFETs/IGBTs', in *Power Electronics and Drive Systems, 1999. PEDS'99. Proceedings of the IEEE 1999 International Conference on*, IEEE, vol. 1, 1999, pp. 246–252.

[27] M. M. El-Desouki and K. Hynynen, 'Driving circuitry for focused ultrasound noninvasive surgery and drug delivery applications', *Sensors*, vol. 11, no. 1, pp. 539–556, 2011.

[28] S. D. Kee, 'The class E/F family of harmonic-tuned switching power amplifiers', PhD thesis, California Institute of Technology, 2002.

[29] R. Seip, W. Chen, J. Tavakkoli, L. Frizzell and N. Sanghvi, 'High-intensity focused ultrasound (HIFU) phased arrays: Recent developments in transrectal transducers and driving electronics design', in *Proc. 3rd Int. Symp. on Therapeutic Ultrasound*, 2003, pp. 423–428.

[30] C. Christoffersen, W. Wong, S. Pichardo, G. Togtema and L. Curiel, 'Class-DE ultrasound transducer driver for HIFU therapy', *IEEE transactions on biomedical circuits and systems*, vol. 10, no. 2, pp. 375–382, 2016.

[31] E. Gaalaas, 'Class D audio amplifiers: What, why, and how', Analog Devices Inc., Tech. Rep., 2006.

[32] S. C. Tang and G. T. Clement, 'A harmonic cancellation technique for an ultrasound transducer excited by a switched-mode power converter', in *Ultrasonics Symposium, 2008. IUS 2008. IEEE*, IEEE, 2008, pp. 2076–2079.

[33] D. Cowell, P. Smith, S. Harput, J. McLaughlan and S. Freear, 'Non-linear harmonic reduction pulse width modulation (HRPWM) for the arbitrary control of transducer-integrated switched excitation electronics', *2014 IEEE International Ultrasonics Symposium*, 2014. DOI: 10.1109/ultsym.2014.0198.

[34] H. Meire and P. Farrant, *Basic ultrasound*, 1995.

[35] B. W. Drinkwater and P. D. Wilcox, 'Ultrasonic arrays for non-destructive evaluation: A review', *NDT & E International*, vol. 39, no. 7, pp. 525–541, 2006, ISSN: 0963-8695. DOI: 10.1016/j.ndteint.2006.03.006.

[36] OlympusNDT, *Phased array tutorial*, 2018.

[37] F. Xiaobing and H. Kullervo, 'Control of the necrosed tissue volume during noninvasive ultrasound surgery using a 16-element phased array', *Medical Physics*, vol. 22, no. 3, pp. 297–306, DOI: 10.1118/1.597603. eprint: https://aapm.onlinelibrary.wiley.com/doi/pdf/10.1118/1.597603.

[38] R. S. Cobbold, *Foundations of biomedical ultrasound*. Oxford University Press, 2006.

[39] C. P. Karunakaran and M. L. Oelze, 'Amplitude modulated chirp excitation to reduce grating lobes and maintain ultrasound intensity at the focus of an array', *Ultrasonics*, vol. 53, no. 7, pp. 1293–1303, 2013.

[40] E. S. Ebbini, H. Yao and A. Shrestha, 'Dual-mode ultrasound phased arrays for image-guided surgery', *Ultrasonic Imaging*, vol. 28, no. 2, pp. 65–82, 2006, PMID: 17094688. DOI: 10.1177/016173460602800201. eprint: http://dx.doi.org/10.1177/016173460602800201.

[41] J. A. Jensen, 'Field: A program for simulating ultrasound systems', in *10^{TH} NORDICBALTIC CONFERENCE ON BIOMEDICAL IMAGING, VOL. 4, SUPPLEMENT 1, PART 1: 351–353*, Citeseer, 1996.

[42] J. Civale, R. Clarke, I. Rivens and G. Ter Haar, 'The use of a segmented transducer for rib sparing in HIFU treatments', *Ultrasound in medicine & biology*, vol. 32, no. 11, pp. 1753–1761, 2006.

[43] F. J. Álvarez and R. Kuc, 'Dispersion relation for air via Kramers-Kronig analysis', *The Journal of the Acoustical Society of America*, vol. 124, no. 2, EL57–EL61, 2008.

[44] R. d. L. Kronig, 'On the theory of dispersion of x-rays', *Josa*, vol. 12, no. 6, pp. 547–557, 1926.

[45] J. S. Toll, 'Causality and the dispersion relation: Logical foundations', *Physical review*, vol. 104, no. 6, p. 1760, 1956.

[46] I. A. Viktorov, *Rayleigh and Lamb waves: physical theory and applications*. Plenum press, 1970.

[47] N. Bochud, Q. Vallet, J.-G. Minonzio and P. Laugier, 'Predicting bone strength with ultrasonic guided waves', *Scientific Reports*, vol. 7, p. 43 628, 2017.

[48] A. P. Duryea, T. L. Hall, A. D. Maxwell, Z. Xu, C. A. Cain and W. W. Roberts, 'Histotripsy erosion of model urinary calculi', *Journal of endourology*, vol. 25, no. 2, pp. 341–344, 2011.

[49] B. E. Treeby and B. T. Cox, 'K-wave: MATLAB toolbox for the simulation and reconstruction of photoacoustic wave fields', *Journal of biomedical optics*, vol. 15, no. 2, pp. 021 314–021 314, 2010.

[50] J. E. Lingeman, J. A. McAteer, E. Gnessin and A. P. Evan, 'Shock wave lithotripsy: Advances in technology and technique', *Nature Reviews Urology*, vol. 6, no. 12, p. 660, 2009.

[51] F. A. Duck, *Physical properties of tissues: a comprehensive reference book*. Academic press, 2013.

[52] M. A. O'Reilly, R. M. Jones and K. Hynynen, 'Three-dimensional transcranial ultrasound imaging of microbubble clouds using a sparse hemispherical array', *IEEE Transactions on Biomedical Engineering*, vol. 61, no. 4, pp. 1285–1294, 2014.

[53] D. A. Coley, *An introduction to genetic algorithms for scientists and engineers*. World Scientific Publishing Company, 1999.

[54] H. Aytug and G. J. Koehler, 'New stopping criterion for genetic algorithms', *European Journal of Operational Research*, vol. 126, no. 3, pp. 662–674, 2000.

[55] S. Baluja and R. Caruana, 'Removing the genetics from the standard genetic algorithm', in *Machine Learning Proceedings 1995*, Elsevier, 1995, pp. 38–46.

[56] M. Srinivas and L. M. Patnaik, 'Genetic algorithms: A survey', *computer*, vol. 27, no. 6, pp. 17–26, 1994.

[57] R. H. Silverman, 'High-resolution ultrasound imaging of the eye - a review', *Clinical & experimental ophthalmology*, vol. 37, no. 1, pp. 54–67, 2009.

[58] C. Fei, C. T. Chiu, X. Chen, Z. Chen, J. Ma, B. Zhu, K. K. Shung and Q. Zhou, 'Ultrahigh frequency (100 MHz-300 MHz) ultrasonic transducers for optical resolution medical imagining', *Scientific reports*, vol. 6, p. 28 360, 2016.

[59] K. Xu, D. Ta, B. Hu, P. Laugier and W. Wang, 'Wideband dispersion reversal of Lamb waves', *IEEE Transactions on Ultrasonics, Ferroelectrics, and Frequency Control*, vol. 61, no. 6, pp. 997–1005, Jun. 2014, ISSN: 0885-3010. DOI: 10.1109/TUFFC.2014.2995.

[60] M. Lowe, D. Alleyne and P. Cawley, 'Defect detection in pipes using guided waves', *Ultrasonics*, vol. 36, no. 1–5, pp. 147–154, 1998, Ultrasonics International 1997, ISSN: 0041-624X. DOI: 10.1016/S0041-624X(97)00038-3.

[61] J. Davies and P. Cawley, 'The application of synthetic focusing for imaging crack-like defects in pipelines using guided waves', *Ultrasonics, Ferroelectrics, and Frequency Control, IEEE Transactions on*, vol. 56, no. 4, pp. 759–771, 2009.

[62] I. Pelivanov, A. Shtokolov, C.-w. Wei and M. O'donnell, 'A 1 kHz a-scan rate pump-probe laser-ultrasound system for robust inspection of composites', *Ultrasonics, Ferroelectrics, and Frequency Control, IEEE Transactions on*, vol. 62, no. 9, pp. 1696–1703, 2015. DOI: 10.1109/TUFFC.2015.007110.

[63] A. K. Edwards, S. Savage, P. L. Hungler and T. W. Krause, 'Examination of f/a-18 honeycomb composite rudders for disbond due to water using through-transmission ultrasonics', *Ultrasound*, vol. 66, no. 2, 2011. DOI: 10.5755/j01.u.66.2.529.

[64] J. L. Rose, 'A baseline and vision of ultrasonic guided wave inspection potential', *Journal of Pressure Vessel Technology*, vol. 124, no. 3, p. 273, 2002. DOI: 10.1115/1.1491272.

[65] T. E. Michaels, J. E. Michaels and M. Ruzzene, 'Frequency-wavenumber domain analysis of guided wavefields', *Ultrasonics*, vol. 51, no. 4, pp. 452–466, 2011, ISSN: 0041-624X. DOI: 10.1016/j.ultras.2010.11.011.

[66] P. Cawley and D. Alleyne, 'The use of Lamb waves for the long range inspection of large structures', *Ultrasonics*, vol. 34, no. 2–5, pp. 287–290, 1996, Proceedings of Ultrasonics International 1995, ISSN: 0041-624X. DOI: 10.1016/0041-624X(96)00024-8.

[67] D. N. Alleyne and P. Cawley, 'Optimization of Lamb wave inspection techniques', *Ndt & E International*, vol. 25, no. 1, pp. 11–22, 1992.

[68] P. D. Wilcox, M. J. S. Lowe and P. Cawley, 'Mode and transducer selection for long range Lamb wave inspection', *Journal of Intelligent Material Systems and Structures*, vol. 12, no. 8, pp. 553–565, 2001. DOI: 10.1177/10453890122145348. eprint: http://jim.sagepub.com/content/12/8/553.full.pdf+html.

[69] S. Fateri, P. S. Lowe, B. Engineer and N. V. Boulgouris, 'Investigation of ultrasonic guided waves interacting with piezoelectric transducers', *IEEE Sensors Journal*, vol. 15, no. 8, pp. 4319–4328, 2015.

[70] A. Croxford, P. Wilcox, B. Drinkwater and G. Konstantinidis, 'Strategies for guided-wave structural health monitoring', *Proceedings of the Royal Society of London A: Mathematical, Physical and Engineering Sciences*, vol. 463, no. 2087, pp. 2961–2981, 2007, ISSN: 1364-5021. DOI: 10.1098/rspa.2007.0048. eprint: http://rspa.royalsocietypublishing.org/content/463/2087/2961.full.pdf.

[71] B. Ren and C. J. Lissenden, 'Pvdf multielement Lamb wave sensor for structural health monitoring', *IEEE transactions on ultrasonics, ferroelectrics, and frequency control*, vol. 63, no. 1, pp. 178–185, 2016.

[72] J.-B. Ihn and F.-K. Chang, 'Detection and monitoring of hidden fatigue crack growth using a built-in piezoelectric sensor/actuator network: Ii. validation using riveted joints and repair patches', *Smart Mater. Struct.*, vol. 13, no. 3, pp. 621–630, 2004. DOI: 10.1088/0964-1726/13/3/021.

[73] A. Perelli, L. De Marchi, A. Marzani and N. Speciale, 'Acoustic emission localization in plates with dispersion and reverberations using sparse PZT sensors in passive mode', *Smart Mater. Struct.*, vol. 21, no. 2, p. 025 010, 2012. DOI: 10.1088/0964-1726/21/2/025010.

[74] E. Baravelli, M. Senesi, M. Ruzzene and L. De Marchi, 'Fabrication and characterization of a wavenumber-spiral frequency-steerable acoustic transducer for source localization in plate structures', *IEEE Transactions on Instrumentation and Measurement*, vol. 62, no. 8, pp. 2197–2204, 2013. DOI: 10.1109/tim.2013.2255992.

[75] A. Mahmoud, D. Cortes, A. Abaza, H. Ammar, M. Hazey, P. Ngan, R. Crout and O. Mukdadi, 'Noninvasive assessment of human jawbone using ultrasonic guided waves', *IEEE Transactions on Ultrasonics, Ferroelectrics, and Frequency Control*, vol. 55, no. 6, pp. 1316–1327, Jun. 2008, ISSN: 0885-3010. DOI: 10.1109/TUFFC.2008.794.

[76] V. C. Protopappas, D. I. Fotiadis and K. N. Malizos, 'Guided ultrasound wave propagation in intact and healing long bones', *Ultrasound in medicine & biology*, vol. 32, no. 5, pp. 693–708, 2006.

[77] J. Foiret, J. G. Minonzio, C. Chappard, M. Talmant and P. Laugier, 'Combined estimation of thickness and velocities using ultrasound guided waves: A pioneering study on in vitro cortical bone samples', *IEEE Transactions on Ultrasonics, Ferroelectrics, and Frequency Control*, vol. 61, no. 9, pp. 1478–1488, Sep. 2014, ISSN: 0885-3010. DOI: 10.1109/TUFFC.2014.3062.

[78] A. Mahmoud, D. Cortes, A. Abaza, H. Ammar, O. Mukdadi, M. Hazey, P. Ngan and R. Crout, 'P5A-10 Assessment of human jawbone using ultrasonic guided wave: In vitro study', in *Ultrasonics Symposium, 2007. IEEE*, Oct. 2007, pp. 2183–2186. DOI: 10.1109/ULTSYM.2007.549.

[79] P. Moilanen, P. H. Nicholson, V. Kilappa, S. Cheng and J. Timonen, 'Assessment of the cortical bone thickness using ultrasonic guided waves: Modelling and in vitro study', *Ultrasound in medicine & biology*, vol. 33, no. 2, pp. 254–262, 2007.

[80] E. Maksuti, E. Widman, D. Larsson, M. W. Urban, M. Larsson and A. Bjällmark, 'Arterial stiffness estimation by shear wave elastography: Validation in phantoms with mechanical testing', *Ultrasound in Medicine and Biology*, vol. 42, no. 1, pp. 308–321, Mar. 2016, ISSN: 0301-5629. DOI: 10.1016/j.ultrasmedbio.2015.08.012.

[81] M. J. S. Lowe, R. E. Challis and C. W. Chan, 'The transmission of Lamb waves across adhesively bonded lap joints', *The Journal of the Acoustical Society of America*, vol. 107, no. 3, pp. 1333–1345, 2000. DOI: 10.1121/1.428420.

[82] E. Moreno and P. Acevedo, 'Thickness measurement in composite materials using Lamb waves', *Ultrasonics*, vol. 35, no. 8, pp. 581–586, 1998.

[83] W. Zhu and J. L. Rose, 'Lamb wave generation and reception with time-delay periodic linear arrays: A bem simulation and experimental study', *Ultrasonics, Ferroelectrics, and Frequency Control, IEEE Transactions on*, vol. 46, no. 3, pp. 654–664, 1999.

[84] J. L. Rose, *Ultrasonic Waves in Solid Media*. Cambridge University Press, 1999.

[85] V. Dayal and V. K. Kinra, 'Leaky Lamb waves in an anisotropic plate. i: An exact solution and experiments', *The Journal of the Acoustical Society of America*, vol. 85, no. 6, pp. 2268–2276, 1989. DOI: 10.1121/1.397772.

[86] J. Rose, 'Guided wave nuances for ultrasonic nondestructive evaluation', *IEEE Transactions on Ultrasonics, Ferroelectrics and Frequency Control*, vol. 47, no. 3, pp. 575–583, 2000. DOI: 10.1109/58.842044.

[87] P. Khalili and P. Cawley, 'Excitation of single-mode Lamb waves at high-frequency-thickness products', *IEEE transactions on ultrasonics, ferroelectrics, and frequency control*, vol. 63, no. 2, pp. 303–312, 2016.

[88] P. Fromme, P. Wilcox, M. J. S. Lowe and P. Cawley, 'On the development and testing of a guided ultrasonic wave array for structural integrity monitoring', *IEEE Transactions on Ultrasonics, Ferroelectrics, and Frequency Control*, vol. 53, no. 4, pp. 777–785, Apr. 2006, ISSN: 0885-3010. DOI: 10.1109/TUFFC.2006.1621505.

[89] D. Alleyne and P. Cawley, 'A two-dimensional fourier transform method for the measurement of propagating multimode signals', *The Journal of the Acoustical Society of America*, vol. 89, no. 3, pp. 1159–1168, 1991.

[90] D. N. Alleyne and P. Cawley, 'The interaction of Lamb waves with defects', *IEEE transactions on ultrasonics, ferroelectrics, and frequency control*, vol. 39, no. 3, pp. 381–397, 1992.

[91] M. Harb and F. Yuan, 'Non-contact ultrasonic technique for Lamb wave characterization in composite plates', *Ultrasonics*, vol. 64, pp. 162–169, 2016.

[92] Y. Cho and J. L. Rose, 'A boundary element solution for a mode conversion study on the edge reflection of Lamb waves', *The Journal of the Acoustical Society of America*, vol. 99, no. 4, pp. 2097–2109, 1996.

[93] O. Asfar, B. Morvan and J.-L. Izbicki, 'Three-mode coupling of symmetric and antisymmetric Lamb waves in plates with finite corrugations', *IEEE transactions on ultrasonics, ferroelectrics, and frequency control*, vol. 62, no. 3, pp. 524–530, 2015.

[94] P. S. Tua, S. T. Quek and Q. Wang, 'Detection of cracks in plates using piezo-actuated Lamb waves', *Smart Materials and Structures*, vol. 13, no. 4, p. 643, 2004.

[95] J. E. Michaels, A. J. Croxford and P. D. Wilcox, 'Imaging algorithms for locating damage via in situ ultrasonic sensors', in *Sensors Applications Symposium, 2008. SAS 2008. IEEE*, Feb. 2008, pp. 63–67.

[96] S. Fu, L. Shi, Y. Zhou and J. Cai, 'Dispersion compensation in Lamb wave defect detection with step-pulse excitation and warped frequency transform', *IEEE Transactions on Ultrasonics, Ferroelectrics, and Frequency Control*, vol. 61, no. 12, pp. 2075–2088, Dec. 2014, ISSN: 0885-3010. DOI: 10.1109/TUFFC.2014.006606.

[97] X. Chen, J. E. Michaels and T. E. Michaels, 'A methodology for estimating guided wave scattering patterns from sparse transducer array measurements', *IEEE transactions on ultrasonics, ferroelectrics, and frequency control*, vol. 62, no. 1, pp. 208–219, 2015.

[98] Y. Lu and J. Saniie, 'Adaptive filtering and fractional Fourier transform for ultrasonic signal processsing and flaw detection', in *Ultrasonics Symposium (IUS), 2014 IEEE International*, Sep. 2014, pp. 1932–1935. DOI: 10.1109/ULTSYM.2014.0480.

[99] G. Konstantinidis, P. D. Wilcox and B. W. Drinkwater, 'An investigation into the temperature stability of a guided wave structural health monitoring system using permanently attached sensors', *IEEE Sensors Journal*, vol. 7, no. 5, pp. 905–912, May 2007, ISSN: 1530-437X. DOI: 10.1109/JSEN.2007.894908.

[100] J. Bingham and M. Hinders, 'Lamb wave detection of delaminations in large diameter pipe coatings', *Open Acoustics Journal*, vol. 2, pp. 75–86, 2009.

[101] K. K. Shung, M. B. Smith and B. M. W. Tsui, *Principles of medical imaging*. Academic Press, 1992.

[102] L. Moreau, B. W. Drinkwater and P. D. Wilcox, 'Ultrasonic imaging algorithms with limited transmission cycles for rapid nondestructive evaluation', *IEEE Transactions on Ultrasonics, Ferroelectrics, and Frequency Control*, vol. 56, no. 9, pp. 1932–1944, Sep. 2009, ISSN: 0885-3010. DOI: 10.1109/TUFFC.2009.1269.

[103] J. Zhang, B. W. Drinkwater, P. D. Wilcox and A. J. Hunter, 'Defect detection using ultrasonic arrays: The multi-mode total focusing method', *NDT & E International*, vol. 43, no. 2, pp. 123–133, 2010, ISSN: 0963-8695. DOI: 10.1016/j.ndteint.2009.10.001.

[104] C. F. Vasile, 'Periodic magnet unidirectional transducer', 4 232 557, Nov. 1980.

[105] J. Li and J. L. Rose, 'Implementing guided wave mode control by use of a phased transducer array', *IEEE transactions on ultrasonics, ferroelectrics, and frequency control*, vol. 48, no. 3, pp. 761–768, 2001.

[106] D. M. Charutz, E. Mor, S. Harput, D. M. J. Cowell, P. R. Smith and S. Freear, 'Guided wave enhancement phased array beamforming scheme using recursive feedback', in *2013 IEEE International Ultrasonics Sym-*

posium (IUS), Jul. 2013, pp. 166–169. DOI: 10.1109/ULTSYM.2013.0043.

[107] A. Gachagan, G. Hayward, A. McNab, P. Reynolds, S. G. Pierce, W. R. Philp and B. Culshaw, 'Generation and reception of ultrasonic guided waves in composite plates using conformable piezoelectric transmitters and optical-fiber detectors', *IEEE Transactions on Ultrasonics, Ferroelectrics, and Frequency Control*, vol. 46, no. 1, pp. 72–81, Jan. 1999, ISSN: 0885-3010. DOI: 10.1109/58.741426.

[108] I. Bartoli, A. Marzani, F. L. di Scalea and E. Viola, 'Modeling wave propagation in damped waveguides of arbitrary cross-section', *Journal of Sound and Vibration*, vol. 295, no. 3–5, pp. 685–707, 2006.

[109] P. Bocchini, A. Marzani and E. Viola, 'Graphical user interface for guided acoustic waves', *Journal of Computing in Civil Engineering*, vol. 25, no. 3, pp. 202–210, 2011. DOI: 10.1061/(ASCE)CP.1943-5487.0000081.

[110] P. N. Marty, N. Desai and J. Andersson, 'NDT of kissing bond in aeronautical structures', in *16th World Conference on NDT*, 2004.

[111] N. Guo and P. Cawley, 'The interaction of Lamb waves with delaminations in composite laminates', *The Journal of the Acoustical Society of America*, vol. 94, no. 4, pp. 2240–2246, 1993.

[112] F. L. di Scalea, P. Rizzo and A. Marzani, 'Propagation of ultrasonic guided waves in lap-shear adhesive joints: Case of incident a0 Lamb wave', *The Journal of the Acoustical Society of America*, vol. 115, no. 1, pp. 146–156, 2004.

[113] J. B. Harley and J. M. Moura, 'Data-driven and calibration-free Lamb wave source localization with sparse sensor arrays', *IEEE transactions on ultrasonics, ferroelectrics, and frequency control*, vol. 62, no. 8, pp. 1516–1529, 2015.

[114] S. E. Burrows, B. Dutton and S. Dixon, 'Laser generation of Lamb waves for defect detection: Experimental methods and finite element modeling', *IEEE Transactions on Ultrasonics, Ferroelectrics, and Fre-*

quency Control, vol. 59, no. 1, pp. 82–89, Jan. 2012, ISSN: 0885-3010. DOI: 10.1109/TUFFC.2012.2158.

[115] R. Levine and J. Michaels, 'Block-sparse reconstruction and imaging for Lamb wave structural health monitoring', *IEEE Transactions on Ultrasonics, Ferroelectrics, and Frequency Control*, vol. 61, no. 6, pp. 1006–1015, Jun. 2014, ISSN: 0885-3010. DOI: 10.1109/TUFFC.2014.2996.

[116] J. Hall and J. Michaels, 'Minimum variance ultrasonic imaging applied to an in situ sparse guided wave array', *IEEE Transactions on Ultrasonics, Ferroelectrics, and Frequency Control*, vol. 57, no. 10, pp. 2311–2323, Oct. 2010, ISSN: 0885-3010. DOI: 10.1109/TUFFC.2010.1692.

[117] A. Gachagan, P. Reynolds, G. Hayward and A. McNab, 'Construction and evaluation of a new generation of flexible ultrasonic transducers', in *Ultrasonics Symposium, 1996. Proceedings., 1996 IEEE*, vol. 2, Nov. 1996, pp. 853–8562. DOI: 10.1109/ULTSYM.1996.584127.

[118] B. Hailu, G. Hayward, A. Gachagan, A. McNab and R. Farlow, 'Comparison of different piezoelectric materials for the design of embedded transducers for structural health monitoring applications', in *Ultrasonics Symposium, 2000 IEEE*, vol. 2, Oct. 2000, pp. 1009–10 122. DOI: 10.1109/ULTSYM.2000.921495.

[119] A. Gachagan, G. Hayward and R. Banks, 'A flexible piezoelectric transducer design for efficient generation and reception of ultrasonic Lamb waves', *IEEE Transactions on Ultrasonics, Ferroelectrics, and Frequency Control*, vol. 52, no. 7, pp. 1175–1182, Jul. 2005, ISSN: 0885-3010. DOI: 10.1109/TUFFC.2005.1504004.

[120] P. Marin-Franch, S. Cochran and K. Kirk, 'Progress towards ultrasound applications of new single crystal materials', *Journal of Materials Science: Materials in Electronics*, vol. 15, no. 11, pp. 715–720, 2004, ISSN: 1573-482X. DOI: 10.1023/B:JMSE.0000043418.10953.38.

[121] M. Castaings and P. Cawley, 'The generation, propagation, and detection of Lamb waves in plates using air-coupled ultrasonic transducers', *The Journal of the Acoustical Society of America*, vol. 100, no. 5, pp. 3070–3077, 1996. DOI: 10.1121/1.417193.

[122] J. E. Michaels, S. J. Lee, A. J. Croxford and P. D. Wilcox, 'Chirp excitation of ultrasonic guided waves', *Ultrasonics*, vol. 53, no. 1, pp. 265–270, 2013, ISSN: 0041-624X. DOI: 10.1016/j.ultras.2012.06.010.

[123] P. Augat and S. Schorlemmer, 'The role of cortical bone and its microstructure in bone strength', *Age and ageing*, vol. 35, no. suppl 2, pp. ii27–ii31, 2006.

[124] S. Bernard, J. Schneider, P. Varga, P. Laugier, K. Raum and Q. Grimal, 'Elasticity-density and viscoelasticity-density relationships at the tibia mid-diaphysis assessed from resonant ultrasound spectroscopy measurements', *Biomechanics and modeling in mechanobiology*, vol. 15, no. 1, pp. 97–109, 2016.

[125] Q. Grimal, K. Raum, A. Gerisch and P. Laugier, 'A determination of the minimum sizes of representative volume elements for the prediction of cortical bone elastic properties', *Biomechanics and Modeling in Mechanobiology*, vol. 10, no. 6, pp. 925–937, 2011, ISSN: 1617-7940. DOI: 10.1007/s10237-010-0284-9.

[126] P. Droin, G. Berger and P. Laugier, 'Velocity dispersion of acoustic waves in cancellous bone', *IEEE transactions on ultrasonics, ferroelectrics, and frequency control*, vol. 45, no. 3, pp. 581–592, 1998.

[127] N. Bochud, J.-G. Minonzio, Q. Vallet and P. Laugier, 'An anisotropic bilayer model to gain insight into in-vivo guided wave measurements', in *Ultrasonic Characterization of Bone (ESUCB), 2015 6th European Symposium on*, IEEE, 2015, pp. 1–4.

[128] P. H. Nicholson, P. Moilanen, T. Kärkkäinen, J. Timonen and S. Cheng, 'Guided ultrasonic waves in long bones: Modelling, experiment and in vivo application', *Physiological measurement*, vol. 23, no. 4, p. 755, 2002.

[129] C. Baron, M. Talmant and P. Laugier, 'Effect of porosity on effective diagonal stiffness coefficients (CII) and elastic anisotropy of cortical bone at 1 MHz: A finite-difference time domain study', *The Journal of the Acoustical Society of America*, vol. 122, no. 3, pp. 1810–1817, 2007.

[130] J. Y. Rho, R. B. Ashman and C. H. Turner, 'Young's modulus of trabecular and cortical bone material: Ultrasonic and microtensile measurements', *Journal of biomechanics*, vol. 26, no. 2, pp. 111–119, 1993.

[131] P. Moilanen, 'Ultrasonic guided waves in bone', *IEEE transactions on ultrasonics, ferroelectrics, and frequency control*, vol. 55, no. 6, 2008.

[132] P. Moilanen, M. Talmant, V. Kilappa, P. Nicholson, S. Cheng, J. Timonen and P. Laugier, 'Modeling the impact of soft tissue on axial transmission measurements of ultrasonic guided waves in human radius', *The Journal of the Acoustical Society of America*, vol. 124, no. 4, pp. 2364–2373, 2008.

[133] E. Bossy, M. Talmant, M. Defontaine, F. Patat and P. Laugier, 'Bidirectional axial transmission can improve accuracy and precision of ultrasonic velocity measurement in cortical bone: A validation on test materials', *IEEE transactions on ultrasonics, ferroelectrics, and frequency control*, vol. 51, no. 1, pp. 71–79, 2004.

[134] C. W. Connor and K. Hynynen, 'Patterns of thermal deposition in the skull during transcranial focused ultrasound surgery', *IEEE transactions on biomedical engineering*, vol. 51, no. 10, pp. 1693–1706, 2004.

[135] G. Pinton, J.-F. Aubry, E. Bossy, M. Muller, M. Pernot and M. Tanter, 'Attenuation, scattering, and absorption of ultrasound in the skull bone', *Medical physics*, vol. 39, no. 1, pp. 299–307, 2012.

[136] R. Sharma and F. Gaillard. (2018). Platybasia, [Online]. Available: `https://radiopaedia.org/articles/platybasia`.

[137] J. A. Kanis *et al.*, 'Assessment of osteoporosis at the primary healthcare level', Technical Report. WHO Collaborating Centre, University of Sheffield, UK, Tech. Rep., 2008.

[138] U.S. Preventive Services Task Force, 'Screening for osteoporosis: U.S. preventive services task force recommendation statement', *Annals of Internal Medicine*, vol. 154, no. 5, pp. 356–364, 2011. DOI: `10.7326/0003-4819-154-5-201103010-00307`. eprint: `/data/journals/aim/20227/0000605-201103010-00010.pdf`. [Online]. Available: `+%20http://dx.doi.org/10.7326/0003-4819-154-5-201103010-00307`.

[139] N. H. Service, 'How it is performed, DEXA (DXA) scan', *NHS Health A-Z*, 2016.

[140] N. I. for Health, 'What people with diabetes need to know about osteoporosis', *Osteoporosis*, 2016, `https://www.bones.nih.gov/health-info/bone/osteoporosis/conditions-behaviors/diabetes`.

[141] S. Prins, H. Jorgensen, L. Jorgensen and C. Hassager, 'The role of quantitative ultrasound in the assessment of bone: A review', *Clin Physiol*, 1997.

[142] D. Hans, T. Fuerst and F. Duboeuf, 'Quantitative ultrasound bone measurement', *European radiology*, vol. 7, no. 2, S43, 1997.

[143] P. Laugier, 'Quantitative ultrasound of bone: Looking ahead', *Joint Bone Spine*, vol. 73, no. 2, pp. 125–128, 2006.

[144] Y. Bala, R. Zebaze and E. Seeman, 'Role of cortical bone in bone fragility', *Current opinion in rheumatology*, vol. 27, no. 4, pp. 406–413, 2015.

[145] V. C. Protopappas, I. C. Kourtis, L. C. Kourtis, K. N. Malizos, C. V. Massalas and D. I. Fotiadis, 'Three-dimensional finite element modeling of guided ultrasound wave propagation in intact and healing long bones', *The Journal of the Acoustical Society of America*, vol. 121, no. 6, pp. 3907–3921, 2007.

[146] K. Raum, I. Leguerney, F. Chandelier, E. Bossy, M. Talmant, A. Saied, F. Peyrin and P. Laugier, 'Bone microstructure and elastic tissue properties are reflected in QUS axial transmission measurements', *Ultrasound in medicine & biology*, vol. 31, no. 9, pp. 1225–1235, 2005.

[147] N. O. Kuchuk, N. M. Van Schoor, S. M. Pluijm, J. H. Smit, W. De Ronde and P. Lips, 'The association of sex hormone levels with quantitative ultrasound, bone mineral density, bone turnover and osteoporotic fractures in older men and women', *Clinical endocrinology*, vol. 67, no. 2, pp. 295–303, 2007.

[148] V. Egorov, A. Tatarinov, N. Sarvazyan, R. Wood, L. Magidenko, S. Amin, S. Khosla, R. J. Ruh, J. M. Ruh and A. Sarvazyan, 'Osteoporosis detection in postmenopausal women using axial transmission multi-frequency bone ultrasonometer: Clinical findings', *Ultrasonics*, vol. 54, no. 5, pp. 1170–1177, 2014.

[149] A. Sarvazyan, A. Tatarinov, V. Egorov, S. Airapetian, V. Kurtenok and C. J. Gatt, 'Application of the dual-frequency ultrasonometer for osteoporosis detection', *Ultrasonics*, vol. 49, no. 3, pp. 331–337, 2009.

[150] E. Bossy, M. Talmant and P. Laugier, 'Effect of bone cortical thickness on velocity measurements using ultrasonic axial transmission: A 2D simulation study', *The Journal of the Acoustical Society of America*, vol. 112, no. 1, pp. 297–307, 2002.

[151] ——, 'Three-dimensional simulations of ultrasonic axial transmission velocity measurement on cortical bone models', *The Journal of the Acoustical Society of America*, vol. 115, no. 5, pp. 2314–2324, 2004.

[152] V. Kilappa, K. Xu, P. Moilanen, E. Heikkola, D. Ta and J. Timonen, 'Assessment of the fundamental flexural guided wave in cortical bone by an ultrasonic axial-transmission array transducer', *Ultrasound in medicine & biology*, vol. 39, no. 7, pp. 1223–1232, 2013.

[153] K. D. Evans, B. Weiss and M. Knopp, 'High-intensity focused ultrasound (HIFU) for specific therapeutic treatments: A literature review', *Journal of Diagnostic Medical Sonography*, vol. 23, no. 6, pp. 319–327, 2007.

[154] R. Illing, J. Kennedy, F. Wu, G. Ter Haar, A. Protheroe, P. Friend, F. Gleeson, D. Cranston, R. Phillips and M. Middleton, 'The safety and feasibility of extracorporeal high-intensity focused ultrasound (HIFU) for the treatment of liver and kidney tumours in a western population', *British journal of cancer*, vol. 93, no. 8, p. 890, 2005.

[155] M. Huisman, G. Ter Haar, A. Napoli, A. Hananel, P. Ghanouni, G. Lövey, R. J. Nijenhuis, M. A. Van Den Bosch, V. Rieke, S. Majumdar *et al.*, 'International consensus on use of focused ultrasound for painful

bone metastases: Current status and future directions', *International Journal of Hyperthermia*, vol. 31, no. 3, pp. 251–259, 2015.

[156] D. Bianchini, F. Marcocci, E. Menghi, V. D'Errico, E. Mezzenga and A. Sarnelli, 'Treatment plan verification in MRgFUs for bone metastasis pain palliation', *Physica Medica: European Journal of Medical Physics*, vol. 32, p. 248, 2016.

[157] P. Smirnov and K. Hynynen, 'Design of a HIFU array for the treatment of deep venous thrombosis: A simulation study.', *Physics in medicine and biology*, 2017.

[158] A. Partanen, P. S. Yarmolenko, A. Viitala, S. Appanaboyina, D. Haemmerich, A. Ranjan, G. Jacobs, D. Woods, J. Enholm, B. J. Wood *et al.*, 'Mild hyperthermia with magnetic resonance-guided high-intensity focused ultrasound for applications in drug delivery', *International journal of hyperthermia*, vol. 28, no. 4, pp. 320–336, 2012.

[159] M. Pernot, J.-F. Aubry, M. Tanter, A.-L. Boch, F. Marquet, M. Kujas, D. Seilhean and M. Fink, 'In vivo transcranial brain surgery with an ultrasonic time reversal mirror', *Journal of neurosurgery*, vol. 106, no. 6, pp. 1061–1066, 2007.

[160] J. Blackmore, M. Veldsman, C. Butler and R. Cleveland, 'Focusing ultrasound through the skull for neuromodulation', *The Journal of the Acoustical Society of America*, vol. 141, no. 5, pp. 3549–3549, 2017.

[161] O. Naor, S. Krupa and S. Shoham, 'Ultrasonic neuromodulation', *Journal of neural engineering*, vol. 13, no. 3, p. 031 003, 2016.

[162] A. Pulkkinen, Y. Huang, J. Song and K. Hynynen, 'Simulations and measurements of transcranial low-frequency ultrasound therapy: Skull-base heating and effective area of treatment', *Physics in Medicine & Biology*, vol. 56, no. 15, p. 4661, 2011.

[163] M. Pernot, J.-F. Aubry, M. Tanter, J.-L. Thomas and M. Fink, 'High power transcranial beam steering for ultrasonic brain therapy', *Physics in medicine and biology*, vol. 48, no. 16, p. 2577, 2003.

[164] G. Clement and K. Hynynen, 'A non-invasive method for focusing ultrasound through the human skull', *Physics in Medicine & Biology*, vol. 47, no. 8, p. 1219, 2002.

[165] J. White, G. T. Clement and K. Hynynen, 'Transcranial ultrasound focus reconstruction with phase and amplitude correction', *IEEEE transactions on ultrasonics, ferroelectrics, and frequency control*, vol. 52, no. 9, pp. 1518–1522, 2005, `https://www.nhs.uk/conditions/dexa-scan/what-happens/`.

[166] H. Estrada, J. Rebling and D. Razansky, 'Prediction and near-field observation of skull-guided acoustic waves', *Physics in Medicine and Biology*, vol. 62, p. 4728, 2017.

[167] N. Bochud, J.-G. Minonzio, Q. Vallet and P. Laugier, 'A genetic algorithms-based optimization method for estimating thickness and porosity of cortical bone from guided wave measurements', in *Ultrasonic Characterization of Bone (ESUCB), 2015 6th European Symposium on*, IEEE, 2015, pp. 1–4.

[168] P. Moilanen, P. Nicholson, V. Kilappa, S. Cheng and J. Timonen, 'Measuring guided waves in long bones: Modeling and experiments in free and immersed plates', *Ultrasound in medicine & biology*, vol. 32, no. 5, pp. 709–719, 2006.

[169] J. L. Rose, *Ultrasonic waves in solid media*, 2000.

[170] K. T. Onwuama, S. O. Salami, M. Ali and J. O. Nzalak, 'Effect of different methods of bone preparation on the skeleton of the African giant pouched rat (cricetomys gambianus).', *International Journal of Morphology*, vol. 30, no. 2, 2012.

[171] L. G. Mandarano-Filho, M. T. Bezuti, N. Mazzer and C. H. Barbieri, 'Influence of cortical bone thickness on the ultrasound velocity', *Acta ortopedica brasileira*, vol. 20, no. 3, pp. 184–190, 2012.

[172] S. Qiao, X. Shang and E. Pan, 'Elastic guided waves in a coated spherical shell', *Nondestructive Testing and Evaluation*, vol. 31, no. 2, pp. 165–190, 2016.

[173] A. N. Norris and A. Shuvalov, 'Elastodynamics of radially inhomogeneous spherically anisotropic elastic materials in the stroh formalism', in *Proc. R. Soc. A*, The Royal Society, vol. 468, 2012, pp. 467–484.

[174] J. Qu, Y. Berthelot and Z. Li, 'Dispersion of guided circumferential waves in a circular annulus', 1996.

[175] G. Gaunaurd and M. Werby, 'Similarities between various Lamb waves in submerged spherical shells, and rayleigh waves in elastic spheres and flat half-spaces', *The Journal of the Acoustical Society of America*, vol. 89, no. 6, pp. 2731–2739, 1991.

[176] W. Sachse and Y.-H. Pao, 'On the determination of phase and group velocities of dispersive waves in solids', *Journal of Applied Physics*, vol. 49, no. 8, pp. 4320–4327, 1978.

[177] L. Mažeika and L. Draudvilienė, 'Analysis of the zero-crossing technique in relation to measurements of phase velocities of the Lamb waves', *Ultrasound*, vol. 66, no. 2, pp. 7–12, 2010.

[178] T. Pialucha, C. Guyott and P. Cawley, 'Amplitude spectrum method for the measurement of phase velocity', *Ultrasonics*, vol. 27, no. 5, pp. 270–279, 1989.

[179] D. Waltisberg and R. Raišutis, 'Group velocity estimation of Lamb waves based on the wavelet transform', *Ultragarsas (Ultrasound)*, vol. 63, no. 4, pp. 35–40, 2008.

[180] D. N. Alleyne and P. Cawley, 'A 2-dimensional Fourier transform method for the quantitative measurement of Lamb modes', in *Ultrasonics Symposium, 1990. Proceedings., IEEE 1990*, IEEE, 1990, pp. 1143–1146.

[181] M. Niethammer, L. J. Jacobs, J. Qu and J. Jarzynski, 'Time-frequency representations of Lamb waves', *The Journal of the Acoustical Society of America*, vol. 109, no. 5, pp. 1841–1847, 2001.

[182] J.-G. Minonzio, M. Talmant and P. Laugier, 'Measurement of guided mode wave vectors by analysis of the transfer matrix obtained with multi-emitters and multi-receivers in contact', in *Journal of Physics: Conference Series*, IOP Publishing, vol. 269, 2011, p. 012 003.

[183] J.-G. Minonzio, M. Talmant and P. Laugier, 'Guided wave phase velocity measurement using multi-emitter and multi-receiver arrays in the axial transmission configuration', *The Journal of the Acoustical Society of America*, vol. 127, no. 5, pp. 2913–2919, 2010.

[184] G. Matrone, A. Savoia, G. Caliano and G. Magenes, 'The delay multiply and sum beamforming algorithm in ultrasound b-mode medical imaging.', *IEEE Trans. Med. Imaging*, vol. 34, no. 4, pp. 940–949, 2015.

[185] D.-a. Ta, K. Huang, W.-q. Wang, Y.-y. Wang and L. H. Le, 'Identification and analysis of multimode guided waves in tibia cortical bone', *Ultrasonics*, vol. 44, e279–e284, 2006.

[186] J.-G. Minonzio, J. Foiret, P. Moilanen, J. Pirhonen, Z. Zhao, M. Talmant, J. Timonen and P. Laugier, 'A free plate model can predict guided modes propagating in tubular bone-mimicking phantoms', *The Journal of the Acoustical Society of America*, vol. 137, no. 1, EL98–EL104, 2015.

[187] P. Ghanouni, K. B. Pauly, W. J. Elias, J. Henderson, J. Sheehan, S. Monteith and M. Wintermark, 'Transcranial MRI-guided focused ultrasound: A review of the technologic and neurologic applications', *American Journal of Roentgenology*, vol. 205, no. 1, pp. 150–159, 2015.

[188] G. Ter Haar, 'Ultrasound focal beam surgery', *Ultrasound in medicine & biology*, vol. 21, no. 9, pp. 1089–1100, 1995.

[189] M. Lee, D. Schlesinger, G. ter Haar, B. Sela, M. Eames, J. Snell, A. Hananel, N. Kassell, J. Sheehan, J. Larner *et al.*, 'Thermal dose and radiation dose comparison based on cell survival', *Journal of Therapeutic Ultrasound*, vol. 3, no. 1, P26, 2015.

[190] Z. Izadifar, P. Babyn and D. Chapman, 'Mechanical and biological effects of ultrasound: A review of present knowledge', *Ultrasound in Medicine & Biology*, 2017.

[191] J. R. McLaughlan, D. M. Cowell and S. Freear, 'Gold nanoparticle nucleated cavitation for enhanced high intensity focused ultrasound therapy', *Physics in medicine and biology*, 2017.

[192] C. J. Diederich, 'Thermal ablation and high-temperature thermal therapy: Overview of technology and clinical implementation', *International journal of hyperthermia*, vol. 21, no. 8, pp. 745–753, 2005.

[193] L. Zhang and Z.-B. Wang, 'High-intensity focused ultrasound tumor ablation: Review of ten years of clinical experience', *Frontiers of medicine in China*, vol. 4, no. 3, pp. 294–302, 2010.

[194] J. E. Kennedy, 'High-intensity focused ultrasound in the treatment of solid tumours', *Nature reviews cancer*, vol. 5, no. 4, pp. 321–327, 2005.

[195] A. Blana, F. J. Murat, B. Walter, S. Thuroff, W. F. Wieland, C. Chaussy and A. Gelet, 'First analysis of the long-term results with transrectal HIFU in patients with localised prostate cancer', *European urology*, vol. 53, no. 6, pp. 1194–1203, 2008.

[196] N. Sanghvi, F. J. Fry, R. Bihrle, R. Foster, M. Phillips, J. Syrus, A. Zaitsev and C. Hennige, 'Noninvasive surgery of prostate tissue by high-intensity focused ultrasound', *IEEE Transactions on Ultrasonics, Ferroelectrics, and Frequency Control*, vol. 43, no. 6, pp. 1099–1110, 1996.

[197] M. Peek, M. Ahmed, A. Napoli, B. ten Haken, S. McWilliams, S. Usiskin, S. Pinder, M. Van Hemelrijck and M. Douek, 'Systematic review of high-intensity focused ultrasound ablation in the treatment of breast cancer', *British journal of surgery*, vol. 102, no. 8, pp. 873–882, 2015.

[198] D. Coluccia, J. Fandino, L. Schwyzer, R. O'Gorman, L. Remonda, J. Anon, E. Martin and B. Werner, 'First noninvasive thermal ablation of a brain tumor with MR-guided focusedultrasound', *Journal of therapeutic ultrasound*, vol. 2, no. 1, p. 17, 2014.

[199] K. Hynynen, G. T. Clement, N. McDannold, N. Vykhodtseva, R. King, P. J. White, S. Vitek and F. A. Jolesz, '500-element ultrasound phased array system for noninvasive focal surgery of the brain: A preliminary rabbit study with ex vivo human skulls', *Magnetic resonance in medicine*, vol. 52, no. 1, pp. 100–107, 2004.

[200] H. Grüll and S. Langereis, 'Hyperthermia-triggered drug delivery from temperature-sensitive liposomes using MRI-guided high intensity focused ultrasound', *Journal of Controlled Release*, vol. 161, no. 2, pp. 317–327, 2012.

[201] D. B. Rodrigues, P. R. Stauffer, D. Vrba and M. D. Hurwitz, 'Focused ultrasound for treatment of bone tumours', *International Journal of Hyperthermia*, vol. 31, no. 3, pp. 260–271, 2015.

[202] T. R. Wang, R. Dallapiazza and W. J. Elias, 'Neurological applications of transcranial high intensity focused ultrasound', *International Journal of Hyperthermia*, vol. 31, no. 3, pp. 285–291, 2015.

[203] J. Xiao, Z. Shi, J. Zhou, J. Ye, J. Zhu, X. Zhou, F. Wang and S. Zhang, 'Cesarean scar pregnancy: Comparing the efficacy and tolerability of treatment with high-intensity focused ultrasound and uterine artery embolization', *Ultrasound in medicine & biology*, vol. 43, no. 3, pp. 640–647, 2017.

[204] M. Brown, P. Farquhar-Smith, J. Williams, G. Ter Haar and N. deSouza, 'The use of high-intensity focused ultrasound as a novel treatment for painful conditions a description and narrative review of the literature', *BJA: British Journal of Anaesthesia*, vol. 115, no. 4, pp. 520–530, 2015.

[205] M. S. Canney, M. R. Bailey, L. A. Crum, V. A. Khokhlova and O. A. Sapozhnikov, 'Acoustic characterization of high intensity focused ultrasound fields: A combined measurement and modeling approach', *J Acoust Soc Am*, vol. 124, no. 4, pp. 2406–2420, Oct. 2008, 014810JAS[PII], ISSN: 0001-4966. DOI: 10.1121/1.2967836. [Online]. Available: http://www.ncbi.nlm.nih.gov/pmc/articles/PMC2677345/.

[206] C. A. Cain and S. Umemura, 'Concentric-ring and sector-vortex phased-array applicators for ultrasound hyperthermia', *IEEE Transactions on Microwave Theory and Techniques*, vol. 34, no. 5, pp. 542–551, May 1986, ISSN: 0018-9480. DOI: 10.1109/TMTT.1986.1133390.

[207] P. J. Benkeser, 'Unfocused multielement and tapered phased array ultrasound transducers for hyperthermia treatment', PhD thesis, University of Illinois, 1985.

[208] J. Sun and K. Hynynen, 'The potential of transskull ultrasound therapy and surgery using the maximum available skull surface area', *The Journal of the Acoustical Society of America*, vol. 105, no. 4, pp. 2519–2527, 1999.

[209] E. L. Carstensen, S. Z. Child, S. Norton and W. Nyborg, 'Ultrasonic heating of the skull', *The Journal of the Acoustical Society of America*, vol. 87, no. 3, pp. 1310–1317, 1990.

[210] F. Fry and J. Barger, 'Acoustical properties of the human skull', *The Journal of the Acoustical Society of America*, vol. 63, no. 5, pp. 1576–1590, 1978.

[211] G. Clement and K. Hynynen, 'Correlation of ultrasound phase with physical skull properties', *Ultrasound in medicine & biology*, vol. 28, no. 5, pp. 617–624, 2002.

[212] Y. Y. Botros, E. S. Ebbini and J. L. Volakis, 'Two-step hybrid virtual array ray (var) technique for focusing through the rib cage', *IEEE transactions on ultrasonics, ferroelectrics, and frequency control*, vol. 45, no. 4, pp. 989–1000, 1998.

[213] M. Tanter, M. Pernot, J.-F. Aubry, G. Montaldo, F. Marquet and M. Fink, 'Compensating for bone interfaces and respiratory motion in high-intensity focused ultrasound', *International Journal of Hyperthermia*, vol. 23, no. 2, pp. 141–151, 2007.

[214] A. H. Chan, V. Y. Fujimoto, D. E. Moore, R. W. Martin and S. Vaezy, 'An image-guided high intensity focused ultrasound device for uterine fibroids treatment', *Medical physics*, vol. 29, no. 11, pp. 2611–2620, 2002.

[215] L. Curiel, F. Chavrier, R. Souchon, A. Birer and J. Y. Chapelon, '1.5-D high intensity focused ultrasound array for non-invasive prostate cancer surgery', *IEEE transactions on ultrasonics, ferroelectrics, and frequency control*, vol. 49, no. 2, pp. 231–242, 2002.

[216] S. C. Tang and G. T. Clement, 'Acoustic standing wave suppression using randomized phase-shift-keying excitations', *The Journal of the Acoustical Society of America*, vol. 126, no. 4, pp. 1667–1670, 2009.

[217] J.-F. Aubry, 'Focusing ultrasound through bones: Past, current, and future transcostal and transskull strategies', *The Journal of the Acoustical Society of America*, vol. 141, no. 5, pp. 3549–3549, 2017.

[218] S. Concepts, *H- transducer series ø64 mm*, `http://bit.ly/2EOrwK6`, accessed 23/02/2018.

[219] P. Acoustics, *HIFU transducers*, `https://www.acoustics.co.uk/product/{HIFU}-transducers/`, accessed 23/02/2018.

[220] P. Davari, N. Ghasemi, F. Zare, P. O'shea and A. Ghosh, 'Improving the efficiency of high power piezoelectric transducers for industrial applications', *IET Science, Measurement & Technology*, vol. 6, no. 4, pp. 213–221, 2012.

[221] S. Tamano, H. Jimbo, T. Azuma, S. Yoshizawa, K. Fujiwara, K. Itani and S.-I. Umemura, 'Improvement of high-voltage staircase drive circuit waveform for high-intensity therapeutic ultrasound', *Japanese Journal of Applied Physics*, vol. 55, no. 7S1, 07KF17, 2016.

[222] P. Kaczkowski, 'Arbitrary waveform generation with the verasonics research ultrasound platform', Verasonics Inc., Tech. Rep., 2016.

[223] G. K. Lewis Jr and W. L. Olbricht, 'Design and characterization of a high-power ultrasound driver with ultralow-output impedance', *Review of scientific instruments*, vol. 80, no. 11, p. 114 704, 2009.

[224] W. Wong, C. Christoffersen, S. Pichardo and L. Curiel, 'An integrated ultrasound transducer driver for HIFU applications', in *Electrical and Computer Engineering (CCECE), 2013 26th Annual IEEE Canadian Conference on*, IEEE, 2013, pp. 1–5.

[225] K. Moro, S. Yoshizawa and S.-i. Umemura, 'Staircase-voltage metal–oxide–semiconductor field-effect transistor driver circuit for therapeutic ultrasound', *Japanese Journal of Applied Physics*, vol. 49, no. 7S, 07HF02, 2010.

[226] A. Berkovich, A. Bursian, K. Zaychenko and N. Petrishchev, 'A high-frequency generator used in high-intensity focused ultrasound transducers for tissue ablation and vessel obliteration', *Biomedical Engineering*, vol. 51, no. 3, pp. 215–217, 2017.

[227] D. M. Cowell, P. R. Smith and S. Freear, 'Phase-inversion-based selective harmonic elimination (PI-SHE) in multi-level switched-mode tone- and frequency-modulated excitation', *IEEE transactions on ultrasonics, ferroelectrics, and frequency control*, vol. 60, no. 6, pp. 1084–1097, 2013.

[228] S. Harput, M. Arif, J. McLaughlan, D. J. Cowell and S. Freear, 'The effect of amplitude modulation on subharmonic imaging with chirp excitation', *IEEE transactions on ultrasonics, ferroelectrics, and frequency control*, vol. 60, no. 12, pp. 2532–2544, 2013.

[229] B. E. Treeby, J. Jaros, A. P. Rendell and B. Cox, 'Modeling nonlinear ultrasound propagation in heterogeneous media with power law absorption using a k-space pseudospectral method', *The Journal of the Acoustical Society of America*, vol. 131, no. 6, pp. 4324–4336, 2012.

[230] D. Nassiri, D. Nicholas and C. Hill, 'Attenuation of ultrasound in skeletal muscle', *Ultrasonics*, vol. 17, no. 5, pp. 230–232, 1979.

[231] W. L. Nyborg, 'Heat generation by ultrasound in a relaxing medium', *The Journal of the Acoustical Society of America*, vol. 70, no. 2, pp. 310–312, 1981. DOI: 10.1121/1.386778. eprint: https://doi.org/10.1121/1.386778.

[232] H. H. Pennes, 'Analysis of tissue and arterial blood temperatures in the resting human forearm', *Journal of applied physiology*, vol. 1, no. 2, pp. 93–122, 1948.

[233] S. A. Sapareto and W. C. Dewey, 'Thermal dose determination in cancer therapy', *International Journal of Radiation Oncology* Biology* Physics*, vol. 10, no. 6, pp. 787–800, 1984.

[234] P. S. Yarmolenko, E. J. Moon, C. Landon, A. Manzoor, D. W. Hochman, B. L. Viglianti and M. W. Dewhirst, 'Thresholds for thermal damage to normal tissues: An update', *International Journal of Hyperthermia*, vol. 27, no. 4, pp. 320–343, 2011.

[235] J. McLaughlan, I. Rivens, T. Leighton and G. Ter Haar, 'A study of bubble activity generated in ex vivo tissue by high intensity focused ultrasound', *Ultrasound in medicine & biology*, vol. 36, no. 8, pp. 1327–1344, 2010.

[236] P. Lai, J. R. McLaughlan, A. B. Draudt, T. W. Murray, R. O. Cleveland and R. A. Roy, 'Real-time monitoring of high-intensity focused ultrasound lesion formation using acousto-optic sensing', *Ultrasound in medicine & biology*, vol. 37, no. 2, pp. 239–252, 2011.

[237] Y. Zhou, L. Zhai, R. Simmons and P. Zhong, 'Measurement of high intensity focused ultrasound fields by a fiber optic probe hydrophone', *The Journal of the Acoustical Society of America*, vol. 120, no. 2, pp. 676–685, 2006.

[238] G. ter Haar, A. Shaw, S. Pye, B. Ward, F. Bottomley, R. Nolan and A.-M. Coady, 'Guidance on reporting ultrasound exposure conditions for bio-effects studies', *Ultrasound in Medicine and Biology*, vol. 37, no. 2, pp. 177–183, 2011.

[239] W. W. Elliott AC, *Statistical analysis quick reference guidebook with SPSS examples*. Sage Publications, 2007.

[240] T. Leighton, *The acoustic bubble*. Academic press, 2012.

[241] K. Hynynen, *Impedance matching for ultrasound phased array elements*, US Patent 9,387,515, Jul. 2016.

[242] C. Hill, 'Calibration of ultrasonic beams for bio-medical applications', *Physics in Medicine & Biology*, vol. 15, no. 2, p. 241, 1970.

[243] J. R. McLaughlan, 'An investigation into the use of cavitation for the optimisation of high intensity focused ultrasound (HIFU) treatments', PhD thesis, Institute of Cancer Research (University Of London), 2008.

Appendix A

Additional AZA and EVA Systems Results

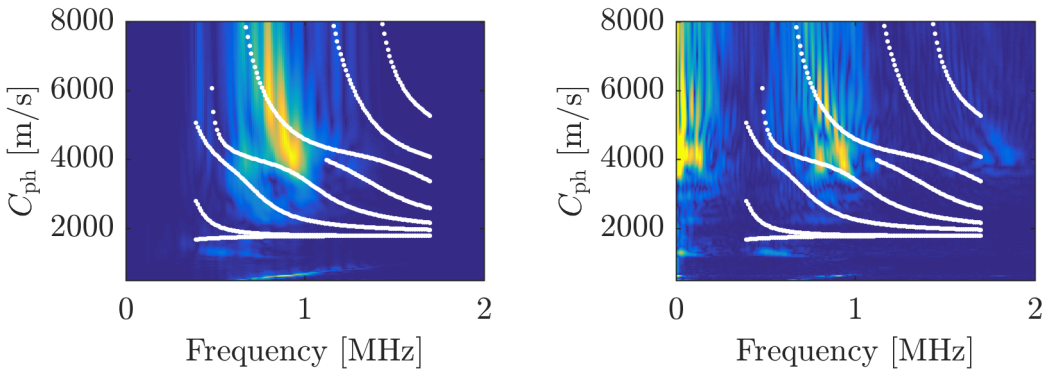

(a) FFT (b) PSAM

Figure A.1: Dispersion obtained using the EVA system from direction 1 using both FFT and PSAM techniques. Model data acquired from a micro CT scan is overlaid in white.

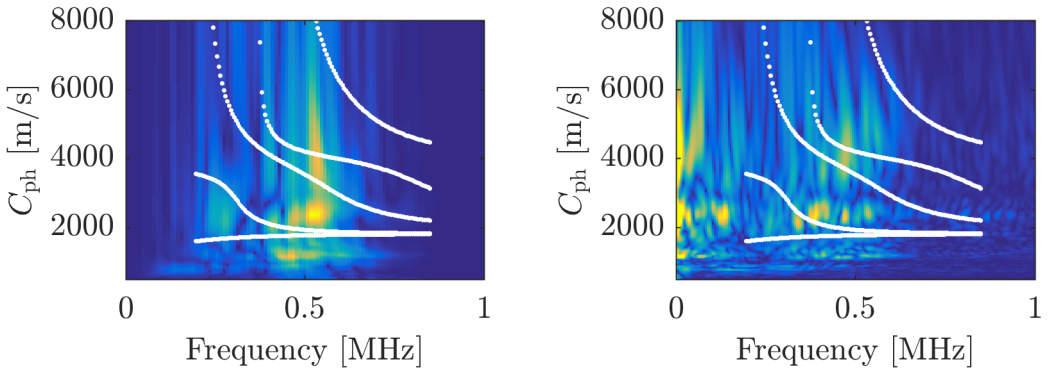

(a) FFT (b) PSAM

Figure A.2: Dispersion obtained using the AZA system from direction 1 using both FFT and PSAM techniques. Model data acquired from a micro CT scan is overlaid in white.

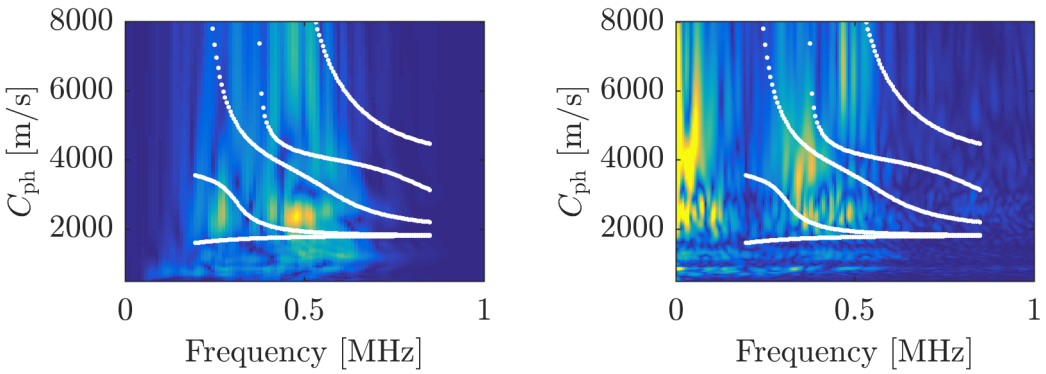

(a) FFT (b) PSAM

Figure A.3: Dispersion obtained using the AZA system from direction 2 using both FFT and PSAM techniques. Model data acquired from a micro CT scan is overlaid in white.

Appendix B

Dispersive Waves Phase Shift Program Code

```
function [W, F] = phaseFilter(M, Cph, L, fs)
    %W here is the output array you're after
    %F is the actual 2D filter

    %Work out szie of FFT
    N = nextpow2(size(M,1));
    N = 2^N;

    %Output W will be same sz as M
    W = zeros(size(M));

    %How many elements?
    zt = size(M,2); %aspatial
    sz = size(M,1);

    %Generate real frequency bins
    %This vector doesn't change because N increases
    %so resolution increases
    %automagically
    fRealPos = (0:N/2) * (fs/N);

    %This is a positive delay.
    %In other words mode delay is applied at channel1
    %THESE ARE POSITIVE WHEN CORRECT
```

```
    fd = (L/Cph) - 1./fRealPos;

    %Above vill produce some weird values at DC etc
    %Remove inf
    fd(isinf(fd)) = 0;

    %Generate an array for all filtering
    %Unity gain by default
    F = ones(N,zt);


    %For each channel..
    for i=1:zt
        %first channel is delayed the most because it comes first
        %Work out the discrete delay in samples
        fdz = fd*fs*(zt-i);

        %n vector used in DFT calculation
        NVEC = 0:N/2;
        f = exp((-1i*2*pi*NVEC.*-fdz)/N);

        %Maintain hermitian symmetry
        f_full = [f(1:end-1) fliplr(conj(f(2:end)))];

        %For the channel define the filter
        F(:,i) = f_full';
    end

    %Fft the incoming 2D array in one go
    Mf = fft(M, N, 1);

    %Apply the filter
    Mff = Mf .* F;
    Mt = ifft(Mff, N, 1,'symmetric');

    %Trim it accordingly (remove zero padding)
    W = (Mt(1:sz,:));

end
```